



Università degli Studi di Palermo and RWTH Aachen University

Coherence properties in superconducting flux qubits

PhD thesis of
Samuele Spilla

Dipartimento di Fisica e Chimica
and
Institut für Theorie der Statistischen Physik
December 2014

Supervisors
Dott.ssa Anna Napoli
Prof. Janine Splettstößer



UNIVERSITÀ DEGLI STUDI DI PALERMO

Dottorato in FISICA
Dipartimento di Fisica e Chimica
Settore Scientifico Disciplinare – FIS02

COHERENCE PROPERTIES IN SUPERCONDUCTING FLUX QUBITS

IL DOTTORE
SAMUELE SPILLA

IL COORDINATORE
PROF. ANTONIO CUPANE

IL TUTOR
DOTT.SSA ANNA NAPOLI

CO-TUTOR
PROF.SSA JANINE SPLETTSTÖBER

COHERENCE PROPERTIES OF SUPERCONDUCTING FLUX QUBITS

Der Fakultät für Mathematik, Informatik und Naturwissenschaften der RWTH Aachen University vorgelegte Dissertation in der genehmigten Form zur Erlangung des akademischen Grades eines Doktors der Naturwissenschaften von

M.Sc. Samuele Spilla

aus Palermo, Italien

Contents

Introduction	v
1 Properties of Josephson Junctions	1
1.1 Josephson junction	2
1.1.1 RCSJ model	3
1.1.2 Junction Hamiltonian	5
1.1.3 DC SQUID: a tunable junction	6
1.2 Microscopic model of the Josephson junctions	7
1.2.1 Thermal current in a single Josephson junction	8
1.2.2 Thermal current in linear response regime	10
2 Josephson qubits	13
2.1 Qubit as a quantum two-level system	13
2.2 Charge qubits	15
2.2.1 Cooper pair box	15
2.2.2 Quantronium and transmon	17
2.3 Flux and phase qubits	19
2.3.1 Phase qubit	19
2.3.2 RF-SQUID qubit	20
2.3.3 Persistent current qubit	23
2.3.4 Fluxonium qubit	24

2.4	Sources of decoherence	27
2.4.1	Relaxation sources	27
2.4.2	Dephasing sources	28
3	Exploiting quantum coherences in flux qubit systems	31
3.1	Double SQUID manipulated by fast modification of its energy potential	31
3.1.1	Experimental setup	32
3.1.2	Experimental results	35
3.1.3	The theoretical analysis	37
3.1.4	Theoretical results and conclusive remarks	39
3.2	GHZ state generation of three Josephson qubits in presence of bosonic baths	41
3.2.1	Ideal generation scheme	42
3.2.2	Dissipation due to coupling to ohmic bosonic baths	49
3.2.3	Conclusive remarks	53
4	Thermal current in superconducting flux qubits	55
4.1	Measurement and dephasing of a Delft qubit due to heat currents	56
4.1.1	Qubit-state sensitive heat currents	56
4.1.2	Impact of temperature gradients on the qubit dephasing	59
4.1.3	Conclusive remarks	63
4.2	Dephasing of the fluxonium qubit due to thermal currents	64
4.2.1	Thermal current in a fluxonium qubit	64
4.2.2	Independence of the sensitivity on the number of array junctions	65
4.2.3	Sensitivity near $f = 0.5$	66
4.2.4	Dephasing time	68
4.2.5	Conclusive remarks	73
5	Conclusions	75
A	Derivation of the Maki-Griffin formula for the heat current	77

B Dynamics of an open quantum system	81
C Appendix to the GHZ state generation scheme	83
C.1 Eigensolutions of the Hamiltonian given in (3.12)	83
C.2 Jump operators between the eigenstates of the Hamiltonian (3.12)	84
C.3 Jump operators of the Hamiltonian H_{rot}^{III}	85
D Slopes of the sensitivities	87
Acknowledgments	97
Curriculum Vitae	99
Publications	101

Introduction

The research work discussed in this thesis deals with the study of superconducting Josephson qubits. Superconducting qubits are solid-state artificial atoms which are based on lithographically defined Josephson tunnel junctions. When sufficiently cooled, these superconducting devices exhibit quantized states of charge, flux or junction phase depending on their design parameters. This allows to observe coherent evolutions of their states. Thanks to their relatively large size they are easy to manipulate and control experimentally [1–5]. Interestingly, their behavior can be theoretically analyzed by means of equivalent mechanical models [6] describing the motion of fictitious particles moving in an effective potential, thus offering the possibility to realize an effective two-level system [7]. For all these reasons superconducting integrated circuits represent leading candidates in many applicative emergent areas of physics [8–22] and furnish, at the same time, an important testbed for investigating fundamental issues of quantum mechanics, especially in regimes not easily accessible with natural atoms or molecules.

These considerations justify the intense research which has been developed in recent years in this context. Superconducting quantum circuits have been, for example, exploited to implement and to control quantum coherences as witnessed by the numerous papers discussing schemes for the realization of assigned multipartite entangled states [8, 11–13]. At the same time, many efforts have been made for protecting quantum coherences in the context of quantum computing and information applications [23–28]. The performance of solid state architecture is indeed unavoidably limited by decoherence and dissipation phenomena related to the presence of different noise sources partly stemming from control circuitry but also having microscopic origin. It is hence important to understand, and consequently to reduce, the causes of decoherence in different superconducting circuits. Generally speaking, there are many channels which a superconducting qubit may relax or dephase through, the relevance of each channel depending on the qubit used, its characterizing parameters and, more generally, on the experimental set up. In particular, flux qubits are extremely sensitive to flux noise and usually limited to operating in the two-level system subspace while charge qubits are more versatile but suffer from charge noise mostly due to stray quasiparticles. In general, in superconducting devices, quasiparticles are sources of energy relaxation and being an intrinsic property of superconducting materials, they could represent an ultimate limit of quantum coherences. The recent technological improvements of the past years have permitted the research on these devices to improve rapidly, starting with the demonstration of nanosecond-scale coherence in a Cooper pair box by Nakamura *et al* [29] in 1999 up to a coherence time above $20\mu\text{s}$ found by the MIT/NEC group in 2011 [30]

using a persistent-current flux qubit. Thus superconducting qubits of the last generation have reached regimes such that quasiparticle tunneling could become a source of decoherence not to be neglected [31–33].

The research work discussed in this thesis is inscribed in this context. The results presented can be divided into two parts. In a first part we investigate operations of superconducting qubits based on the quantum coherence in superconducting quantum interference devices (SQUID). We explain experimental data which has been observed in a SQUID subjected to fast, large-amplitude modifications of its effective potential shape. The motivations for this work come from the fact that in the past few years there have been attempts to interpret the supposed quantum behavior of physical systems, such as Josephson devices, within a classical framework [34, 35]. Moreover, we analyze the possibility of generating Greenberger-Horne-Zeilinger (GHZ) states, namely maximally entangled states, in a quantum system made out of three Josephson qubits. In particular, we investigate the possible limitations of the GHZ state generation due to coupling to bosonic baths.

In the second part of the thesis we address a particular cause of decoherence of flux qubits which has been disregarded until now: thermal gradients, which can arise due to accidental non equilibrium quasiparticle distributions. The reason for these detrimental effects is that heat currents flowing through Josephson tunnel junctions in response to a temperature gradient are periodic functions of the phase difference between the electrodes. This phenomenon was theoretically predicted in 1965 by Maki and Griffin [36]. The phase dependence of the heat current comes from Andreev reflection, namely an interplay between the quasiparticles which carry heat and the superconducting condensate which is sensitive to the superconducting phase difference. This effect has been demonstrated experimentally [37–41]. A superconducting ring, namely a *DC*-SQUID with two Josephson junctions was exposed to a temperature gradient. The measurement of the resulting heat current as a function of the magnetic flux penetrating the SQUID demonstrated the sensitivity of the heat current to the phase differences across the junctions. In this way, the SQUID is operated as a heat modulator. Generally speaking, the flux qubit states are characterized by different values of the phase difference through their Josephson junctions. Consequently, the phase-dependent thermal current through a device subject a temperature gradient is related to the phase-dependent qubit states. We study how the thermal currents change according to the state of the qubits hence yielding a measurement of the qubit state. This in turn leads to an impact of temperature gradient on the dynamics of the system. We show that flux qubits in the Delft qubit design can have limitations of the decoherence time to the order of microseconds as a result of this newly discovered source of decoherence. In contrast, the fluxonium qubit is found to be well protected due to its superinductance.

In this thesis the results I obtained during the three years of my Ph.D. studies, which I spent between the Dipartimento di Fisica e Chimica at the Università di Palermo and the Institut für Theorie der Statistischen Physik at the RWTH Aachen University, are presented and discussed.

This thesis is structured as follows: in Chapter 1 Josephson junctions are introduced and some of the physics of these system is explained. Chapter 2 is devoted to the presentation of different types of Josephson qubits. The study of the coherences and of their utilization is

the main subject of Chapter 3, in which firstly the coherence properties of a rf-SQUID (flux qubit) are studied when the system is manipulated by fast modification of its energy potential. Secondly, I explain how it is possible to build an entangled state using Josephson qubit, in presence of dissipation given by an interaction with bosonic baths. Chapter 4 is devoted to the study of decoherence effects due to temperature gradients in flux qubits, in particular the effects of thermal gradients on a persistent current qubit and on a fluxonium qubit will be studied.

Chapter 1

Properties of Josephson Junctions

The superconductivity in certain materials consists in the vanishing of the electrical resistance when their temperatures is lowered below a certain characteristic temperature of the material, called the critical temperature, T_c . This phenomenon is one of the most interesting and sophisticated in condensed matter physics even because the effect on electrical resistance is not the only remarkable property of superconducting materials, which have also interesting magnetic properties, for example the Meissner effect.

In 1957 John Bardeen, Leon Cooper and J. Robert Schrieffer developed a microscopic theory of superconductivity, which is known as the BCS theory. The central feature of the BCS theory is that two electrons in the superconductor are able to form a bound pair called a Cooper pair because they somehow experience an attractive interaction between them caused by the interaction of the electrons with the phonons in the material. In the superconducting state, the idea is that all electron pairs adopt the same phase like a unique wave. The quantum mechanical description of superconductivity, given by the BCS theory, models the whole network of electrons as a Bose-Einstein condensate characterized by one wave function, called also order parameter, $\psi = \sqrt{\rho}e^{i\theta}$, where ρ is the Cooper pair density and θ is the phase of the order parameter. To destroy the superconducting state described above and make it normal, a small amount of energy is needed. This energy is called the energy gap Δ .

From their discovery, superconducting materials have been used in many applicative areas. The first large scale commercial application of superconductivity was in magnetic resonance imaging (MRI) but they are also used in scientific research where high magnetic field electromagnets are required. In what follows we will not give a detailed description of BCS theory results on superconductivity, but instead we will focus on the properties of the Josephson junctions, which are made by superconducting materials and are the basic bricks which are used to build the superconducting qubits that are object of our studies.

1.1 Josephson junction

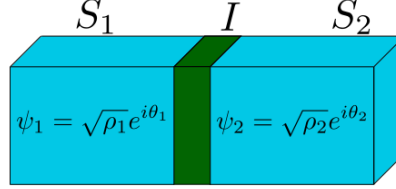


Figure 1.1: A Josephson junction: two superconducting electrodes $S_{1/2}$ (~ 100 nm) separated by a thin layer of insulating material I (~ 1 nm). The two condensates in the superconductors are described by their wave functions $\psi_{1/2}$.

A Josephson junction is made by two superconducting electrodes (~ 100 nm) separated by a thin layer of insulating material. If the layer between the two superconductors is sufficiently thin (~ 1 nm) the electrons can tunnel through the barrier. In the case of equivalent superconductors at both sides of the barrier, if ψ_i ($i = 1, 2$) is the wave function of the electrons in the i -th electrode, such that $|\psi_i|^2$ defines the Cooper pair density, and without magnetic field applied to the barrier, we write [42]

$$\begin{aligned} i\hbar \frac{\partial \psi_1}{\partial t} &= U_1 \psi_1 + K \psi_2, \\ i\hbar \frac{\partial \psi_2}{\partial t} &= U_2 \psi_2 + K \psi_1, \end{aligned} \quad (1.1)$$

where K is the coupling constant between the electrodes and U_i is the potential energy of each electrode. If there is a potential difference between the electrodes $U_1 - U_2 = 2eV$ ($2e$ being the charge of a Cooper pair), (1.1) becomes

$$\begin{aligned} i\hbar \frac{\partial \psi_1}{\partial t} &= eV \psi_1 + K \psi_2, \\ i\hbar \frac{\partial \psi_2}{\partial t} &= -eV \psi_2 + K \psi_1. \end{aligned} \quad (1.2)$$

Writing explicitly the wave functions, as a function of the phases θ_i and densities ρ_i of Cooper pairs for the i -th electrode

$$\begin{aligned} \psi_1 &= \sqrt{\rho_1} e^{i\theta_1}, \\ \psi_2 &= \sqrt{\rho_2} e^{i\theta_2}, \end{aligned} \quad (1.3)$$

we obtain

$$\begin{aligned} \dot{\rho}_1 &= 2\frac{K}{\hbar} \sqrt{\rho_1 \rho_2} \sin \varphi, \\ \dot{\rho}_2 &= -2\frac{K}{\hbar} \sqrt{\rho_1 \rho_2} \sin \varphi, \\ \dot{\theta}_1 &= \frac{K}{\hbar} \sqrt{\frac{\rho_2}{\rho_1}} \cos \varphi - \frac{eV}{\hbar}, \\ \dot{\theta}_2 &= \frac{K}{\hbar} \sqrt{\frac{\rho_1}{\rho_2}} \cos \varphi + \frac{eV}{\hbar}, \end{aligned} \quad (1.4)$$

where φ is the phase difference $\varphi = \theta_2 - \theta_1$ between the two electrodes. Since $\dot{\rho}_1 = -\dot{\rho}_2$, the current density of Cooper pairs flowing from the first to the second electrode is given by

$$J = 2\frac{K}{\hbar}\sqrt{\rho_1\rho_2}\sin\varphi = J_c\sin\varphi, \quad (1.5)$$

where $J_c = 2K\rho_0/\hbar$ and $\rho_0 = \sqrt{\rho_1\rho_2}$. Since we make the hypothesis of equivalent superconductors we have $\rho_1 = \rho_2 = \rho_0$.

From the equations for the phases θ_i we derive

$$\dot{\varphi} = \dot{\theta}_2 - \dot{\theta}_1 = 2eV/\hbar = \frac{2\pi}{\Phi_0}V, \quad (1.6)$$

where $\Phi_0 \equiv h/2e$ is the superconducting flux quantum. Starting from equation (1.6) one gets

$$\varphi(t) = \varphi(0) + \frac{2e}{\hbar}\int_0^t V(t)dt. \quad (1.7)$$

Equations (1.5) and (1.6) are known as Josephson relations. In particular (1.5) defines the *DC Josephson effect*, so that if it is possible to produce a constant difference of phase $\varphi \neq k\pi$ with $k \in \mathbf{Z}$, it is possible to observe a Cooper pair current, $I = I_c \sin \varphi$, flowing through the barrier without a potential drop through it, this current is also called *supercurrent*. The origin of the supercurrent can be traced back to Andreev reflection of incoming electrons and as such it is an interplay of quasiparticles at the interface and the superconducting condensate on both sides. The quasiparticles are the single electrons not arranged in Cooper pairs, which are present in the insulating barrier and in general also in the superconducting electrodes, when the temperature of the electrodes is different from zero [43]. The Andreev reflection is a type of particle scattering which occurs at interfaces between a superconductor and a normal state material and consists in the transfer of a charge $2e$ across the interface, avoiding the forbidden single-particle transmission within the superconducting energy gap. The Josephson effect was first predicted by Brian Josephson in 1962 [44] and subsequently experimentally confirmed the next year by Anderson and Rowell [45]. This chapter will be devoted to see how Josephson junctions can be treated as non linear circuitual elements and the associated Hamiltonian will be introduced. In this way we will understand how to use Josephson junctions to build superconducting Josephson junctions' based devices.

1.1.1 RCSJ model

The experimental behavior of a Josephson junction it is slightly different from the ideal case depicted in the previous section. This is given by the fact that in real case the junction has also a geometrical induced capacitance between its electrodes and a resistance giving dissipation when we have a finite voltage across it. To find a circuit analogue of a real Josephson junction, in this section it will be introduced the so-called RCSJ (*Resistively and Capacitively Shunted Junction*) model [46, 47], which describes it in terms of circuitual components. A real Josephson junction (*JJ*) can be conveniently modeled as a parallel of three circuitual elements, as shown in figure

1.2: a non-linear Josephson element which obeys equation (1.5) indicated by the symbol \times , in parallel with a capacitor C (which depends on the geometry and fabrication of the junction) and a resistance R . Assuming that the junction is current-biased, we can write the Kirchoff's

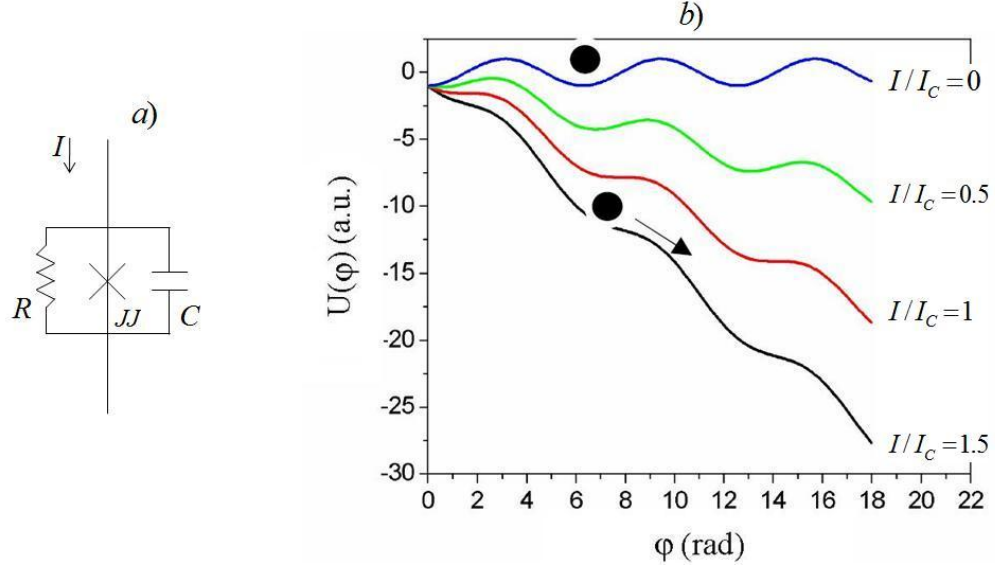


Figure 1.2: a) RCSJ model for a Josephson junction b) $U(\varphi)$ potential for different values of I/I_c .

current law as

$$I = C\dot{V} + I_c \sin \varphi + \frac{V}{R}, \quad (1.8)$$

which exploiting equation (1.6) can be written in the form

$$I = C \frac{\Phi_0}{2\pi} \ddot{\varphi} + \frac{1}{R} \frac{\Phi_0}{2\pi} \dot{\varphi} + I_c \sin \varphi. \quad (1.9)$$

The behavior of the system can be more easily analyzed by means of an equivalent mechanical model [6, 48–51], describing the motion of a fictitious particle of “mass” $m = C(\Phi_0/2\pi)^2$. Using equation (1.9) as an equation of motion for this particle it is possible to put it in the form

$$m\ddot{\varphi} + \gamma\dot{\varphi} + \frac{\partial U(\varphi)}{\partial \varphi} = 0 \quad (1.10)$$

where $\gamma = \frac{\Phi_0}{2\pi} \frac{1}{R}$ is a viscous damping coefficient, and the effective *washboard* potential is of the form

$$U(\varphi) = -E_J \left(\frac{I}{I_c} \varphi + \cos \varphi \right), \quad (1.11)$$

where $E_J \equiv (\Phi_0 I_c / 2\pi)$ is called Josephson coupling energy. The current I biasing the junction tilts the potential (figure 1.2.b)), which presents maxima and minima. The height of the barrier

between a minimum and the next maximum is

$$\Delta U = 2E_J \left[\sqrt{1 - (I/I_c)^2} - \frac{I}{I_c} \arccos(I/I_c) \right]. \quad (1.12)$$

It is possible to distinguish qualitatively three different regimes for the junction. If $I < I_c$ the particle remains trapped in a potential hole, oscillating with *plasma frequency* $\Omega_P = \left(\frac{2\pi I_c}{\Phi_0 C} \right)^{\frac{1}{2}}$ around the minimum. Since the phase averages to zero there is no voltage drop through the junction, the junction is in the superconducting regime. When I becomes bigger, the particle remains in the hole until $I = I_c$, when the minima become flex points. If $I > I_c$, the particle starts to move with velocity $\dot{\varphi} \neq 0$ along the potential, which from equation (1.6) yields a voltage drop across the junction, the junction is in the normal regime. When $I \gg I_c$ the particle tends to move with constant velocity $\dot{\varphi} = \frac{2\pi}{\Phi_0} IR$ and has an ohmic behavior $V = IR$.

1.1.2 Junction Hamiltonian

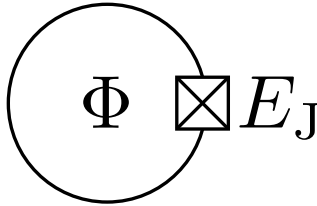


Figure 1.3: Real Josephson junction in a loop threaded by the magnetic flux Φ . A real Josephson junction is indicated with a \times enclosed in a square.

Let us now close the Josephson junction circuit in a loop and imagine that the loop is threaded by a magnetic flux Φ as shown in fig 1.3. The superconducting order parameter must be single valued, and this imposes a quantization condition (fluxoid quantization): the total phase difference around the loop must be quantized in units of the flux quantum Φ_0 . This condition may be expressed as

$$2\pi n = \varphi - 2\pi \frac{\Phi}{\Phi_0} \quad (1.13)$$

where n is the number of flux quanta Φ_0 .

If the temperature of the system is sufficiently low it is possible to neglect the dissipative term in equation (1.8) and write the equation for an isolated junction as $C\dot{V} + I_c \sin \varphi = 0$ or as

$$\frac{2\pi\ddot{\Phi}}{\Phi_0} + \Omega_P \sin \left(\frac{2\pi\Phi}{\Phi_0} \right) = 0. \quad (1.14)$$

In the previous equation Ω_P is the plasma frequency that characterizes the phase evolution time. In order to obtain equation (1.14) as equation of motion of the virtual particle of “mass” C and

generalized coordinate Φ one can start from the Lagrangian function

$$L(\Phi, \dot{\Phi}) = \frac{1}{2}C\dot{\Phi}^2 + E_J \cos\left(\frac{2\pi\Phi}{\Phi_0}\right). \quad (1.15)$$

The conjugate momentum to the coordinate Φ is given by

$$p_\Phi \equiv \frac{\partial L}{\partial \dot{\Phi}} = C\dot{\Phi} = q, \quad (1.16)$$

namely the charge $q = CV$ and the Hamiltonian of the system can be written

$$H(\Phi, p_\Phi) \equiv p_\Phi \dot{\Phi} - L = \frac{q^2}{2C} - E_J \cos\left(\frac{2\pi\Phi}{\Phi_0}\right). \quad (1.17)$$

This Hamiltonian is easily quantized substituting the classical variables Φ and q with the corresponding quantum operators $\hat{\Phi}$ and $\hat{q} = -i\partial/\partial\hat{\Phi}$, which satisfy the commutation relation $[\hat{\Phi}, \hat{q}] = i\hbar$, such that

$$\hat{H} = \frac{\hat{q}^2}{2C} - E_J \cos\left(\frac{2\pi\hat{\Phi}}{\Phi_0}\right). \quad (1.18)$$

Defining the number operator $\hat{n} = \frac{\hat{q}}{2e}$ and the phase operator $\hat{\varphi} = \frac{2\pi}{\Phi_0}\hat{\Phi}$, so that $[\hat{\varphi}, \hat{n}] = i\hbar$, the Hamiltonian can be put in the form [52]

$$\hat{H} = 4E_C\hat{n}^2 - E_J \cos \hat{\varphi} \quad (1.19)$$

equation (1.19) shows that the term corresponding to the kinetic energy is proportional to the *Coulomb energy* $E_C = \frac{e^2}{2C}$, which corresponds to the electrostatic energy of an electron on the capacitor C (this means that a superconducting Cooper pair has charging energy $4E_C$), while the Josephson energy E_J is proportional to the potential term. The dynamical behavior of a junction depends on the competition between these two different energies. If $E_C \gg E_J$ (charge regime) the number of Cooper pairs $n = q/2e$ on the capacitor can be considered constant since the energy required to change this number is big. Consequently, here is a great indetermination on the phase ($\Delta\varphi \rightarrow \infty$). In this regime the description of the system can be done using charge eigenstates (or eigenstates of the number operator), and q (or n) is a “good” quantum number. If $E_J \gg E_C$ (phase regime) the junction works as an anharmonic semi-classical oscillator and Φ (or φ) is a “good” quantum number. When E_C and E_J are of the same order of magnitude (mesoscopic regime) neither the charge (or number) nor the flux (or the phase) are good quantum numbers, and a great indetermination for both the coordinate and its conjugate has to be taken into account. In what follows it will be shown that different types of superconducting qubits built with Josephson junctions correspond to different operating regimes of the junction.

1.1.3 DC SQUID: a tunable junction

In this section, it will be shown how a device which has the same effective behavior as that of a Josephson junction can be built, using more than one Josephson junction. The importance of

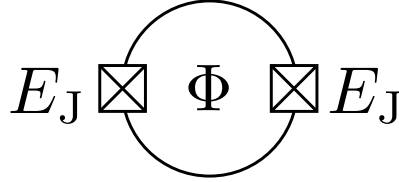


Figure 1.4: DC SQUID: a superconducting loop interrupted by two junctions and threaded by a magnetic flux Φ .

this device is that the critical current of the effective junction is tunable. The Direct-Current Superconducting Quantum Interference Device (DC SQUID) is a superconducting loop interrupted by two junctions (figure 1.4). A current I flows into the SQUID and then separates into two currents I_j in the arms $j = 1, 2$. In each arm of the SQUID there is a Josephson junction with critical current I_{c_j} , phase φ_j , and Josephson inductance L_j in each arm. There is also in general a geometric inductance in each arm which will be considered small with respect to the Josephson inductances. The total inductance around the loop is L . The current passing through branch j is given by the Josephson current equation (1.5), such that the total current is

$$I = I_{c1} \sin \varphi_1 + I_{c2} \sin \varphi_2. \quad (1.20)$$

An external magnetic field is applied to the SQUID, and it yields a flux Φ penetrating the loop. The fluxoid quantization may be expressed as

$$2\pi n = \varphi_2 - \varphi_1 - 2\pi f \quad (1.21)$$

where n is the number of flux quanta Φ_0 and $f = \Phi/\Phi_0$. If one assumes that the critical currents are equal $I_{c1} = I_{c2} \equiv I_c$, then equations (1.20) and (1.21) can be combined and yield

$$I = 2I_c \cos \left(\pi \frac{\Phi}{\Phi_0} \right) \sin \left(\frac{\varphi_1 + \varphi_2}{2} \right) \quad (1.22)$$

which is analogue to the first Josephson equation taking as critical current

$$I_{c,\text{SQ}}(\Phi) = 2I_c \left| \cos \left(\pi \frac{\Phi}{\Phi_0} \right) \right| \quad (1.23)$$

and $(\varphi_1 + \varphi_2)/2$, the symmetric phase of the SQUID, as phase of the equivalent junction. The critical current of the SQUID $I_{c,\text{SQ}}$ is hence a function of the external flux and it can be tuned between 0 and $2I_c$. In this way, the DC SQUID acts as a tunable Josephson junction. This feature is also used to make tunable superconducting qubits. In particular, if the two junctions in the loop are equivalent, the DC SQUID acts as a junction with internal capacitance which is twice the one of each junction and with resistance which is half of the one of each junction.

1.2 Microscopic model of the Josephson junctions

For the scope of this thesis it is useful to briefly introduce a *microscopic* model of the Josephson junction. Exploiting the Bardeen-Cooper-Schrieffer (BCS) theory of superconductivity, each

superconductor (the two electrodes are denoted by $l = 1, 2$) is assumed to be a particle reservoir in equilibrium at temperature T_l and to be characterised by the mean-field BCS Hamiltonian

$$H_l = \sum_{k,\sigma} (\varepsilon_{l,k} - \mu_0) c_{l,k\sigma}^\dagger c_{l,k\sigma} - \sum_k (\Delta_{l,k} c_{l,k\uparrow}^\dagger c_{l,-k\downarrow}^\dagger + \Delta_{l,k}^* c_{l,-k\downarrow} c_{l,k\uparrow}). \quad (1.24)$$

In (1.24), $c_{l,k\sigma}^\dagger$ and $c_{l,k\sigma}$ are single-electron creation and annihilation operators in the momentum k and spin $\sigma = \uparrow, \downarrow$ representation and $\Delta_{l,k}$ is the superconducting energy gap of the l -th electrode. Tunnelling between reservoirs is described by the tunnelling Hamiltonian

$$H_T = \sum_{k,q,\sigma} (V_{kq}^{12} c_{1,k\sigma}^\dagger c_{2,q\sigma} + V_{kq}^{12*} c_{2,q\sigma}^\dagger c_{1,k\sigma}), \quad (1.25)$$

where k and q are the momentum quantum numbers and the tunnelling matrix element is denoted by V_{kq}^{12} . The total Hamiltonian is then written as $H_{\text{tot}} = H_1 + H_2 + H_T$.

In equation (1.24), $\varepsilon_{l,k\sigma} - \mu_0 \equiv \xi_{l,k\sigma}$ is the electron energy relative to the chemical potential which is assumed equal for the two electrodes, $\mu_1 = \mu_2 = \mu_0$. Assuming the gap to be independent of k , it is characterized by its absolute value $|\Delta_l|$ and by the phase θ_l . As introduced before the phase differences φ across a junction is given by $\varphi = \theta_2 - \theta_1$. The temperature dependence of the magnitude of the superconducting gap is approximately given by $|\Delta_l(T_l)| \approx \Delta_0 \sqrt{1 - T_l/T_{\text{crit}}}$ with $\Delta_0 \simeq k_B T_{\text{crit}}$ the gap of the superconductor at zero temperature and T_{crit} the critical temperature. It will be assumed from now on that all the superconductors are built from the same material with equivalent geometries, such that they share T_{crit} and Δ_0 .

1.2.1 Thermal current in a single Josephson junction

Using the microscopic model description of the Josephson junction, it is interesting to derive the heat currents flowing through a Josephson junction, when the arms between the junction are kept at different temperatures. Assuming that the system is sufficiently isolated and that in particular phonons are frozen out at very low temperatures, the heat current in electrode 1 is carried by electrons entering or leaving it, accompanied by a change in the expectation value of the Hamiltonian in the first electrode as in equation (1.24), namely H_1 , with respect to the electrochemical potential. According to the quantum-mechanical equation of motion, the heat current into the first electrode is

$$\frac{dQ^{(1)}}{dt} = \left\langle \frac{d}{dt} H_1 \right\rangle = \frac{i}{\hbar} \langle [H_{\text{tot}}, H_1] \rangle. \quad (1.26)$$

where the brackets $\langle \cdot \rangle$ denote the equilibrium average with respect to the total Hamiltonian H_{tot} , introduced before as the sum of the Hamiltonians of the electrodes H_l and of the tunneling Hamiltonian H_T . Evaluating the commutator in equation (1.26) we derive

$$\frac{dQ^{(1)}}{dt} = \frac{2}{\hbar} \text{Im} \left\{ \sum_{k,q,\sigma} \left\langle V_{kq}^{12} \xi_{1,k} c_{1,k\sigma}^\dagger c_{2,q\sigma} + V_{kq}^{12} (\Delta_{1,-k}^* c_{1,-k\uparrow} c_{2,q\downarrow} - \Delta_{1,k}^* c_{1,-k\downarrow} c_{2,q\uparrow}) \right\rangle \right\}. \quad (1.27)$$

Manipulating equation (1.27) we derive the heat current in the weak tunnel coupling regime [36, 53], see the appendix for a detailed derivation of the heat current. The result for the heat current through a junction connecting reservoir 1 and 2 due to a difference in temperature, $T_1 \neq T_2$, can be divided into a pure quasiparticle contribution to the heat current, $\dot{Q}_{\text{qp}}^1(T_1, T_2)$, and an interference contribution due to an interplay between quasiparticles and the Cooper pair condensate, $\dot{Q}_{\text{int}}^1(T_1, T_2)$, namely

$$\dot{Q}^1(T_1, T_2) = \dot{Q}_{\text{qp}}^1(T_1, T_2) - \dot{Q}_{\text{int}}^1(T_1, T_2) \cos \varphi . \quad (1.28)$$

The pure quasiparticle contribution to the heat current is

$$\dot{Q}_{\text{qp}}^1(T_1, T_2) = \frac{2}{e^2 R_{12}} \int_{|\Delta_{\text{max}}|}^{\infty} d\omega \omega^3 \frac{f_1(\omega) - f_2(\omega)}{\sqrt{\omega^2 - |\Delta_1|^2} \sqrt{\omega^2 - |\Delta_2|^2}} , \quad (1.29)$$

where $f_l(\omega) = [1 + \exp(\omega/k_B T_l)]^{-1}$ is the Fermi function of electrode l with $l = 1, 2$ and $|\Delta_{\text{max}}| = \max\{|\Delta_1|, |\Delta_2|\}$. R_{12} is the normal state resistance of the junction connecting reservoirs 1 and 2 and is related to the normal conducting density of states of the reservoirs at the Fermi level (including spin), N_l^0 , and the tunneling amplitude supposed to be independent of the momenta k and q). The inverse resistance is given by $R_{12}^{-1} = \pi e^2 N_1^0 N_2^0 |V^{12}|^2 / \hbar$. The interference contribution to the heat current due to the interplay between quasiparticles and the Cooper pair condensate depends on the phase difference φ of the superconducting condensates and yields

$$\dot{Q}_{\text{int}}^1(T_1, T_2) = \frac{2}{e^2 R_{12}} \int_{|\Delta_{\text{max}}|}^{\infty} d\omega \omega |\Delta_1 \Delta_2| \frac{f_1(\omega) - f_2(\omega)}{\sqrt{\omega^2 - |\Delta_1|^2} \sqrt{\omega^2 - |\Delta_2|^2}} . \quad (1.30)$$

It is $T_1, T_2 \lesssim |\Delta_0|/k_B$ and the square root terms are changing faster than the other factors in the integrals of Eqs. (1.29) and (1.30). The magnitude of the heat currents can then be estimated as

$$\begin{aligned} \dot{Q}_{\text{qp}}^l(T_l, T_m) &\simeq \dot{Q}_{\text{int}}^l(T_l, T_m) \simeq \dot{Q}_{\text{typ}} \\ &= \frac{|\Delta_{\text{max}}|^2}{e^2 R_{lm}} K(|\Delta_{\text{min}}|/|\Delta_{\text{max}}|) [e^{-|\Delta_{\text{max}}|/k_B T_l} - e^{-|\Delta_{\text{max}}|/k_B T_m}] , \end{aligned} \quad (1.31)$$

where $K(k) = \int_0^{\pi/2} (1 - k^2 \sin^2 \phi)^{-1/2} d\phi$ is the complete elliptic integral of the first kind, and $|\Delta_{\text{min}}|$ the superconducting gap at the largest temperature. The elliptic integral is a monotonously increasing function which starts at $\pi/2$ for small arguments and has a logarithmic divergence with $K(1 - \epsilon^2) \sim \ln 1/\epsilon$ when k approaches 1. Since the contribution of the integrands of (1.29) and (1.30) have a maximum for ω being in the vicinity of the superconducting gap $|\Delta_{\text{max}}|$, the quasiparticle and the interference contributions to the heat current are generally of the same order of magnitude.

It is interesting now to briefly give an estimate of the order of magnitude of the heat currents for the limits of small and large temperature differences. In the case of a *small temperature difference*, $\delta T \equiv |T_l - T_m| \ll T_l, T_m$, we obtain from (1.31) the typical value $\dot{Q}_{\text{typ}} \simeq |\Delta_{\text{max}}|^3 K[1 - \delta T/2(T_{\text{crit}} - T)] e^{-|\Delta_{\text{max}}|/k_B T} \delta T / (e^2 R_{lm} k_B T^2)$ of the heat current. Assuming furthermore that $\delta T \ll T_{\text{crit}} - T$, we obtain the estimate $\dot{Q}_{\text{typ}} \simeq |\Delta_{\text{max}}|^3 \ln[(T_{\text{crit}} -$

$T)/T_{\text{cut}}]e^{-|\Delta_{\text{max}}|/k_{\text{B}}T}\delta T/(e^2R_{lm}k_{\text{B}}T^2)$. The tunneling approximation gives a cutoff temperature $T_{\text{cut}} = \delta T$ which leads to a logarithmic divergence of the heat current for small temperature gradients as already pointed out in [36]. However, as shown in [53] this is an artifact of the tunneling approximation which fails to take properly into account a resonance in the density of states due to a weakly bound Andreev state. The resonance introduces a new cutoff at the scale $T_{\text{cut}} = D\Delta_0 \sin^2(\varphi_{lm}/2)/k_{\text{B}}$ with D the transparency of the tunneling barrier, which essentially describe a tunneling barrier denoting its characteristic transmission probability of the modes. The form of the thermal current in the case of small temperature difference will be given in the next paragraph.

In contrast, in the case of a *large temperature difference*, we have that $T_{\text{min}} \ll T_{\text{max}}$. Since in this case T_{min} is hence also always much smaller than T_{crit} , the heat current only depends on T_{max} and we obtain the estimate $\dot{Q}_{\text{typ}} \simeq \Delta_0^2 e^{-\Delta_0/k_{\text{B}}T_{\text{max}}} K(\sqrt{1 - T_{\text{max}}/T_{\text{crit}}})/e^2R_{lm}$. If we additionally have that $T_{\text{max}} \lesssim T_{\text{crit}}$, the elliptic integral is of order one and the estimate simply reads $\dot{Q}_{\text{typ}} \simeq \Delta_0^2 e^{-\Delta_0/k_{\text{B}}T_{\text{max}}}/e^2R_{lm}$.

Thermal currents in a system similar to the one we study here were measured in the experiment by Giazotto and Martinez-Perez reported in [38]. If we use these same experimental values for an estimate, we have $\Delta_0 \simeq 200 \mu\text{eV}$ and $R_{12} \simeq 1 \text{ k}\Omega$. For $T = 0.1T_{\text{crit}}$ and large temperature gradient we obtain $\dot{Q}_{\text{typ}} \simeq 10^{-11} \text{ W}$, while for a small temperature gradient we obtain the estimate $\dot{Q}_{\text{typ}} \simeq (\delta T/T)10^{-14} \text{ W}$ (assuming that the logarithm is of order one).

1.2.2 Thermal current in linear response regime

In the case when $T_1 = T$ and $T_2 = T + \delta T$ with $\delta T \ll T$ we approximate the thermal current in a power series of δT . In order to do this, since the two superconductors' energy gap are assumed to be dependent only on the temperature, they will considered to be equal $\Delta_1 = \Delta_2 = \Delta$. In Ref. [53], the thermal current between the two superconducting electrodes has been calculated. The result in linear response is given by

$$\dot{Q}(\varphi, T, \delta T) = -\kappa(\varphi, T)\delta T \quad (1.32)$$

with

$$\kappa = \frac{1}{2e^2R_{12}k_{\text{B}}T^2} \int_{\Delta}^{\infty} d\omega \frac{\omega^2}{\cosh^2(\omega/2k_{\text{B}}T)} \frac{\omega^2 - \Delta^2}{(\omega^2 - \omega_{\text{b}}^2)^2} \left[(\omega^2 - \Delta^2 \cos \varphi) - D\Delta^2 \sin \frac{\varphi^2}{2} \right] \quad (1.33)$$

where D is the transparency of the interface barrier. Moreover, $\omega_{\text{b}} = \Delta[1 - D \sin^2(\varphi/2)]^{1/2}$ is the energy associated with a quasi-bound Andreev state in the interface. There is a dependence of the thermal current on the phase difference φ across the junction. In the tunneling regime, that is for $D \ll 1$, the term proportional to D appearing in the right side of equation (1.33) can be neglected obtaining

$$\kappa = \frac{1}{2e^2R_{12}k_{\text{B}}T^2} \int_{\Delta}^{\infty} d\omega \frac{\omega^2}{\cosh^2(\omega/2k_{\text{B}}T)} \frac{\omega^2 - \Delta^2}{(\omega^2 - \omega_{\text{b}}^2)^2} (\omega^2 - \Delta^2 \cos \varphi). \quad (1.34)$$

The dependence on the phase can be made more explicit when bringing the expression (1.34) into the form

$$\kappa = \kappa_0 - \kappa_1 \sin^2 \frac{\varphi}{2} \ln \left(\sin^2 \frac{\varphi}{2} \right) + \kappa_2 \sin^2 \frac{\varphi}{2} \quad (1.35)$$

with the coefficients

$$\begin{aligned} \kappa_0 &= \frac{1}{2e^2 R_{12} k_B T^2} \int_{\Delta}^{\infty} d\omega \frac{\omega^2}{\cosh^2(\omega/2k_B T)} \\ \kappa_1 &= \frac{\Delta^3}{8e^2 R_{12} k_B T^2 \cosh^2(\Delta/2k_B T)}, \\ \kappa_2 &= \frac{\Delta^3}{8e^2 R_{12} k_B T^2} \left[\frac{4k_B T}{\Delta} (1 - \tanh(\Delta/2k_B T)) + c \right] \\ &\quad - (1 + \ln D) \kappa_1, \\ c &= 2 \int_0^{\infty} dx x \ln x \left[\frac{(\Delta/k_B T) \sinh \left(\frac{\sqrt{x^2+1}}{2k_B T/\Delta} \right)}{(x^2+1) \cosh^3 \left(\frac{\sqrt{x^2+1}}{2k_B T/\Delta} \right)} \right. \\ &\quad \left. + \frac{1}{(x^2+1)^{3/2} \cosh^2 \left(\frac{\sqrt{x^2+1}}{2k_B T/\Delta} \right)} \right]. \end{aligned} \quad (1.36)$$

In the next parts of the thesis, the results derived in this chapter will be the starting point to introduce the physical systems, namely the superconducting Josephson qubits, and to study them exploiting the physical properties of superconducting materials in general and in particular of the Josephson junctions.

Chapter 2

Josephson qubits

Josephson qubits are all those qubits realized by electronic circuits made with superconducting Josephson junctions and other superconducting components. They manifest their quantum behavior when appropriately cooled. Superconducting qubits have attracted considerable attention since the 1980s until today as they are considered the ideal “two-level systems” to be exploited for the realization of a quantum computer. All superconducting qubits can be seen as simple LC -oscillators which have been made anharmonic thanks to the addition of Josephson elements. The big variety of Josephson qubits introduced in literature in the last years is due to the variety of exploited circuit architectures as well as to the number and size of the Josephson junctions used. It is possible to make a first chronological division of these devices distinguishing between the “first-generation” qubits, including *Cooper pair box* [29, 54–57], *Quantronium* [58], *RF SQUID* [59], *phase qubit* [1] and *persistent-current flux qubit* (also called *Delft qubit*) [60, 61] and the “next-generation” qubits, basically *Transmon* [62] and *Fluxonium* [63]. Alternatively we can distinguish them based on the comparison between the two energies E_C and E_J , namely the charging energy and the Josephson energy, introduced in the previous chapter, characterizing the system. Depending on the value of the ratio E_C/E_J the states of the system will be described by charge or flux states. This in turn allows to separate the superconducting qubits in two big classes: charge and flux qubits. The aim of the chapter is to provide an overview of the superconducting qubits, introducing their Hamiltonian, the fundamentals of their operation, their similarities and their differences. In particular in view of the results presented in chapter 4, this chapter will concentrate on two different Josephson flux qubits, namely the Delft qubit and the Fluxonium.

2.1 Qubit as a quantum two-level system

Qubits are systems whose states have energies close together and very different from those of all other states of the system. To a first approximation, if we want to analyze the dynamics of the two states or the effect on them of a perturbation, we can simply ignore all the other

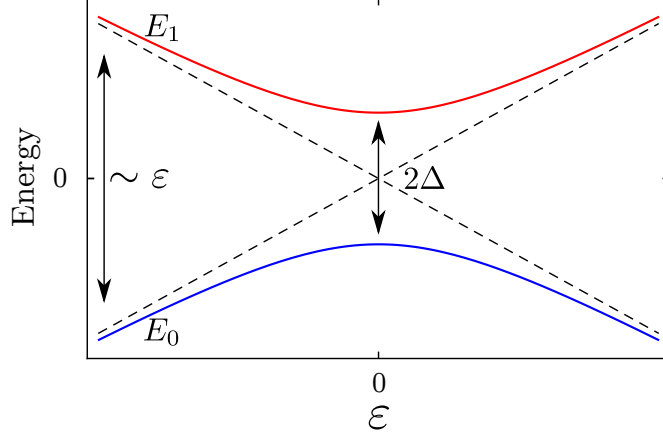


Figure 2.1: Variation of the energies E_1 and E_0 with respect to ϵ . If Δ is zero, the levels cross at the origin (dashed straight lines). When Δ is different from zero we obtain an avoided level crossing.

energy levels of the system. All the calculations can then be performed in a two-dimensional subspace of the state space. In other words qubits can be treated as quantum two-level systems. In this small section we will see some mathematical tools to study the dynamics of a qubit and to understand some of its physical properties.

Let us choose $|0\rangle$ and $|1\rangle$ as a basis states for the qubit. Usually the qubit Hamiltonian will be written as

$$\hat{H}_0 = -\frac{\hbar}{2} [\epsilon \hat{\tau}_3 + \Delta \hat{\tau}_1] \quad (2.1)$$

where $i = 1, 3$ are the Pauli spin matrices. The Bohr frequency of the system will take the form [64]

$$\omega_{01} = \frac{E_1 - E_0}{\hbar} = \sqrt{\epsilon^2 + 4|\Delta|^2}. \quad (2.2)$$

When ϵ varies, E_0 and E_1 describe two branches of a hyperbola which is symmetrical with respect to the coordinate axes and whose asymptotes are the values $\pm\epsilon/2$, as it is shown in figure 2.1. This means that if Δ is zero, the levels are the dashed straight lines and they cross at the origin. When Δ is different from zero the two levels “repel each other” and we obtain what usually is called an avoided level crossing.

The state of the qubit will be described by the density operator $\rho(t)$

$$\rho(t) = \begin{pmatrix} \rho_{00}(t) & \rho_{01}(t) \\ \rho_{10}(t) & \rho_{11}(t) \end{pmatrix} \quad (2.3)$$

and the dynamics of the system will be controlled by the Liouville-von Neumann equation ($\hbar = 1$)

$$\dot{\rho}(t) = -i[H, \rho(t)] \quad (2.4)$$

where H is the Hamiltonian of the complete system which, in general, can take into account the interaction of the system with its environment. If the qubit is coupled with an external environment (which could also simply be the measurement device) we can have two kinds of detrimental effects on its state: relaxation and decoherence. The relaxation affects the diagonal elements of the density operator, which will ultimately reach the thermal equilibrium value

$$\rho_{00,11}^{\text{eq}} = \frac{\exp\left(\pm \frac{\hbar\omega_{10}}{2k_{\text{B}}T}\right)}{\text{tr}\left\{\exp\left(\frac{\hat{H}_0}{2k_{\text{B}}T}\right)\right\}}. \quad (2.5)$$

The relaxation time, namely the time which takes for the diagonal terms of the qubit to relax, will be called \mathcal{T}_1 . The decoherence affects the non-diagonal terms which are essential to the quantum operations of the qubit. The coherence time, denoted with \mathcal{T}_2 is the length of time for which the qubit maintains a given superposition of states. There are two processes that contribute to decoherence: relaxation and dephasing [52]. The dephasing is the the way in which coherence decays over time. The amount of time that it takes for dephasing to recover classical behavior from a quantum system is called dephasing time and is denoted with \mathcal{T}_ϕ . The relaxation time \mathcal{T}_1 and the dephasing time \mathcal{T}_ϕ combine to yield

$$\frac{1}{\mathcal{T}_2} = \frac{1}{2\mathcal{T}_1} + \frac{1}{\mathcal{T}_\phi}. \quad (2.6)$$

2.2 Charge qubits

A charge qubit is a qubit whose basis states are charge states (i.e. states which represent the presence or absence of excess Cooper pairs in a superconducting electrode, called the “island”). The circuit that paradigmatically represents the charge qubit is the Cooper Pair Box (CPB) which is formed by a tiny superconducting island coupled by a Josephson junction to a superconducting reservoir. The state of the qubit is determined by the number of Cooper pairs which occupy the box. The other two charge qubit which will be presented in this paragraph are the Quantronium and the Transmon. These two circuits are modifications of the CPB, which improve dramatically the dephasing times of the original circuit. We will see that this is possible because Quantronium and Transmon manage mostly to better deal with the charge noise, which is the biggest problem with this kind of circuits.

2.2.1 Cooper pair box

The Cooper pair box was among the first superconducting devices to demonstrate properties of quantum coherence, including evidence for quantum superposition of charge states [54–57] and it was the first used to demonstrate coherent control of the quantum states of a qubit in a solid-state electronic device [29]. This device is composed of a small superconducting island bounded by a Josephson junction and a capacitor to ground, as shown in figure 2.2. The key

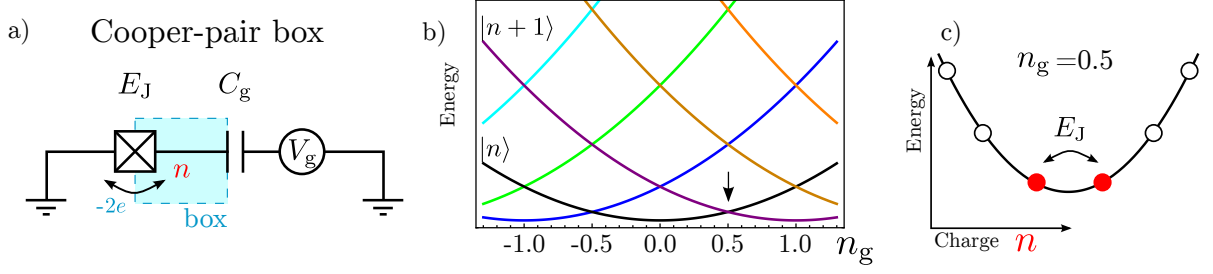


Figure 2.2: a) Circuit diagram of a single-junction CPB: a small superconducting island isolated by a Josephson junction and a capacitor to ground. The charge in the island is indicated by n , and this value can vary due to the tunneling through the Josephson junction or due to variations of the gate voltage. b) When the charge induced by the gate is $n_g = 1/2$, the energy levels of the charge states $|n\rangle$ and $|n+1\rangle$ are degenerate. c) The system can tunnel from a state to the other with a strength dictated by the Josephson energy E_J .

feature of this island is that it is sufficiently small that the charging energy required to add a Cooper pair to it is much larger than the thermal energy,

$$4E_C = 4 \frac{e^2}{2C_\Sigma} \gg k_B T \quad (2.7)$$

where $C_\Sigma = C_J + C_g$ is the total capacitance of the island and for typical values of the system's parameters must be less than a fF. The amount of charge on the island is induced by the gate and it is, expressed in number of Cooper pairs,

$$n_g = \frac{Q_g}{2e} = \frac{C_g V_g}{2e}. \quad (2.8)$$

The gate charge n_g is controlled by the voltage source V_g and is proportional to the gate capacitance C_g , consequently n_g is continuously tunable. The Hamiltonian of this system is a sum of two terms, proportional to the charging energy and to the Josephson energy in the island

$$\hat{H}_{\text{CPB}} = 4E_C(\hat{n} - n_g)^2 - E_J \cos \hat{\varphi}. \quad (2.9)$$

For the CPBs we have $E_C \gg E_J$, and so the number of Cooper pairs on the island is a well defined variable, it is hence a charge qubit. In particular, the first term in the Hamiltonian is the electrostatic energy, which plotted versus n_g gives a series of parabolae, each associated to a different discrete value of n . Tuning the gate voltage to the point where the charge induced by the gate is $n_g = 1/2$, the energy levels of the parabolae associated with charge states $|n\rangle$ and $|n+1\rangle$ are degenerate. Josephson tunneling between n and $n+1$ Cooper pairs on the island mixes these states and opens an avoided crossing with a strength dictated by the Josephson energy. This is the second term of the Hamiltonian, and it is the junction energy written in the phase basis. The mixing of charge states can be seen explicitly writing the Hamiltonian in the charge basis

$$\hat{H}_{\text{CPB}} = \sum_n \left[4E_C(\hat{n} - n_g)^2 |n\rangle\langle n| - \frac{E_J}{2} (|n\rangle\langle n+1| + |n+1\rangle\langle n|) \right]. \quad (2.10)$$

Expanding this Hamiltonian around the charge degeneracy point at $n_g = 1/2$, the CPB can be approximated by a two level system, taking the charge states to be $|0\rangle$ and $|1\rangle$,

$$\begin{aligned}\hat{H}_{\text{CPB}} &= -\frac{1}{2}[E_J\hat{\tau}_3 + 4E_C(1 - 2n_g)\hat{\tau}_1] \\ &\equiv -\frac{\hbar}{2}[\varepsilon\hat{\tau}_3 + \Delta\hat{\tau}_1]\end{aligned}\quad (2.11)$$

where

$$\begin{aligned}\hbar\Delta &= 4E_C(1 - 2n_g) \\ \hbar\varepsilon &= E_J.\end{aligned}\quad (2.12)$$

The CPB has a tunable gate charge n_g and can have also a tunable splitting at the avoided crossing by replacing the junction in the circuit with the DC SQUID equivalent junction introduced in 1.1.3. In this case, the Josephson energy is a function of the external magnetic field applied to the SQUID loop

$$E_J(\Phi_x) = E_{J,\text{max}} \left| \cos\left(\pi \frac{\Phi_x}{\Phi_0}\right) \right| \quad (2.13)$$

where the previous equation is valid for symmetric SQUID (a DC-SQUID composed by two equivalent JJ) and $E_{J,\text{max}} = E_{J1} + E_{J2}$.

From equation (2.11) we see that the Hamiltonian of the system is diagonal for $n_g = 1/2$ and the energy levels are first-order insensitive to charge noise. The CPB is read out using a single-electron transistor (SET) operated as a sensitive charge electrometer. The SET is a superconducting island isolated by two junctions. The drain and the source of the SET are the junction electrodes that connect to the island. When the SET is properly biased, current can flow from drain to source with a value that depends strongly on the gate-source voltage. The CPB island is coupled capacitively to the island and modifies the SET gate charge depending on its state. At the CPB charge-degeneracy point ($n_g = 1/2$), the SET cannot distinguish between $|0\rangle$ and $|1\rangle$, because their probability of detection are equal. This means that a readout can be done slightly away from the degeneracy point.

2.2.2 Quantronium and transmon

Quantronium was among the first design modifications of the CPB [58]. Quantronium manages to extend the dephasing times using the charge degeneracy point operation to mitigate low-frequency fluctuations. To measure the state of the qubit while remaining at the charge degeneracy point, a large junction is added in parallel to the CPB, forming a loop, as shown in figure 2.3 a). There is a magnetic flux threading this loop, controlling an additional degree of freedom and, thereby, a new noise channel. However, the energy of the system along the flux dimension also has a degeneracy point and the qubit is operated at this “double” charge-flux degeneracy point. In this way, to first order, the Quantronium is made insensitive to both charge

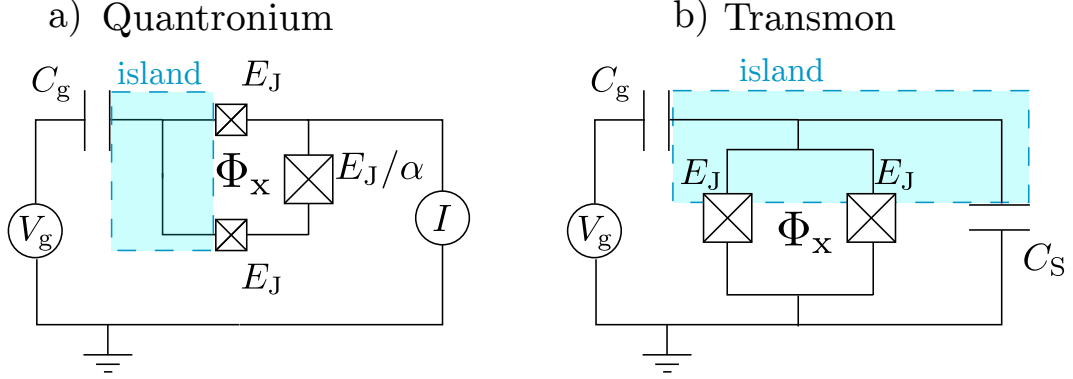


Figure 2.3: a) Circuit diagram of the quantronium. In this circuit the single Josephson junction in a CPB is replaced by two small junctions in parallel that are connected to a larger junction ($\alpha < 1$) to form a closed loop. The Cooper-pair box (island) is shown in light blue. The two states are now the two counter-rotating currents in the loop, which are observed by measuring the current I through the large junction. The system is controlled by a voltage V_g and the magnetic flux Φ_x . b) A transmon is a capacitively shunted CPB. Adding a large parallel capacitor to the CPB flattens the energy levels and makes the CPB much less sensitive to the charge fluctuations. The transmon may be realized either with a single junction or, as shown in the figure, with a tunable junction, namely a DC SQUID.

and flux noise, and dephasing times around 500 ns were enabled by this approach. [58]. Readout is performed by shifting the qubit away from the flux degeneracy point.

As the quantronium also the transmon is obtained slightly modifying a CPB. The transmon was developed by scientists at Yale University in 2007 [62, 65] and its name is an abbreviation of the term *transmission line shunted plasma oscillation qubit*. As shown in figure 2.3 b) a large capacitor is put in parallel to a Cooper pair box island in order to protect the qubit from fluctuations of offset charge of the superconducting island by flattening the transition frequency dependence on offset charge. The large capacitance influences mostly two qubit parameters, the anharmonicity and the charge dispersion. The anharmonicity is measured by the difference in energy between excitations of the system. If E_{10} and E_{21} are the energy differences between respectively the ground state and the first excited and between the first and second excited, the anharmonicity is denoted as $a = (E_{21}/E_{10}) - 1$: a harmonic oscillator has an anharmonicity of zero. While a large anharmonicity may not be fully exploitable, a small anharmonicity requires long qubit pulses in order to selectively excite only one pair of levels. Charge dispersion is the amount that the energy levels are dependent on the offset charge n_g on the island making up the qubit. The CPB energy levels are so dependent on charge such that the charge in the island must be kept constant using a gate voltage. The remarkable advantage of the transmon comes from the prediction that as the qubit parameter E_J/E_C is increased, the charge dispersion reduces exponentially and the anharmonicity decreases only with a power law. Because of this, with practical parameters, the charge dispersion can be made negligibly small while maintaining enough anharmonicity.

Aside from the different regime of parameters, the transmon Hamiltonian has the same form of the CPB.

2.3 Flux and phase qubits

In this section we will present the Flux qubits, which will be our main object of investigation throughout this theses. In the majority of the cases flux qubits are micrometer sized loops of superconducting metal interrupted by Josephson junctions. The junction parameters are engineered during fabrication so that a persistent current will flow continuously when an external flux is applied. The computational basis states of the qubit are defined by the circulating currents which can flow either clockwise or counter-clockwise. These currents screen the applied flux limiting it to multiples of the flux quantum and give the qubit its name. When the applied flux through the loop area is close to a half integer number of flux quanta the two energy levels corresponding to the two directions of circulating current are brought close together and the loop may be operated as a qubit. Computational operations are performed by pulsing the qubit with microwave frequency radiation which has an energy comparable to that of the gap between the energy of the two basis states. Properly selected frequencies can put the qubit into a quantum superposition of the two basis states while subsequent pulses can manipulate the probability amplitudes that the qubit will be measured in either of the two basis states, thus performing a computational operation.

In this section will be presented also the phase qubit, whose dynamics is described by its phase states. The phase qubit is closely related to the different types of flux qubit presented, yet distinct from them. A phase qubit is a current-biased Josephson junction, operated in the zero voltage state with a non-zero current bias. The connection between the two kind of qubit, (apart from the relation between flux and phase presented in paragraph 1.1.2) is given from the fact that a flux qubit is simply a flux biased phase qubit. For this reason the phase qubit will be the first qubit presented in this section.

2.3.1 Phase qubit

The phase qubit is a current-biased Josephson junction [1], Fig 2.4 a). When the junction is biased close to its critical current, the washboard potential of equation (1.11) is sufficiently tilted that a potential well accommodates only a few quantized states, which we will indicate with $|0\rangle, |1\rangle, |2\rangle$ and so on. In this limit, the local potential well is sufficiently anharmonic that the $|0\rangle \rightarrow |1\rangle$ transition can be distinguished from the $|1\rangle \rightarrow |2\rangle$ transition. In this regime, the state $|0\rangle$ is metastable, state $|1\rangle$ is relatively long-lived and state $|2\rangle$ tunnels rapidly. Qubit readout is performed by driving the transition $|1\rangle \rightarrow |2\rangle$. If the qubit were in state $|1\rangle$, it would quickly tunnel to state $|2\rangle$ if appropriately driven. If such a tunneling event happens there is a junction voltage which indicates a variation the junction phase, as it is possible to see from equation (1.6). within the two-level system model, the phase qubit Hamiltonian is essentially a pseudo spin with energy ω_{01} along $\hat{\tau}_3$ with a transverse component related to changes in the circulating current δI_{circ} . Changing the circulating current will also change the frequency ω_{01} . As a result,

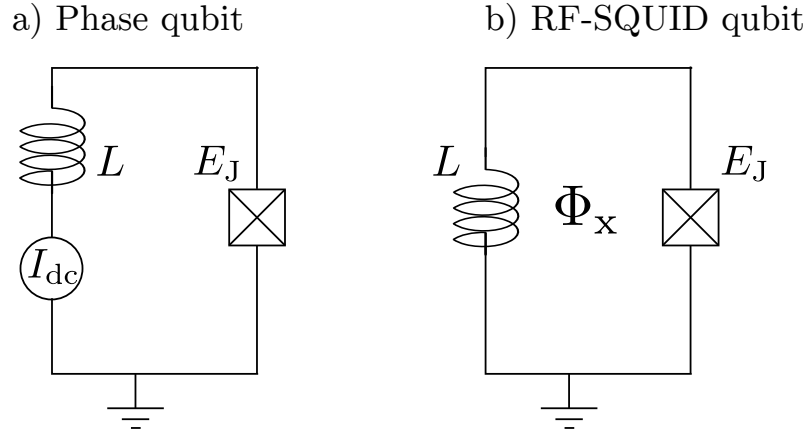


Figure 2.4: a) Single Josephson junction biased near its critical current is a phase qubit. The junction is bias such that the wells of the washboard potential shown in figure 1.2 have a few quantized states. Driving the transition from the first excited state to the second excited state constitutes readout, which creates a voltage if the qubit were in the first excited state, due to the tunneling from the second excited to the running state. b) Flux-biased phase qubit realizes a RF-SQUID.

the Hamiltonian is approximately [1, 66]

$$H_{pq} = -\frac{1}{2} \left[\hbar\omega_{01}\hat{\tau}_3 + \sqrt{\frac{\hbar}{2\omega_{01}C}} \delta I_{\text{circ}}(\hat{\tau}_1 + \chi\hat{\tau}_3) \right] \quad (2.14)$$

ΔU being the height of the barrier in the potential and $\chi = \sqrt{\hbar\omega_{01}/3\Delta U} \approx 1/4$ for typical parameters [66].

2.3.2 RF-SQUID qubit

The radio-frequency SQUID (RF-SQUID) is made by a Josephson junction placed in a loop of inductance L , threaded by a magnetic flux Φ_x [59] as shown in figure 2.4 b). The qubit potential energy U is the sum of the junction energy and the inductive energy due to the shunt inductance

$$U = -E_J \cos \phi + \frac{1}{2} E_L \left(\phi + 2\pi \frac{\Phi_x}{\Phi_0} \right)^2 \quad (2.15)$$

with E_L given by

$$E_L = \frac{(\Phi_0/2\pi)^2}{L}. \quad (2.16)$$

It is possible to redefine ϕ to move the flux dependence to the Josephson term

$$\varphi = \phi + 2\pi \frac{\Phi_x}{\Phi_0} \quad (2.17)$$

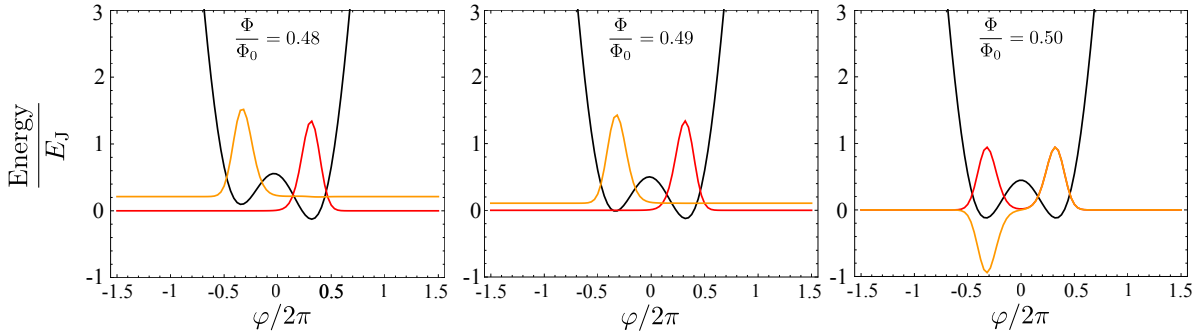


Figure 2.5: The black curve shows the potential energy of the RF SQUID as a function of the superconducting phase φ for $E_L/E_J = 0.4$ [59] and different values of the magnetic flux Φ . In the same plots the wave functions of the three lowest lying eigenstates ($E_C/E_J = 10^{-2}$) are depicted (red and orange lines) where the vertical offset indicates the corresponding eigenenergy.

The Hamiltonian of the RF-SQUID then becomes

$$\hat{H}_{\text{RFS}} = 4E_C(\hat{n} - n_g)^2 - E_J \cos\left(\hat{\varphi} - 2\pi\frac{\Phi_x}{\Phi_0}\right) + \frac{1}{2}E_L\hat{\varphi}^2 \quad (2.18)$$

where n_g represents fluctuating offset charges across the junctions, which can be removed through a gauge transformation $\psi'(\varphi) = e^{in_g\varphi}\psi(\varphi)$. With this change it is possible to rewrite the Hamiltonian as

$$\hat{H}_{\text{RFS}} = 4E_C\hat{n}^2 - E_J \cos\left(\hat{\varphi} - 2\pi\frac{\Phi_x}{\Phi_0}\right) + \frac{1}{2}E_L\hat{\varphi}^2 \quad (2.19)$$

From the Hamiltonian in equation (2.19) we see that tuning the external magnetic flux Φ_x effectively shifts the cosine wells along the parabola. The RF-SQUID is nominally operated near $\Phi_x = \Phi_0/2$, the value of the flux for which the potential of the qubit is a symmetric double well potential configuration. The height of the barrier between the two wells depends on the value of E_J . The two wells of the potential correspond to two different circulating current states, clockwise and counter-clockwise, and resonant tunneling through the double-well barrier will open an avoided crossing. For this reason, even if its Hamiltonian is the one of a flux-biased phase qubit, its mode of operation is most similar to the next qubit that will be presented, the persistent-current qubit. Even in the case of the RF-SQUID the single junction can be substituted by a DC-SQUID. The resulting circuit, called *double SQUID* [67] will be investigated in chapter 3, concentrating our attention on the modifications of its energy potential depending on the fast modification of the external flux bias.

The RF-SQUID was among the first flux qubits to demonstrate quantized energy levels and an avoided level crossing [59]. However, the small loop inductance, and therefore steep inductive potential, make RF-SQUID qubits very sensitive to flux bias, and therefore strongly susceptible to flux noise.

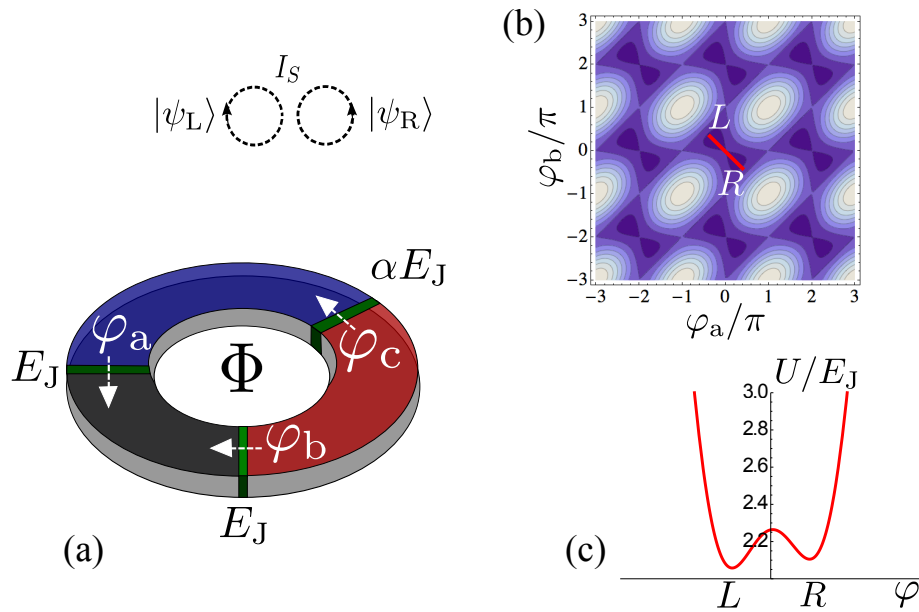


Figure 2.6: (a) Sketch of a persistent current qubit realised by a SQUID with three superconducting links, characterised in general by different phase differences, $\varphi_a, \varphi_b, \varphi_c$. The SQUID is penetrated by a magnetic flux Φ . The direction of the supercurrent circulating in the SQUID characterises the state of the persistent current qubit. (b) Potential landscape of the SQUID as a function of the phase differences for $\alpha = 0.75$ and $\Phi/\Phi_0 = 0.495$. The potential is 2π -periodic in φ_a and φ_b and it can be divided into equal square cells of side 2π . (c) Cut through the potential in the central cell of figure (b) along the line $\varphi = \varphi_a = -\varphi_b$ visualising the two minima corresponding to the qubit states of oppositely circulating currents.

2.3.3 Persistent current qubit

A persistent current qubit consists of a superconducting loop with three Josephson junctions, which encloses a flux Φ supplied by an external magnetic field [60, 61], as it is sketched in figure 2.6, sometimes this qubit is referred to as Delft qubit. The three junctions, $i = a, b, c$, are in general characterised by different Josephson energies E_J^i . In the Delft-qubit design, two of the junctions are equivalent, i.e. they have the same Josephson coupling energy $E_J^a = E_J^b \equiv E_J$, and the third junction has a smaller Josephson energy $E_J^c = \alpha E_J$, where $\alpha \leq 1$ is the asymmetry parameter. The different phase differences, φ_i , across the junctions (the arrows in figure 2.6 define the direction for a positive phase difference φ_i) are related to each other due to the fluxoid quantization as in equation (1.13) around the superconducting loop containing the junctions,¹

$$\varphi_a - \varphi_b + \varphi_c = -2\pi f . \quad (2.20)$$

The total Josephson energy of the ring is given by the phase-dependent expression $U = \sum_i E_J^i (1 - \cos \varphi_i)$. Combining this relation with the flux quantisation condition in (2.20) the Josephson energy can be written as

$$U = E_J [2 + \alpha - \cos \varphi_a - \cos \varphi_b - \alpha \cos(2\pi f + \varphi_a - \varphi_b)] . \quad (2.21)$$

The potential U is plotted in figure 2.6 (b) for $\alpha = 0.75$ and $f = 0.495$, a typical operation point of the Delft qubit. The plot shows a periodic structure of two nearby minima. These two minima, indicated by L and R, fulfill the condition $\varphi_a = -\varphi_b \equiv \varphi$ and correspond to situations in which the Josephson current in the loop has opposite signs. Due to the periodicity of the potential, all other minima are equivalent to L and R. If the magnetic flux is tuned to $f = \frac{1}{2}$ the two minima are equal, $U_{\min} = 2E_J (1 - \frac{1}{\alpha})$, and they are situated at $\varphi_{L/R} = \mp \arccos(1/2\alpha)$. Small deviations $\delta f = f - \frac{1}{2}$ from this point yield a shift of the minima by $\delta\varphi = -2\pi \delta f (2\alpha^2 - 1)/(4\alpha^2 - 1)$, such that $\varphi_{L/R} = \mp \arccos(1/2\alpha) + \delta\varphi$. Consequently, the potential becomes asymmetric as indicated in figure 2.6 (c) when a magnetic flux different from $f = 1/2$ is applied. For values $\alpha \leq 1/2$ the two minima would merge into a single minimum; in the following it will be assumed $\alpha > 1/2$.

The dynamics of the system is provided by the fact that each of the junctions adds a small electrical capacitance C . In fact the conjugate momentum to φ is given by the number of Cooper pairs $N = -i\hbar \partial/\partial\varphi$, which charge the capacitances. So the Hamiltonian takes the form

$$H_{\text{qubit}} = -4E_C \frac{\partial^2}{\partial\varphi^2} + E_J \left[2 + \alpha - 2 \cos(\varphi) - \alpha \cos(2\pi f + 2\varphi) \right] ; \quad (2.22)$$

the first term takes account for the charging energy $E_C = e^2/2C_\Sigma$, where C_Σ combines the capacitive effects of the three junctions, and the second term is the potential energy U as given in (2.21) with $\varphi = \varphi_a = -\varphi_b$. The low-energy physics of this system can be described by the two metastable states $|\psi_L\rangle$ and $|\psi_R\rangle$, corresponding to the ground states of the local minima of the potential as shown in figure 2.6 (c). They will serve as the two qubit states in the following. In the vicinity of the local minima, the Hamiltonian can be approximated using

¹Neglecting loop inductances.

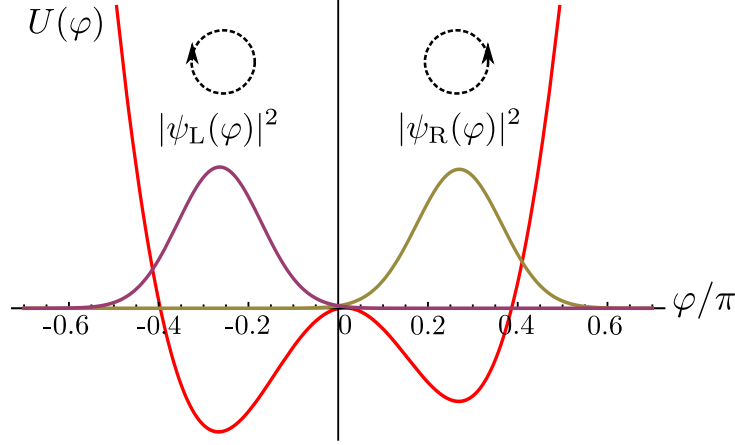


Figure 2.7: Cut through the potential of the SQUID along $\varphi = \varphi_a = -\varphi_b$, with the two approximated qubit states $|\psi_L\rangle$ and $|\psi_R\rangle$ in the phase representation for $\alpha = 0.75$ and $f = 0.495$.

$U(\varphi) \approx U(\varphi_{L/R}) + E_J [\cos(\varphi_{L/R}) + 2\alpha \cos(2\pi f + 2\varphi_{L/R})] (\varphi - \varphi_{L/R})^2$ for $\varphi \approx \varphi_{L/R}$. The qubit states are then given by the oscillator ground states

$$\langle \varphi | \psi_{L/R} \rangle = \left(\frac{\lambda_{L/R}}{\pi} \right)^{1/4} \exp \left\{ -\frac{\lambda_{L/R} (\varphi - \varphi_{L/R})^2}{2} \right\} \quad (2.23)$$

with the inverse of the variance

$$\begin{aligned} \lambda_{L/R} &= \frac{E_J}{2E_C} [\cos(\varphi_{L/R}) + 2\alpha \cos(2\pi f + 2\varphi_{L/R})] \\ &\approx \frac{E_J}{2E_C} \left[\frac{4\alpha^2 - 1}{2\alpha} \mp \frac{\pi(1+2\alpha^2)\delta f}{\alpha\sqrt{4\alpha^2 - 1}} \right] \end{aligned} \quad (2.24)$$

These states are shown in figure 2.7 together with the qubit potential. They are coupled through possible quantum tunnelling through the potential barrier between the two minima, whose height depends on the values of the asymmetry parameter, α , which is tuneable via the Josephson energy of the junction c . This can be done for instance by replacing junction c by a DC SQUID with a separately tuneable flux [23, 60]. However, as soon as the flux deviates from the value $\Phi = \Phi_0/2$ the qubit eigenstates occur to be well-localised in the potential wells, coupling between the two states is negligibly small and they are hence approximately given by $|\psi_L\rangle$ and $|\psi_R\rangle$. Usually the persistent current qubit dynamics is operated for $f = 1/2$, usually called “sweet spot”, where the energies of the two states of the qubit are degenerate and the qubit is first order insensitive to flux noise.

2.3.4 Fluxonium qubit

The fluxonium is a superconducting qubit whose electrical circuit is shown in figure 2.8: a small Josephson junction with Josephson energy E_J and capacitance C is shunted by an array of M

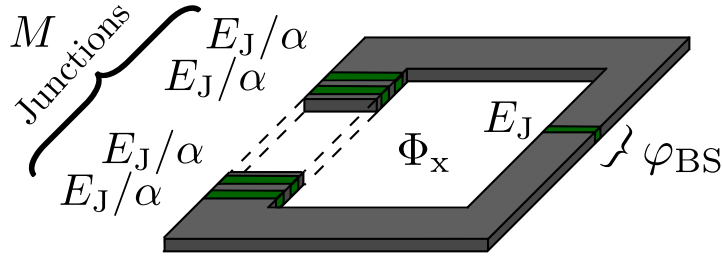


Figure 2.8: The fluxonium qubit consists of a superconducting loop interrupted by $M + 1$ Josephson junctions which is threaded by a magnetic flux Φ_x . In an effective description only the junction with the Josephson energy E_J and the phase difference φ_{BS} acts as a Josephson junction whereas the remaining M junctions with a larger Josephson energy E_J/α ($\alpha < 1$) act as a superinductance.

larger JJs characterized by Josephson energy E_J/α with $\alpha < 1$ [63]. When operated at microwave frequencies well below its self-resonant frequency $\sqrt{E_J E_C}/\alpha/\hbar$ with the charging energy $E_C = e^2/2C$, the array emulates a ‘superinductance’ which is an inductance whose impedance exceeds the superconducting impedance quantum $R_Q = \hbar/(2e)^2 \simeq 1 \text{ k}\Omega$. The superinductance has to be realized with Josephson junctions as it is impossible to realize using a conventional coil due to stray capacitances between the windings [63]. The Hamiltonian of the system consists of the kinetic energy $T = 4E_C \hat{n}_{BS}^2$, with the number operator $\hat{n}_{BS} = -i\partial/\partial\varphi_{BS}$ which is the conjugate variable to the superconducting phase difference φ_{BS} across the junction with the Josephson energy E_J (which from now on will be referred to as the ‘*black sheep*’). Additionally, the phase of the *black sheep* is exposed to the potential energy $U_{BS} = E_J(1 - \cos\varphi_{BS})$. Assuming that the M junctions constituting the superinductance are equivalent, they all will have the same superconducting phase difference φ_M . As a result the total potential energy is given by $U = U_{BS} + M(E_J/\alpha)(1 - \cos\varphi_M)$. If the size R of the superconducting loop is so small that $\Phi_0^2/R \gg E_J$ the fluxoid quantization takes the form [43]

$$\varphi_{BS} + M\varphi_M - 2\pi f = 0. \quad (2.25)$$

It is convenient to introduce the new variable $\varphi = M\varphi_M = -\varphi_{BS} - 2\pi f$ which denotes the phase difference across the superinductance. For large M at fixed φ , the phase difference φ_M across each junction in the array constituting the superinductance becomes small. As a result, it is possible to expand the cosine in the potential energy to second order and obtain

$$U = E_J \cos\varphi_{BS} + \frac{1}{2}E_L\varphi^2 \quad (2.26)$$

with E_L given by [63]

$$E_L = \frac{E_J}{\alpha M} = \frac{(\Phi_0/2\pi)^2}{L_{\text{eff}}} \quad (2.27)$$

where $L_{\text{eff}} \propto M$ denotes the effective superinductance emulated by the array of Josephson junctions. It is important to observe that it is the expansion of the cosine potential to second order in φ which removes the 2π periodicity of U as a function of φ and thus makes the device charge

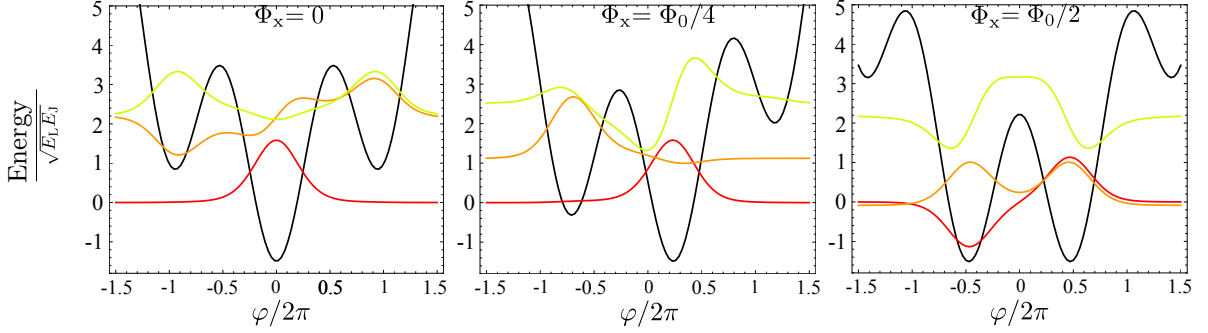


Figure 2.9: The black curve shows the potential energy of the fluxonium device as a function of the superconducting phase φ for $E_L/E_J = 5.8 \cdot 10^{-2}$ and different values of the magnetic flux Φ_x . In the same plots the wave functions of the three lowest lying eigenstates ($E_C/E_J = 2.8 \cdot 10^{-1}$) are depicted (rot, orange and green lines) where the vertical offset indicates the corresponding eigenenergy. The specific values of the energy are taken from Ref. [63].

insensitive, thus it is important to have a large number M of junctions. However, instantons connecting different minima of the potential U have to be suppressed and this effectively limits the maximal value of M which can be employed. The value of M consequently has to be a compromise between these two limitations [63]. In conclusion, the total Hamiltonian of the fluxonium is given by

$$H = T + U = 4E_C \hat{n}^2 + \frac{1}{2} E_L \hat{\varphi}^2 - E_J \cos(\hat{\varphi} - 2\pi f) \quad (2.28)$$

with $\hat{n} = -i\partial/\partial\varphi = -\hat{n}_{\text{BS}}$ the operator conjugate to $\hat{\varphi}$.

The Hamiltonian model thus obtained can describe a two level system, namely the so-called fluxonium qubit, if the conditions $E_J > E_C > E_L$ are satisfied. Figure 2.9 shows the potential as well as the wavefunctions for the lowest three energy levels of the Hamiltonian (2.28), evaluated in particular putting $E_L/E_J = 5.8 \cdot 10^{-2}$ and $E_C/E_J = 2.8 \cdot 10^{-1}$, which are the values for the energies used in Ref. [63], in correspondence to three different value of the flux control Φ_x . Let us observe that for $\Phi_x = 0$, the ground (g), first excited (e) and second excited (d) states form a V system, while a Λ system is provided near $\Phi_x = \Phi_0/2$. For intermediate flux bias, the (g) and (e) states are fluxon modes localized in two different wells. Moreover at $\Phi_x = \Phi_0/2$ the potential resembles that of a flux qubit, where the g and e states become the symmetric and antisymmetric superpositions of the degenerate fluxon modes. The stability of the g - d transition is exploited for reading out the qubit state. By placing the readout resonator frequency near the g - d transition frequency, the state of the qubit may be observed over the entire flux tunable range in a dispersive measurement.

For the scope of this thesis it is interesting to observe that if the value of the adimensional parameter f is not far from 0.5, namely for $\delta f = f - 0.5 < 0.3$ the qubit eigenstates are well-localized in the potential wells. Moreover, another important aspect to underline is that in the vicinity of a local minimum $\bar{\varphi}$ of the potential shown in figure 2.9, the energy potential can be

approximated using $U(\varphi) \approx U(\bar{\varphi}) + \frac{1}{2} [E_L + E_J \cos(\bar{\varphi} - 2\pi f)] (\varphi - \bar{\varphi})^2$, so the oscillator ground and first excited states can be taken as a good approximation of the qubit states. The qubit states are then given by

$$\langle \varphi | \psi_{g/e} \rangle = \left(\frac{\lambda_{g/e}}{\pi} \right)^{1/4} \exp \left[-\frac{\lambda_{g/e} (\varphi - \varphi_{g/e})^2}{2} \right] \quad (2.29)$$

with

$$\lambda_{g/e}^2 = \frac{1}{8E_C} [E_L + E_J \cos(\varphi_{g/e} - 2\pi f)], \quad (2.30)$$

where $\varphi_{g/e}$ are the positions of the two minima of the two deepest wells.

2.4 Sources of decoherence

This section will be devoted to introducing the most common sources of decoherence in a superconducting qubit. In general there are many channels through which a qubit may relax or dephase, ultimately leading to decoherence as we can see from equation (2.6). The strength of each channel depends on the qubit species, parameters, and experimental setup. At the end of the section, typical values of decoherence and relaxation times will be given for each qubit introduced in this chapter.

2.4.1 Relaxation sources

Relaxation of the qubit implies energy loss and thus any material through which an electric field is set or a current flows as part of the qubit mode, contributes to the total relaxation time of the qubit, usually indicated with \mathcal{T}_1 . In general, there are many sources of relaxation in every qubit, some of which may be orders of magnitude stronger than others. Important sources of relaxation are for example *capacitive losses*, due to each material in which electric field energy resides, and *inductive losses*, due to each material through which current travels. Also, the energy that leaves the qubit by radiation to the outside, introduces a *loss by radiation* contribution to the total relaxation term.

An example of a capacitive material loss is dissipation due to two level systems (TLS). Dielectric materials are often thought to have various defects both in the bulk and especially on their surface. Some of these defects may have two states with difference in energy close to the qubit excitation energy. In this case, the qubit may relax while exciting a defect TLS. Eventually the TLS may dissipate the energy in the form of phonons into the substrate, thus preparing the TLS to absorb more energy from the qubit.

Another typical relaxation contribution is given by the *Purcell effect* [68], which is responsible for radiation loss. The Purcell Effect is a relaxation mechanism which arises when the qubit is coupled to a cavity that is coupled to a microwave line for readout and drive purposes. The

strength of this coupling is controlled by the qubit-cavity coupling strength, the qubit-cavity detuning, and the cavity coupling quality factor.

Usually, one can think about these various loss mechanisms considering a resonant circuit representation in which each element comes with a resistor in parallel representing the loss associated to that component. The participation ratio of each component to the total loss, in this view, leads to different currents in different arms of the circuit. If there is a component with no current, its resistance does not count towards the total. In this way, for a generic qubit, one must include the junction inductance and capacitance, the environment capacitance and inductance, and the *Purcell effect*, which takes into account the loss by radiation term.

2.4.2 Dephasing sources

In a manner similar to relaxation, there are many possible sources of dephasing. Any microscopic or macroscopic process causing the qubit frequency to drift or fluctuate is a source of dephasing. The dephasing time usually is indicated with \mathcal{T}_ϕ and the sources which can contribute to it are *photon induced dephasing*, *offset charge noise*, *flux noise*, *critical current noise* and dephasing due to *quasiparticle tunneling*, which will be discussed in detail in chapter 4.

Photon induced dephasing [69] is due to the fact that coupling a qubit to a cavity introduces a term that makes the qubit frequency depend on the number of excitations in the cavity. If the number of photons in the cavity fluctuates, then so does the qubit frequency, giving a dephasing contribution.

The offset charge noise comes from offset charge fluctuations. For example, fluctuations of the offset charge on the island of the CPB induce frequency fluctuations. The sensitivity of a given qubit design to charge noise is characterized by the slope $\partial E_{ge}/\partial n_g$ where E_{ge} is the energy difference between the the ground state and the first excited state

$$\mathcal{T}_\phi \sim \frac{\hbar}{A_q} \left| \frac{\partial E_{ge}}{\partial n_g} \right|^{-1} \quad (2.31)$$

where A_q is a term denoting the amplitude of charge fluctuations, and may be of the order 10^{-3} or $10^{-4} e$ [70]. When the slope $\partial E_{ge}/\partial n_g$ goes to zero, small charge fluctuations do not shift the qubit frequency to first order, in this way sweet spot for charge noise occurs, meaning that this situation will be preferred to minimize the dephasing due to the offset charge.

Flux noise is another possible dephasing source, and results from flux fluctuations through a superconducting loop that influences the qubit frequency. The source of these fluctuations may be either from microscopic spins on the device surface or fluctuations of an externally applied field, for example. The sensitivity of a given qubit design to flux noise is characterized by the slope $\partial E_{ge}/\partial \Phi$ where Φ is the flux through the loop under consideration

$$\mathcal{T}_\phi \sim \frac{\hbar}{A_\Phi} \left| \frac{\partial E_{ge}}{\partial \Phi} \right|^{-1} \quad (2.32)$$

	CPB	Quantronium	Transmon	Phase qubit	RF-SQUID	Delft	Fluxonium
\mathcal{T}_1	5 ns	1 μ s	50 μ s	10 ns	20 ns	1 μ s	10 μ s
\mathcal{T}_2	5 ns	0.5 μ s	10 μ s	10 ns	20 ns	1 μ s	10 μ s

Table 2.1: Characteristic relaxation and decoherence times for the qubit in this chapter [1, 29, 58, 73–76]

where A_Φ is a term denoting the amplitude of flux fluctuations, and may be of the order of 10^{-5} or $10^{-6} \Phi_0$ [71]. Even for the flux noise, a sweet spot occurs when the slope $\partial E_{ge}/\partial\Phi$ goes to zero, meaning small flux fluctuations do not shift the qubit frequency to first order.

Yet another possible source of dephasing is critical current noise. The Josephson energy E_J is calculated using the critical current of the Josephson tunnel junction $E_J = \hbar I_c/2e$, and is physically derived from the thickness and area of the insulating layer. Fluctuations in critical current can then be converted into fluctuations in E_J , which in turn can be converted to fluctuations in qubit frequency. Dephasing times can be calculated in general as

$$\mathcal{T}_\phi \sim \frac{\hbar}{A_{I_c}} \left| \frac{\partial E_{ge}}{\partial I_c} \right|^{-1} \quad (2.33)$$

where A_{I_c} is a term denoting the amplitude of critical current fluctuations, and may be of the order of 10^{-6} or $10^{-7} I_c$ [72].

In the next chapters the attention will be concentrated on the study of coherences in flux qubits. In the third chapter the dynamics of a double SQUID when its energy potential is rapidly modified by flux pulses will be analyzed. This investigation will be based on experimental results obtained at the IFN-CNR by Chiarello et al. In the fourth chapter, the analysis will be centered on the Delft qubit and on the Fluxonium qubit, namely the more performant among the flux qubits presented in this chapter, both for relaxation and decoherence times.

Chapter 3

Exploiting quantum coherences in flux qubit systems

In this chapter we present two different studies concerning the exploitation of quantum coherences in flux qubit devices. Starting from an experiment performed at the IFN-CNR by Chiarello et al. [77], we will prove that the interplay of Landau-Zener transitions and quantum tunneling as well as the presence of quantum coherences in the initial state of a double SQUID can be the origin of an experimentally observed anomalous behavior. In particular, the population of the states of the double SQUID under study show a behavior which can be described theoretically using quantum coherence properties of the system. In other words, this experiment can be used as a witness of quantum coherences in the system, thus proving the quantum nature of a double SQUID.

In the second part of the chapter we show another important application of quantum coherence in superconducting qubits, namely the possibility of generating entangled states. In particular, we propose a generating scheme for a state with specific quantum coherences in a system composed by three flux qubits, taking into account the interaction of the system with its surroundings, modeled as bosonic baths.

3.1 Double SQUID manipulated by fast modification of its energy potential

Controlling and modifying the effective potential shape of superconducting devices is today possible with a fast and accurate tuning. This allows for example the observation of very fast oscillations of the magnetic flux states in a SQUID just by quickly changing its potential shape from a symmetric double well to a single one and back to the initial potential. For this kind of manipulation the rapidity of the modification of the effective potential shape is of great importance. For example, if we consider quantum computing applications, the manipulation

must be fast enough in order to induce non-adiabatic Landau-Zener transitions between the first two energy levels, which are used as computational space (namely the space generated by the states we are interested in). Landau-Zener transitions are non-adiabatic processes which can take place when a system has a time-dependent Hamiltonian varying such that the energy separation of the two states is a linear function of time. The Landau-Zener transition can be explained with an example. Let us put in the situation when the system starts, in the infinite past, in the lower energy eigenstate. For infinitely slow variation of the energy difference, the adiabatic theorem tells us that a transition to the upper energy state cannot take place and this because the system will always be in an instantaneous eigenstate of the Hamiltonian at that moment in time. At non-zero velocities, transitions can occur with a probability described by the Landau-Zener formula [78, 79]. The manipulation must also be slow enough in order to avoid transitions to upper levels (non computational space). Fortunately generally speaking this is possible thanks to an appropriate energy gap existing between the first couple of levels and the upper ones, but the transition rate is an aspect that must be accurately considered and calibrated [80]. In what follows we investigate the effects of the modification speed of the effective potential of a double SQUID discussing in detail the experimental observations obtained by Chiarello et al. [77] and the theoretical analysis we made in order to understand the physical origin of the observed behavior.

3.1.1 Experimental setup

The device considered in the experiment is the so called double SQUID [67], consisting of a superconducting loop of inductance L interrupted by a DC SQUID, a second smaller superconducting loop of inductance l interrupted by two identical Josephson junctions, each of (nominally) identical critical current i_0 and capacitance c (fig. 3.1a). As discussed in chapter 1, the DC SQUID behaves approximately like a single junction of capacitance $C = 2c$ and tunable critical current $I_0(\Phi_c) = 2i_0 \cos(2\pi\Phi_c/\Phi_0)$, which is controlled by a magnetic flux Φ_c applied to the small loop (this approximation holds if the loop is small enough, i.e for $li_0 \ll \Phi_0$). The double SQUID behavior can be controlled by two distinct magnetic fluxes, one applied to the large loop (Φ_x) and the second to the small one (Φ_c). As before discussed, it is useful to describe the SQUID dynamics by an equivalent mechanical model, with effective mass $m = C\Phi_0^2/4\pi^2$, effective position corresponding to the total magnetic flux threading the large loop (Φ), and potential

$$U = \frac{(\Phi - \Phi_x)^2}{2L} - \frac{I_0(\Phi_c)\Phi_0}{2\pi} \cos\left(2\pi\frac{\Phi}{\Phi_0}\right) \quad (3.1)$$

This effective potential can have one or two distinct wells, according to the adimensional parameter $\beta(\Phi_c) = 2\pi I_0(\Phi_c)L/\Phi_0$: in the particular case $\Phi_x = 0$ there will be a single-well for $\beta > -1$ (approximately an harmonic potential with a characteristic frequency controlled by Φ_c , fig. 3.1b), and two distinct wells separated by a barrier for $\beta < -1$ (with barrier height controlled by Φ_c , fig. 3.1c). The flux Φ_x controls the potential symmetry: for $\Phi_x = 0$ the potential is symmetric, otherwise it is tilted (fig. 3.1c).

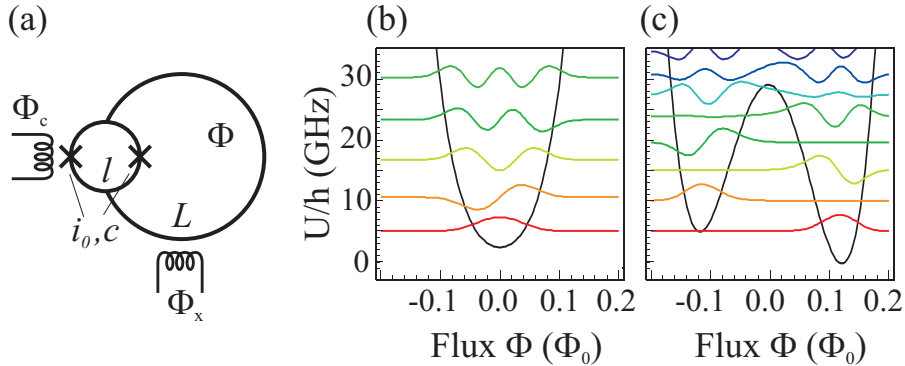


Figure 3.1: (a) Scheme of the double SQUID. (b) Effective potential of the double SQUID in the single-well case, with relative eigenwaves vertically shifted by the corresponding eigenenergies. (c) Double-well case with a slight asymmetry.

During the experiment a fast and large modification of the potential shape, from the single-well to the double-well case is realized. This is just one half of the complete manipulation of the qubit state presented in ref. [81, 82]. Initially the system is maintained in the single-well case for a rest time t_w . Then it is moved rapidly to the double-well case, where an high barrier separates the two minima, and this is obtained by changing the control flux Φ_c with a characteristic sweeping rate $\chi = \frac{d\Phi_c}{dt}$. Finally, a read out of the SQUID flux state is done, in order to observe which of the two minima is occupied at the end. This step is performed by an inductively coupled readout SQUID used as a magnetometer by means of measurements of the switching current [83]. The sequence is repeated many times in order to estimate the occupation probability P of the final flux state (for example, the probability to obtain a final right flux state). The complete operation is repeated for different unbalancing fluxes Φ_x . For slow (adiabatic) modifications we expect that the system remains always in its ground state: the left flux state when the left minima is the lower one (for $\Phi_x < 0$), and the right flux state in the opposite case (for $\Phi_x > 0$), with a smooth transition between these opposite cases around the symmetry point ($\Phi_x \approx 0$). In this case the probability P as a function of the unbalancing flux Φ_x presents a sigmoidal shape. By increasing the sweeping rate χ we expect an excitation of upper levels due to non adiabatic transitions, with a possible emerging of effects related to this population.

The measurements [77] were performed on devices realized by standard trilayer Nb/AlO_x/Nb technology, with nominal parameters $L = 85\text{pH}$, $l = 7\text{pH}$, $I_0 = 8\mu\text{A}$ and $c = 0.3\text{pF}$, in a dilution refrigerator with base temperature $T = 30\text{mK}$ arranged for ultra low noise qubit measurements (mu-metal, superconducting and normal metal shields, thermocoax and L-C-L filters on dc lines, different attenuator stages on the signal line). A preliminary study of the switching current in the readout DC SQUID gives an escape temperature of about 250 mK, compatible with the crossover temperature within the experimental errors. This indicates the absence of an excess temperature due to noise [83]. The probability P is evaluated by repeating the preparation - modification - readout cycles for 1000 times at a rate of 10 kHz. The initial preparation is

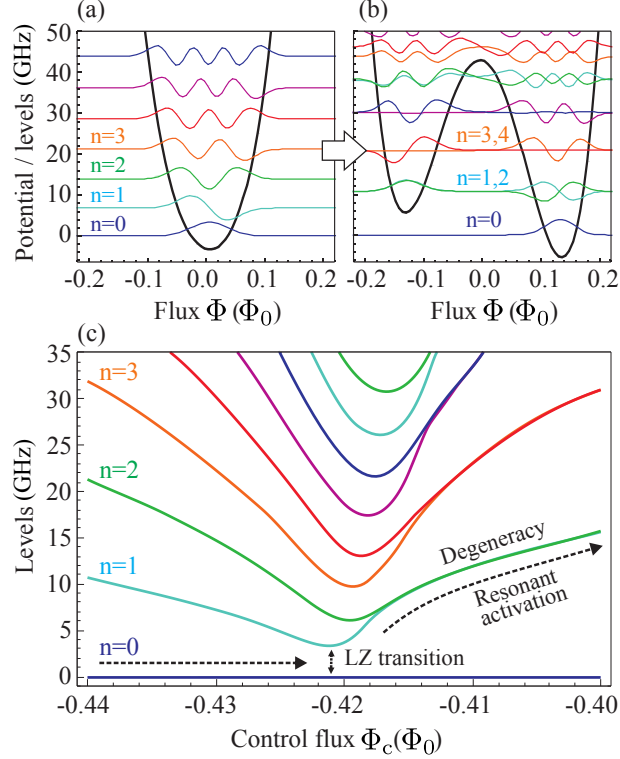


Figure 3.2: (a) Energy potential of the system and relative eigenstates in the single-well case (for $\Phi_c = -429 \text{ m}\Phi_0$). (b) Energy potential of the system and relative eigenstates in the double-well case (for $\Phi_c = -412 \text{ m}\Phi_0$), with a slight asymmetry ensuring the degeneracy (for $\Phi_x = 0.543 \text{ m}\Phi_0$). (c) Variation of the energy levels positions for different fluxes Φ_c (for $\Phi_x = 0.543 \text{ m}\Phi_0$). Note that for convenience all energies are expressed as frequencies in GHz, and are shifted by subtracting the ground state energy.

obtained by waiting for a time $t_w = 200\text{ns}$ in the single-well condition (fig. 3.2a), for $\Phi_c \approx -480 \text{ m}\Phi_0$. In this condition the system is well approximated by an harmonic oscillator with characteristic frequency $\approx 19\text{GHz}$, corresponding to a level spacing of about 0.91K , very high with respect to the thermal bath temperature, so that we expect a negligible thermal excitation.

The potential shape modification is driven by a fast pulse generator, presenting signals with a typical rise time $t_R = 0.8\text{ns}$ that can be changed by using a tunable L-C-L filter. The modified pulse is fully characterized thanks to a fast oscilloscope, in particular it is possible to check the pulse shape and the actual rise time. The fast signal is transmitted to the device thanks to a 50Ω matched coaxial cable interrupted by three 20dB attenuators placed at 300 K , 1 K and 30 mK stages. More details on the setup can be found in ref. [81]. The entire line was tested at room temperature and in the absence of the chip, while the present setup does not allow to test the entire system (line plus chip) at low temperature. For this reason a large error in the determination of the real signal shape and rise time at the device level can be expected. The applied signal modifies the potential from the single-well condition, at $\Phi_c \approx -480\text{m}\Phi_0$, to the double-well case, at $\Phi_c \approx -360\text{m}\Phi_0$, passing through the critical condition $\Phi_c \approx -422\text{m}\Phi_0$

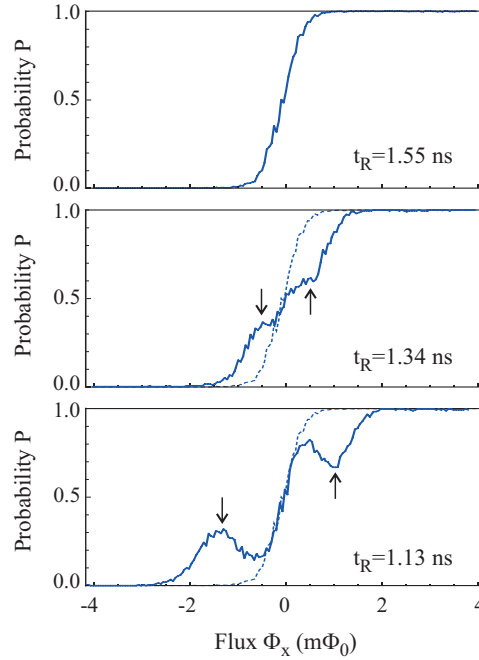


Figure 3.3: Experimental results for the probability P to measure a right flux state for different unbalancings Φ_x at three different rise times t_R . Resonance peaks are visible for faster transitions (arrows in second and third plots) [77]

where there is the transition between the single-well and double-well conditions (fig. 3.2). At the end of each cycle the final flux state is measured by the coupled readout DC SQUID. This is done by applying a current ramp to the SQUID and recording the switching current, which is directly related to the qubit flux. The sequence is repeated for different unbalancing fluxes Φ_x , ranging from $-4m\Phi_0$ to $+4 m\Phi_0$.

3.1.2 Experimental results

The probability curves obtained after the sequence of measurement for different unbalancing fluxes are plotted in figure 3.3. These curves in particular correspond to three different rise times, $t_R = 1.55$ ns, $t_R = 1.34$ ns and $t_R = 1.13$ ns. In the top plot we observe the sigmoidal function expected for a slow rate. In the middle and lower plots two distinct order of peaks appear, respectively at about $\pm 0.55m\Phi_0$ and $\pm 1.1m\Phi_0$. The measurement can be repeated for different rise times obtaining the 3-dimensional curve shown in fig. 3.4.

In fig. 3.4 we observe the following characteristics. First of all the position of peaks (in Φ_x) corresponds to the conditions for which different levels in the two wells are aligned (degenerate) (fig. 3.2b). This strongly suggest that the presence of peaks is a manifestation of resonant

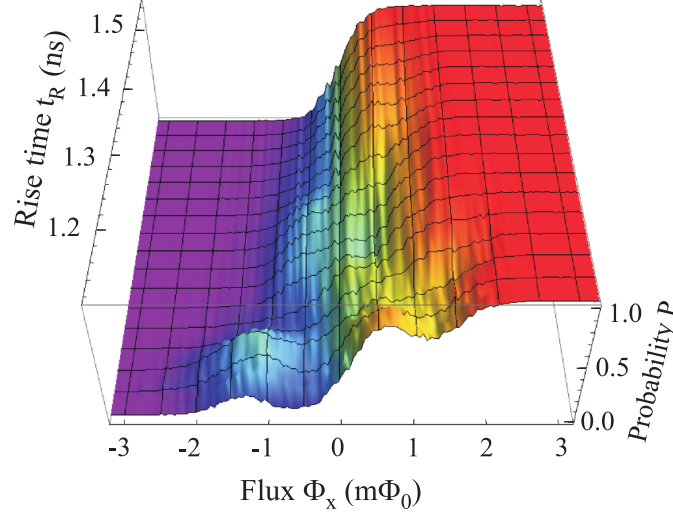


Figure 3.4: Experimental results for the probability P to measure a right flux state for different unbalancings Φ_x at different rise times t_R , plotted as a 3D surface. [77]

tunneling between wells. Secondly we note that the appearing of peaks requires rise times below a particular critical value, namely it is necessary to have a high enough sweep-rate in order to observe peaks. Thirdly, there is an alternation of peaks' set: when the second set of peaks appears, the first set disappears. In fig. 3.2 c it is plotted the modification of the first nine energy levels in the passage from the single-well to the double-well condition (in the degenerate case for $\Phi_x = 0.55 m\Phi_0$). This figure can help us in a qualitative explanation of the observed peaks. In the single-well condition (on the left) it appears reasonable to suppose that only the ground state is populated. Close to the critical point $\Phi_c \approx -0.42m\Phi_0$, where the barrier appears to separate two distinct wells, Landau-Zener transitions lead to a population of the upper levels, with an efficiency depending on the sweep-rate $\frac{d\Phi_c}{dt}$. These excited states can cross the barrier thanks to a resonant tunneling when the alignment condition is met. The experimental results thus suggest that these two effects combine and produce the observed peaks, due to an excess of population in the upper well when the resonant and the non-adiabatic conditions are both fulfilled. The region where this effect is active is small, of the order of 1/10 of the entire span of the flux Φ_c ($120 m\Phi_0$), and this region is crossed in a similar fraction of the entire rise time duration, about 0.1ns. We stress again that the combination of Landau-Zener and resonant tunneling can explain the first two observations (position of peaks and their appearance only below a critical rise time), but not the third one, that is the alternation of peaks' set. In the next section we will give a more detailed theoretical analysis of the system, in order to gain information about possible physical mechanisms and/or properties of the system which may be responsible for the appearance of the alternation of peaks' set as in fig. 3.4

3.1.3 The theoretical analysis

In what follows we describe a more quantitative analysis we developed [77], exploiting a simple quantum model useful to describe the system under scrutiny. In order to do this we start considering the Hamiltonian model relative to the potential (3.1)

$$H(t) = -\frac{1}{2m} \frac{\partial^2}{\partial \varphi^2} + m\Omega^2 \frac{(\varphi - \varphi_x)^2}{2} + m\Omega^2 \beta(t) \cos(\varphi), \quad (3.2)$$

where $\Omega = 1/\sqrt{LC}$, $\varphi = 2\pi\Phi/\Phi_0$ and $\varphi_x = 2\pi\Phi_x/\Phi_0$. Also $\beta(t) = -I_0(\Phi_c(t)) \frac{\Phi_0}{2\pi m\Omega^2}$. The Hamiltonian (3.2) is well suited to describe the time evolution of a particle in one dimensional time-dependent potential. In particular, appropriately choosing the function $\beta(t)$, it is possible to vary the potential shape from a single to a double-well, in a time interval \tilde{t} , thus reproducing the initial and final conditions of the experiment discussed before. The problem therefore consists in finding the probability P that, at the end of the process, the particle is found in the right well as function of both the unbalancing parameter φ_x as well as of the rise time t_R . Let's observe that knowing the state of the system $|\Psi(\tilde{t})\rangle$ at the time instant \tilde{t} , this probability can be simply evaluated as

$$P(\tilde{t}) = \int_{\text{right well}} \Psi^*(\tilde{t})\Psi(\tilde{t})d\varphi \quad (3.3)$$

Let's indicate by $|\psi_n(t)\rangle$ a set of instantaneous eigenfunctions of the Hamiltonian (3.2):

$$H(t)|\psi_n(t)\rangle = E_n(t)|\psi_n(t)\rangle \quad (3.4)$$

Exploiting these states, we can write

$$|\Psi(t)\rangle = \sum_{n=0}^{\infty} \exp[i \int_0^t E_n(t')dt'] \cdot s_n(t) \cdot |\psi_n(t)\rangle \quad (3.5)$$

where the $|s_n(t)|^2$ are the populations of the instantaneous eigenstates $|\psi_n(t)\rangle$. The function $s_n(t)$ are solutions of the following set of integro-differential equations:

$$\dot{s}_n(t) = - \sum_{k=0}^{\infty} M_{nk}(t) \exp[i \int_0^t (E_n(t') - E_k(t'))dt'] s_k(t). \quad (3.6)$$

with $M_{nk}(t) = \langle \psi_n(t) | \dot{\psi}_k(t) \rangle$. Starting from eqs. (3.3) and (3.5), the probability P can then be written as

$$\begin{aligned} P(\tilde{t}) &= \sum_{n=0}^{\infty} |s_n(\tilde{t})|^2 \int_{\text{right well}} \psi_n^*(\tilde{t})\psi_n(\tilde{t})d\varphi \\ &\equiv \sum_{n=0}^{\infty} |s_n(\tilde{t})|^2 L_n \end{aligned} \quad (3.7)$$

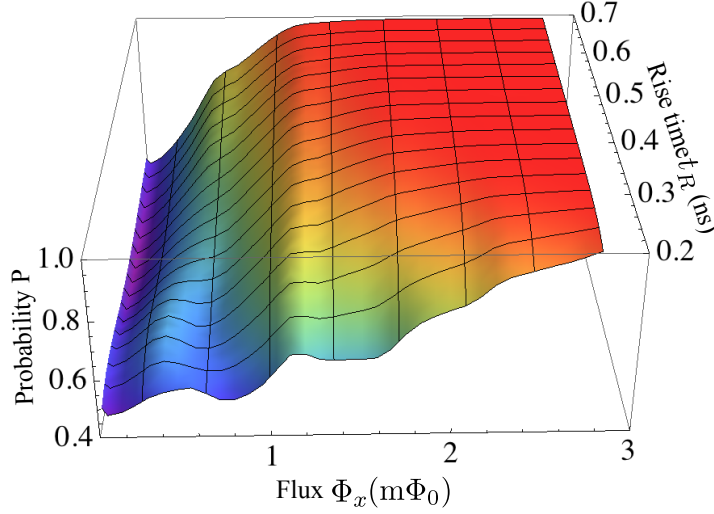


Figure 3.5: Probability P to find the system in the right well against the unbalancing Φ_x and rise time t_R , supposing that at $t = 0$ it is in its ground state. [77]

with

$$L_n = \int_{\text{right well}} \psi_n^*(\tilde{t}) \psi_n(\tilde{t}) d\varphi \quad (3.8)$$

Given the difficulties of calculating an exact analytical solution of the coupled integro-differential equations (3.6), we proceed further by performing numerical simulations of the dynamical behavior of the system carefully taking into account both the non adiabaticity in the system dynamics and the possible emergence of resonant tunneling processes. As first step, considering $\beta(t)$ as a parameter, we numerically diagonalize the Hamiltonian (3.2) at a generic time instant t , finding its instantaneous eigenvectors $|\psi_n(t)\rangle$ and the correspondent eigenvalues $E_n(t)$.

Considering values of t_R of interest in the context of this paper, we have evaluated the quantity L_n , defined in eq. (3.8), in correspondence to different values of n . As expected, at least for not too large n , L_n is either almost equal to one or negligible, witnessing that the first eigenstates are practically localized for $\Phi_x \neq 0$. In our simulation however we use the numerical value of L_n instead of 0 or 1.

To evaluate the probability P we thus need to calculate the populations $|s_n(\tilde{t})|^2$ by numerically solving the equations (3.6) explicitly giving the way in which the potential shape modifies itself going from the initial condition to the final one during the time \tilde{t} . In other words, we now must choose the function $\beta(t)$ appearing in equation (3.2). We wish to underline that this is a very delicate point. It is undoubted indeed that the dynamics of the system will be deeply affected by the way of varying the potential shape. Thus we expect to find different results in correspondence to different choices of $\beta(t)$.

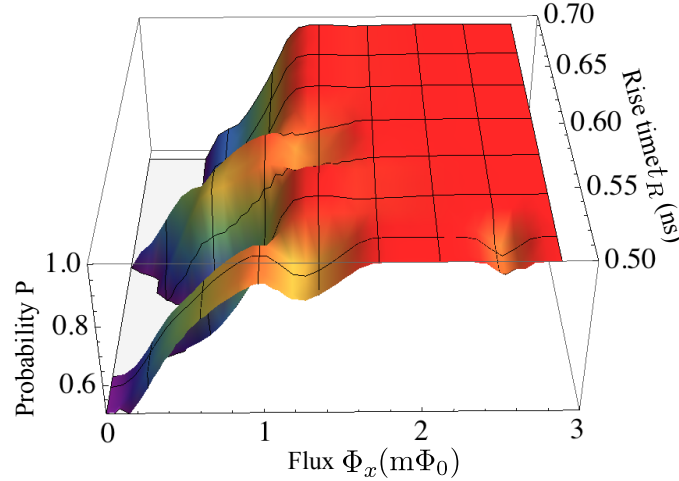


Figure 3.6: Probability P to find the system in the right well against the unbalancing Φ_x and rise time t_R , supposing that at $t = 0$ it is in the linear superposition $|\Psi(0)\rangle = x|\psi_0(0)\rangle + e^{i\theta}\sqrt{(1-x^2)}|\psi_1(0)\rangle$ of its ground and first excited states in correspondence to $x = 0.95$ and $\theta = 0$. [77]

3.1.4 Theoretical results and conclusive remarks

Taking into account the considerations presented in section 3.1.3, it appears reasonable fixing the $\beta(t)$ shape as a sigmoidal function. In particular we put it as $\beta(t) = \beta(0)(1 - \zeta(t)) + \beta(\tilde{t})\zeta(t)$ with $\zeta(t) = \frac{\text{Erf}((2t/\tilde{t}-1)w-s) - \text{Erf}(-w-s)}{\text{Erf}(w-s) - \text{Erf}(-w-s)}$, $\text{Erf}(x) = \frac{2}{\sqrt{\pi}} \int_0^x e^{-t^2} dt$. This function contains two parameters w and s , which respectively control how much the slope of the sigmoidal function is shifted in time and how steep its slope is. We stress that varying the value of these two parameters implies a change in the rise time t_R . In our simulation the parameters have been chosen as $w = 2$ and $s = 0.3$, in order to obtain a sufficiently steep slope and a correspondent appropriate rise time.

In order to investigate the appearance of peaks in fig. 3.4, we have calculated the probability of finding the particle in the right well for different values of $\Phi_x = \varphi_x \Phi_0 / 2\pi$ supposing, as it appears physically reasonable, that at $t = 0$ the system is in its ground state. This was supposed as a consequence of the waiting time t_w in which the system has been put in the single well condition. In particular we evaluated this probability considering a range of Φ_x in which the peaks appear, as suggested by the experimental data. Considering values of t_R as in figure 3.4, our simulation does not evidence the existence of significant peaks. However, by taking into account the fact that the peaks in the probability P arise reducing the rise time, and in view of the experimental uncertainties before discussed, we have simulated the behavior of the system exploring smaller t_R . The results obtained are reported in figure (3.5) where the probability P is plotted as a function of both Φ_x and t_R . As expected, resonance peaks appear at different values of Φ_x . However the position of such peaks with respect to the rise time t_R does not reflect the experimental observations neither qualitatively nor quantitatively. In other words even if a dependence of P on t_R is evident, the function $P(t_R)$ is very different from the experimental

one. In particular the probability P obtained by simulation (see fig. 3.5) is not characterized by the alternation of peaks' set as in figure 3.4. This result moreover does not seem to be imputable to the particular choice of the $\beta(t)$ we made. We have indeed verified that this is the case by choosing a linear function and obtaining the same qualitative behavior of that shown in fig. 3.5. If it is true that the manner in which we modify the potential shape deeply affects the dynamics of the system and thus the probability P that the system is found in the right well at the end of the potential modification, another key ingredients to be considered is surely the state of the system at $t = 0$. Taking into account the fact that the temperature at which the experiment is performed is $\sim 30mK$, it is reasonable to suppose that at $t = 0$ there is a small, but not zero (of the order of few percent), probability that the system is in its first excited state. It could be thus reasonable to assume that the preparation step leaves the system in a mixture $\rho = x^2|\psi_0(0)\rangle\langle\psi_0(0)| + (1 - x^2)|\psi_1(0)\rangle\langle\psi_1(0)|$ of the ground and the first excited state. Performing simulations starting from this mixture instead of the ground state, we have verified that, considering values of x compatible with $T \simeq 30mK$, we do not get significant differences with respect to the results displayed in fig. 3.5. We have also checked that increasing the relative weight x of the first excited state in the initial mixture worsens the accordance between theoretical predictions and experimental results. The theoretical prediction instead drastically changes if we suppose that quantum coherences are present in the initial state of the system. Such an assumption can be justified by considering the fact that the waiting interval of time t_w was not long enough to allow the complete destruction of the coherences between the ground and the first excited state of the double SQUID. If this is the case, it is reasonable to assume that at $t = 0$ the system is in a quantum superposition $|\Psi(0)\rangle = x|\psi_0(0)\rangle + e^{i\theta}\sqrt{(1 - x^2)}|\psi_1(0)\rangle$ of the first two low-lying states, instead of a mixture of the two states as before supposed. Starting from this initial state the probability P shows a dependence on both Φ_x and t_R as displayed in fig. (3.6) where we have considered a smaller range of t_R to better appreciate the behavior of P . As expected, also in view of experimental uncertainties on the function $\beta(t)$ as well as on the parameters defining the system, figure (3.6) does not exactly match the experimental results presented before, even if the qualitative behavior of P seems to be well reproduced. More in detail the most important aspect of the results shown in fig. (3.6) consists in the fact that, as experimentally observed, there is an alternation of the peaks' set determined by both the asymmetry in the potential governed by the value of the unbalancing parameter Φ_x , and on the rise time t_R required to go from a single to a double-well.

The theoretical analysis developed in this paper has the merit to disclose the role played by the persistence of quantum coherences in the initial state of the double SQUID. We wish to stress indeed that starting from an initial state as the ground state of the qubit or a mixture of the same ground state and the first excited one, even if leading to the appearance of peaks, is completely unable to predict the alternance of minima and maxima as requested by the experimental results. Thus our assumption, that is the persistence of quantum coherences, leads to predictions in good qualitative agreement with the experimental results. The intriguing point is that all the alternative seemingly more reasonable assumptions concerning the initial state of the SQUID predict a behavior not compatible with some aspect of the observed one.

Before concluding this section we wish to spend some words about possible decoherence

effects in the dynamical behavior of the system. It is important to stress that, as we have previously discussed, the temporal interval where the physical mechanisms at the basis of the observed effects are active is a small fraction (of the order of 0.1 ns) of the total duration of the experiment (about 1 ns). As first approximation it is thus reasonable to neglect decoherence effects in the system dynamics, which present time scales of the order of nanoseconds. Anyway it is the case to underline that in this context the source of noise is the $\frac{1}{f}$ noise [84] that generally speaking acts modifying the effective control parameter as for example Φ_x [85–87]. We thus expect that the effects of such a noise on the results reported in figure 3.6 would consist at most in a broadening of the observed peaks.

3.2 GHZ state generation of three Josephson qubits in presence of bosonic baths

Since its introduction, quantum entanglement has played a central role in foundational discussions of quantum mechanics. More recently, also due to the advent of new more applicative areas, the concept of entanglement has attracted a renewed interest from the scientific community. Entangled quantum states in multipartite systems are those states which interact in ways such that the quantum state of each part of the system cannot be described independently, instead, a quantum state may be given for the system as a whole. Entangled states have indeed proved to be essential resources for example both for quantum information processing and computational tasks. For this reason, in the last few years many efforts have been devoted to the design and the implementation, in very different physical areas, of schemes aimed at generating entangled states [8, 9, 11–13, 15–21]. In this context, in particular, superconductive qubits turned out to be promising candidates providing their scalability and the possibility of controlling and manipulating their quantum state in situ via external magnetic field and voltage pulses [52, 88–90].

Having as final target the realization of states characterized by prefixed quantum correlations, it is obviously important to estimate the effects of the coupling between the system considered and its surroundings.

Recently Galiautdinov and Martinis [8] have presented a protocol suitable for generating maximally entangled states, namely *GHZ* (Greenberger - Horne- Zeilinger state) and *W* states [91], of three Josephson qubits. The key idea on which their proposal is based, is that for implementing symmetric states, as the *GHZ* and *W* are, it is convenient to symmetrically control all the qubits in the system. In particular, making use of a triangular coupling interaction scheme and exploiting single qubit local rotations, they demonstrate the possibility of generating the desired state appropriately setting the interaction time between the qubits. In their analysis, however, the authors considered the system as an ideal one, without taking into account in any way its unavoidable coupling with uncontrollable external degrees of freedom. In the next section will be presented the investigation we did [92], following the idea proposed in ref. [8], on the effects of the environment on the generation of *GHZ* states. More in detail, we concentrated our attention on all the external degrees of freedom that can be effectively mod-

eled as independent bosonic modes taking into account their presence from the very beginning. We moreover exploited the same triangular coupling mechanism envisaged in ref. [8], but we modified the single qubit rotation protocols with respect the ones of Galiutdinov and Martinis. Our analysis clearly proves that the scheme for generating GHZ states is stable enough against the noise sources we consider.

3.2.1 Ideal generation scheme

3.2.1.1 Galiutdinov - Martinis entangling protocol

In this section we briefly summarize the single step entangling protocol, proposed by Galiutdinov and Martinis in order to generate the three-qubits *GHZ* states

$$|GHZ\rangle = \frac{1}{\sqrt{2}}(|000\rangle + e^{i\varphi}|111\rangle) \quad (3.9)$$

being $|0\rangle$ and $|1\rangle$ the ground and excited states of each qubit respectively. In particular we review only some aspects of the procedure that are of interest for our further investigations. The Hamiltonian model describing the physical system consisting of three Josephson qubits with pairwise coupling, is given by

$$H = \sum_{i=1}^3 \left(\frac{\omega}{2} \tau_3^i + \frac{1}{2} [g(\tau_1^i \tau_1^{i+1} + \tau_2^i \tau_2^{i+1}) + \tilde{g} \tau_3^i \tau_3^{i+1}] \right) \quad (3.10)$$

with $\tau_k^4 = \tau_k^1$ ($k = x, y, z$). Introducing the collective operators

$$\mathbf{S} = \sum_{j=1}^3 \frac{\boldsymbol{\tau}^j}{2} \quad (3.11)$$

we can rewrite equation (3.10) in the following more convenient form

$$H = \omega S_z + g S^2 - (g - \tilde{g}) S_z^2 \quad (3.12)$$

within a constant term. Starting from equation (3.12) it is evident that the eigenstates of the system can be written as common eigenstates $|s_{12}, s, m\rangle$ of the operators $S_{12}^2 = [\frac{1}{2}(\boldsymbol{\tau}^1 + \boldsymbol{\tau}^2)]^2$, S^2 and S_z :

$$\begin{aligned} S_{12}^2 |s_{12}, s, m\rangle &= s_{12}(s_{12} + 1) |s_{12}, s, m\rangle \\ S^2 |s_{12}, s, m\rangle &= s(s + 1) |s_{12}, s, m\rangle \\ S_z |s_{12}, s, m\rangle &= m |s_{12}, s, m\rangle \end{aligned} \quad (3.13)$$

In particular it is immediate to convince oneself that the two states

$|000\rangle \equiv \left| s_{12} = 1, s = \frac{3}{2}, s_z = -\frac{3}{2} \right\rangle$ and $|111\rangle \equiv \left| s_{12} = 1, s = \frac{3}{2}, s_z = \frac{3}{2} \right\rangle$ are eigenstates of

H correspondent to the eigenvalues $-\frac{3}{2}\omega + \frac{3}{4}(2g + 3\tilde{g})$ and $\frac{3}{2}\omega + \frac{3}{4}(2g + 3\tilde{g})$ respectively. In view of these considerations it is clear that, if at $t = 0$ the three qubits are in their respective ground state, in order to guide the system toward the desired state (3.9) it becomes necessary to implement some local rotations before turning on the interaction mechanism described by the Hamiltonian (3.10). This is what Galiautdinov and Martinis do, making thus sure to obtain an initial condition having both $|000\rangle$ and $|111\rangle$ components. The entanglement is then performed by switching on, for an appropriate interval of time $t_{\text{int}} = \frac{\pi}{2(g-\tilde{g})}$, the interaction described by equation (3.10) and finally by realizing an additional single-qubit rotation. The scheme thus consists of three different steps: in the first and the third ones, the Josephson qubits are independent and are driven by external fields in order to appropriately rotate their state. In the second step instead the three qubits are coupled thus producing the desired entanglement among them.

3.2.1.2 Single-qubit rotations

As we have underlined in section 3.2.1.1, starting from the initial condition $|000\rangle$ the interaction mechanism described in equation (3.10) can be usefully exploited for generating GHZ states of three qubits, only if local rotation operations are realized as first and final steps of the procedure, whose duration is hereafter indicated by t_1 and t_3 respectively. These two distinct operations of the protocol require a total time of realization $t_{13} = t_1 + t_3$, which has to add to the length of the qubit interaction interval $t_{\text{int}} = \frac{\pi}{2(g-\tilde{g})}$, if we wish to estimate the total duration of the generation scheme. Thus the choice of the physical mechanism able to perform appropriate single qubit rotations, could be usefully exploited to control the time required to generate the desired state starting from the state $|000\rangle$. This aspect is of particular interest especially when the presence of external degrees of freedom is not negligible. At the light of these considerations we have chosen rotation mechanisms different from those envisaged in ref. [8]. In particular we suppose that in the first, as well as in the last step of the scheme, the system of the three qubits is described by the following Hamiltonian

$$H_{\text{rot}}^l = \sum_{j=1}^3 H_{\text{rot}}^l(j) \quad (l = I, III) \quad (3.14)$$

with

$$H_{\text{rot}}^l(j) = \frac{\omega}{2}\tau_3^j + \frac{\omega}{2}\left(e^{i\beta_l}\tau_-^j + \text{h.c.}\right) \quad (3.15)$$

where

$$\begin{aligned} \beta_I &= \pi\left(\frac{1}{\sqrt{2}} + 1\right) \\ \beta_{III} &= \pi\left(\frac{3+\sqrt{2}}{2}\right) + \pi\left(\frac{(3+\sqrt{3})\omega}{8(g-\tilde{g})}\right). \end{aligned} \quad (3.16)$$

In ref. [93] it is discussed a possible way to realize a Hamiltonian model like that given by equation (3.14) is discussed in detail, showing in particular that a full control of qubit rotations on the entire Bloch sphere can be achieved.

It is possible to prove that setting $t_1 = t_3 = \frac{\pi}{\sqrt{2}\omega}$, the sequence of the three steps leads to the desired *GHZ* states when the interaction between the system of the three Josephson qubits and the external world may be neglected. After some calculations indeed we obtain that at $t = t_1$ the state of the system is given by

$$|\psi(t_1)\rangle = \frac{1}{\sqrt{8}} \left(|000\rangle + |111\rangle e^{-\frac{3i\pi}{\sqrt{2}}} + \sqrt{3}|W\rangle e^{-\frac{i\pi}{\sqrt{2}}} + \sqrt{3}|W'\rangle e^{-\sqrt{2}i\pi} \right). \quad (3.17)$$

where

$$|W\rangle = \frac{1}{\sqrt{3}} (|100\rangle + |010\rangle + |001\rangle) \quad (3.18)$$

and

$$|W'\rangle = \frac{1}{\sqrt{3}} (|011\rangle + |101\rangle + |110\rangle). \quad (3.19)$$

At $t = t_1$ the interaction mechanism described by equation (3.10) is switched on for a time $t_{\text{int}} = \frac{\pi}{2(g-\tilde{g})}$. At the end of this second step the state of the system will be

$$\begin{aligned} |\psi(t_1 + t_{\text{int}})\rangle &= \frac{1}{\sqrt{8}} \left(|000\rangle + |111\rangle e^{-\frac{3i\pi}{2} \left(\frac{\omega}{g-\tilde{g}} + \sqrt{2} \right)} + \right. \\ &\quad \left. - \sqrt{3}|W\rangle e^{i\pi \left(\frac{(\sqrt{3}-3)\omega}{4(g-\tilde{g})} - \frac{\sqrt{2}}{2} \right)} - \sqrt{3}|W'\rangle e^{-i\pi \left(\frac{(\sqrt{3}+3)\omega}{4(g-\tilde{g})} + \sqrt{2} \right)} \right). \end{aligned} \quad (3.20)$$

Thus the last step of the procedure described by H_{rot}^{III} , leads the system into the final state

$$|\psi(t_1 + t_{\text{int}} + t_3)\rangle = \frac{1}{2} \left[(i + e^{i\alpha})|000\rangle + ie^{-i\theta}(i - e^{i\alpha})|111\rangle \right] \quad (3.21)$$

with

$$\begin{aligned} \alpha &= \frac{3\pi\omega(\sqrt{3}-1)}{8(g-\tilde{g})} \\ \theta &= \frac{3\pi\sqrt{2}}{2} + \frac{3\pi\omega(\sqrt{3}+3)}{8(g-\tilde{g})}. \end{aligned} \quad (3.22)$$

Starting from equations (3.21) and (3.22) it is immediate to convince oneself that, if the condition

$$\frac{\omega}{g-\tilde{g}} = \frac{8k}{3(\sqrt{3}-1)} \quad k \in \mathbb{N} \quad (3.23)$$

is satisfied, the three Josephson qubits are left in the desired *GHZ* state.

Thus we can say that the time required to generate the state (3.9) starting from the condition $|000\rangle$ can be estimated as

$$t_{\text{tot}} = t_1 + t_{\text{int}} + t_3 = \frac{\sqrt{2}\pi}{\omega} + \frac{\pi}{2(g-\tilde{g})}. \quad (3.24)$$

This value of t_{tot} has to be compared with a time $t_{\text{tot}} = \frac{\pi}{\Omega} + \frac{\pi}{2(g-\tilde{g})}$, with $\Omega \ll \omega$ required if the procedure of Galiautdinov and Martinis is adopted. The proposal of Galiautdinov and Martinis

requires that in the first and in the last step of the procedure the dynamics of each qubit is governed by the following Hamiltonian model [8, 94]

$$H_{\text{GM}}^{I,III} = \sum_j H_{\text{GM}}^{I,III}(j) \quad (3.25)$$

where

$$H_{\text{GM}}^{I,III}(j) = \frac{\omega}{2}\tau_z^j + \Omega \cos(\omega t + \phi_{I,III})\tau_x^j \quad (3.26)$$

with $\Omega \ll \omega$ and $\phi_I = -\frac{\pi}{2}$ $\phi_{III} = 0$. Thus, changing the way to rotate the state of the three qubits during the first and the last step of the procedure, it is possible to reduce the time required to generate the target state. As said before, this aspect is of particular relevance when the interaction of the system with the external world is not negligible. The price to pay anyway is that in our case, differently from the scheme of Galiautdinov and Martinis, three qubit GHZ states can be generated only if the condition given in equation (3.23) is satisfied. Generally speaking, indeed, at the end of the procedure, the three Josephson qubits are left in a linear superposition of the two states $|000\rangle$ and $|111\rangle$ with amplitudes $A_{000} = \frac{1}{2}(i + e^{i\alpha})$ and $A_{111} = \frac{i}{2}e^{-i\theta}(i - e^{i\alpha})$ respectively. It is important, however, to stress that the condition (3.23) is compatible with typical values of the free frequency ω , that generally speaking can be taken of the order of 10GHz, and with the values of the coupling constants g and \tilde{g} , that reasonably can be assumed of the order of 1GHz and 10^{-1} GHz respectively [7, 23, 66, 95]. On the other hand, condition (3.23) is not as restrictive as it appears, since we have verified that variations of ten percent in the ratio $\frac{\omega}{g-\tilde{g}}$ are still compatible with the requirement that $|A_{000}|^2 \simeq |A_{111}|^2$.

3.2.1.3 Microscopic master equation derivation

In a realistic description of the scheme until now discussed, we cannot neglect the presence of uncontrollable external degrees of freedom coupled to the three Josephson qubits that, generally speaking, affects in a bad way quantum state generation protocols. These degrees of freedom, that define the so-called environment, can have different physical origin and thus different descriptions. In this section we will focus our attention on all the external degrees of freedom describable as independent bosonic modes [96–104]. More in detail, we will suppose that during all the process each qubit is coupled to a bosonic bath and the three baths are independent.

The plausibility of this assumption can be tracked back to the fact that the three superconductive qubits are spatially separated so that it is reasonable to suppose that each of them is affected by sources of noise stemming from different parts of the superconductive circuit. In this section we review all the three steps of the procedure discussed before, analyzing the dynamics of the system by considering from the very beginning the interaction of each qubit with a bosonic bath. In order to do this we will construct and solve microscopic master equations in correspondence to the three different steps described in section 3.2.1.2 in which the generation scheme is structured. In each of the three steps the master equation will be derived in the Born - Markov and Rotating wave approximations. In appendix B a more detailed derivation of the master equation is given in these two approximations. We wish to stress at this point that the

use of microscopic master equations instead of more naive and more popular phenomenological ones, becomes important particularly when structured bosonic baths are considered [105].

3.2.1.4 First step: single-qubit rotation

Let us suppose that the three Josephson qubits are initially prepared in the ground state $|000\rangle$ and that the Hamiltonian describing the system in the first step of the procedure is given by equation (3.14) with $l = I$. Moreover, each qubit is coupled to a bosonic bath and the three baths are independent. The Hamiltonian model describing the system in the first step can thus be written as [106]

$$H_1 = H_{\text{rot}}^I + H_B + H_{\text{int}} \quad (3.27)$$

with

$$\begin{aligned} H_B &\equiv H_B(1) + H_B(2) + H_B(3) = \\ &= \sum_k \omega_k^1 a_k^{1\dagger} a_k^1 + \sum_k \omega_k^2 a_k^{2\dagger} a_k^2 + \sum_k \omega_k^3 a_k^{3\dagger} a_k^3 \end{aligned} \quad (3.28)$$

and

$$\begin{aligned} H_{\text{int}} &= \tau_1^1 \otimes \sum_k g_k^1 (a_k^1 + a_k^{1\dagger}) + \tau_1^2 \otimes \sum_k g_k^2 (a_k^2 + a_k^{2\dagger}) + \\ &+ \tau_1^3 \otimes \sum_k g_k^3 (a_k^3 + a_k^{3\dagger}). \end{aligned} \quad (3.29)$$

Exploiting a standard procedure [107], briefly illustrated in Appendix B, we now derive the microscopic master equation suitable to describe the dynamics of the three qubits system. Taking into account the fact that the qubits, as well as the baths, are, in this case, independent, it is enough to construct and solve the master equation correspondent to a single superconductive qubit. Indicating by $\rho_j(t)$ the density matrix of the j -th ($j = 1, 2, 3$) qubit, it is possible to prove that during the first step we have

$$\begin{aligned} \dot{\rho}_j(t) &= -i[H_{\text{rot}}^I(j), \rho_j(t)] \\ &+ \gamma_1(\omega_1) \left(A_j(\omega_1) \rho_j(t) A_j^\dagger(\omega_1) - \frac{1}{2} \{ A_j^\dagger(\omega_1) A_j(\omega_1), \rho_j(t) \} \right) \\ &+ \gamma_1(\omega_2) \left(A_j(\omega_2) \rho_j(t) A_j^\dagger(\omega_2) - \frac{1}{2} \{ A_j^\dagger(\omega_2) A_j(\omega_2), \rho_j(t) \} \right) \end{aligned} \quad (3.30)$$

where the Bohr frequencies are respectively $\omega_1 = \sqrt{2}\omega$ and $\omega_2 = 0$. The correspondent operators, describing the jumps between the eigenstates $|\psi_{\pm\epsilon}\rangle_j$ ($\epsilon = \frac{\omega}{\sqrt{2}}$), of the Hamiltonian $H_{\text{rot}}^I(j)$, are

given by

$$\begin{aligned}
A_j(\omega_1) &\equiv |\psi_{-\epsilon}\rangle_{jj}\langle\psi_{-\epsilon}|\tau_x^j|\psi_\epsilon\rangle_{jj}\langle\psi_\epsilon| = \\
&= \left(\frac{1}{\sqrt{2}}\cos\frac{\pi}{\sqrt{2}} - i\sin\frac{\pi}{\sqrt{2}}\right)|\psi_{-\epsilon}\rangle_{jj}\langle\psi_\epsilon| \\
A_j(\omega_2) &\equiv |\psi_{-\epsilon}\rangle_{jj}\langle\psi_{-\epsilon}|\tau_x^j|\psi_{-\epsilon}\rangle_{jj}\langle\psi_{-\epsilon}| + |\psi_\epsilon\rangle_{jj}\langle\psi_\epsilon|\tau_x^j|\psi_\epsilon\rangle_{jj}\langle\psi_\epsilon| = \\
&= \frac{1}{\sqrt{2}}\cos\frac{\pi}{\sqrt{2}}\left(|\psi_{-\epsilon}\rangle_{jj}\langle\psi_{-\epsilon}| - |\psi_\epsilon\rangle_{jj}\langle\psi_\epsilon|\right)
\end{aligned} \tag{3.31}$$

with

$$\begin{aligned}
|\psi_\epsilon\rangle_j &= \frac{1}{2}\left[\sqrt{2+\sqrt{2}}e^{-i\beta_I}|1\rangle_j + \sqrt{2-\sqrt{2}}|0\rangle_j\right] \\
|\psi_{-\epsilon}\rangle_j &= \frac{1}{2}\left[\sqrt{2-\sqrt{2}}e^{-i\beta_I}|1\rangle_j - \sqrt{2+\sqrt{2}}|0\rangle_j\right].
\end{aligned} \tag{3.32}$$

Concerning the decay rates $\gamma_1(\omega_1)$ and $\gamma_1(\omega_2)$ appearing in equation (3.30), we will fix their numerical value in the next section where we explicitly give the spectral properties of the baths.

3.2.1.5 Second step: entangling procedure

As we have previously discussed, the next step requires that the three qubits interact among them through the coupling mechanism described by the Hamiltonian H , given in (3.12). In addition each qubit interacts with a bosonic bath. Thus the Hamiltonian describing the total system in this second step can be written as

$$H_2 = H + H_B + H_{\text{int}}. \tag{3.33}$$

The master equation for the density matrix of the three qubits during the second step can be written in the form

$$\begin{aligned}
\dot{\rho}(t) &= -i[H, \rho(t)] + \\
&+ \sum_{j=1}^3 \sum_{k=1}^8 \gamma_2(\omega_k) \left(A_j(\omega_k) \rho(t) A_j^\dagger(\omega_k) - \frac{1}{2} \{ A_j^\dagger(\omega_k) A_j(\omega_k), \rho(t) \} \right)
\end{aligned} \tag{3.34}$$

where the Bohr frequencies are the following

$$\begin{aligned}
\omega_{1,3} &= \frac{3-\sqrt{3}}{2}\omega \pm 2(g-\tilde{g}) \\
\omega_{2,4} &= \frac{3}{2}\omega \mp (g+2\tilde{g}) \\
\omega_5 &= \sqrt{3}\omega \\
\omega_{6,7} &= \frac{\sqrt{3}}{2}\omega \pm 3g \\
\omega_8 &= 0
\end{aligned} \tag{3.35}$$

whereas the jump operators between the eigenstates of the Hamiltonian (3.12) are given for convenience in appendix C.2. We wish to underline that equation (3.34) does not contain mixed terms of the form $A_j(\omega_k)\rho(t)A_{j'}^\dagger(\omega_k) - \frac{1}{2}\{A_j^\dagger(\omega_k)A_{j'}(\omega_k), \rho(t)\}$ with $j \neq j'$ since the three bosonic baths are independent.

We have solved the master equation (3.34), considering as initial condition the solution of the master equation (3.30) obtained in the previous paragraph at $t = t_1$. More in detail, taking into account the fact that the ideal scheme provides a dynamics confined in the subspace generated by the states $|000\rangle$, $|111\rangle$, $|W\rangle$ and $|W'\rangle$, we have focused our attention on the projection of $\rho(t)$ on this subspace. It is possible indeed to prove that the neglected subspace will be at the most populated with a probability not exceeding the 3%.

3.2.1.6 Third step: local rotations

To complete the analysis of the GHZ state generation procedure in presence of noise, we must construct the microscopic master equation describing the system in the last step of the scheme. Actually it can be immediately deduced from the master equation derived in the first step simply substituting β_I with β_{III} in the eigenstates $|\psi_{\pm\epsilon}\rangle$ appearing in the jump operators. However, in this case it is more convenient to write the jump operators exploiting the basis

$$\begin{aligned}
|\widetilde{000}\rangle &= T|000\rangle \\
|\widetilde{111}\rangle &= T|111\rangle \\
|\widetilde{W}\rangle &= T|W\rangle = \frac{1}{\sqrt{3}}T(|100\rangle + |010\rangle + |001\rangle) \\
|\widetilde{W'}\rangle &= T|W'\rangle = \frac{1}{\sqrt{3}}T(|011\rangle + |101\rangle + |110\rangle) \\
|\widetilde{\psi}_1\rangle &= T|\psi_1\rangle = \frac{1}{\sqrt{2}}T(|100\rangle - |010\rangle) \\
|\widetilde{\psi}'_1\rangle &= T|\psi'_1\rangle = \frac{1}{\sqrt{2}}T(|011\rangle - |101\rangle) \\
|\widetilde{\psi}_2\rangle &= T|\psi_2\rangle = \frac{1}{\sqrt{6}}T(|100\rangle + |010\rangle - 2|001\rangle) \\
|\widetilde{\psi}'_2\rangle &= T|\psi'_2\rangle = \frac{1}{\sqrt{6}}T(|011\rangle + |101\rangle - 2|110\rangle).
\end{aligned} \tag{3.36}$$

instead of the standard one. In this new basis the unitary operator T can be represented as

$$T = \frac{\sqrt{2 + \sqrt{2}}}{8} \begin{pmatrix} B_1 & & 0 \\ & B_2 & \\ 0 & & B_3 \end{pmatrix} \tag{3.37}$$

with

$$\begin{aligned}
B_1 &= \begin{pmatrix} -(2+\sqrt{2}) & -(4-3\sqrt{2}) & \sqrt{6} & -\sqrt{3}(2-\sqrt{2}) \\ -(4-3\sqrt{2})e^{-3i\beta_{III}} & (2+\sqrt{2})e^{-3i\beta_{III}} & \sqrt{3}(2-\sqrt{2})e^{-3i\beta_{III}} & \sqrt{6}e^{-3i\beta_{III}} \\ \sqrt{6}e^{-i\beta_{III}} & \sqrt{3}(2-\sqrt{2})e^{-i\beta_{III}} & (3\sqrt{2}-2)e^{-i\beta_{III}} & -(4-\sqrt{2})e^{-i\beta_{III}} \\ -\sqrt{3}(2-\sqrt{2})e^{-2i\beta_{III}} & \sqrt{6}e^{-2i\beta_{III}} & -(4-\sqrt{2})e^{-2i\beta_{III}} & -(3\sqrt{2}-2)e^{-2i\beta_{III}} \end{pmatrix} \\
B_2 &= \begin{pmatrix} 4e^{-i\beta_{III}} & 4(\sqrt{2}-1)e^{-i\beta_{III}} \\ 4(\sqrt{2}-1)e^{-2i\beta_{III}} & -4e^{-2i\beta_{III}} \end{pmatrix} \\
B_3 &= \begin{pmatrix} 4e^{-i\beta_{III}} & 4(\sqrt{2}-1)e^{-i\beta_{III}} \\ 4(\sqrt{2}-1)e^{-2i\beta_{III}} & -4e^{-2i\beta_{III}} \end{pmatrix}
\end{aligned}$$

It is possible to demonstrate that in this case the master equation can be written as

$$\begin{aligned}
\dot{\rho}(t) &= -i[H_{\text{rot}}^{III}, \rho(t)] + \\
&+ \sum_{j=1}^3 \sum_{i=1}^2 \gamma_3(\omega_i) \left(A_j(\omega_i) \rho(t) A_j^\dagger(\omega_i) - \frac{1}{2} \{ A_j^\dagger(\omega_i) A_j(\omega_i), \rho(t) \} \right)
\end{aligned} \tag{3.38}$$

where the Bohr frequencies are the same as those in the first step whereas the jump operators $A_j(\omega_i)$ between the eigenstates of the Hamiltonian H_{rot}^{III} are for convenience given in the appendix C.3.

3.2.2 Dissipation due to coupling to ohmic bosonic baths

Having at disposal the microscopic master equations (3.30), (3.34) and (3.38), describing the dynamics of the three-qubit system, we have found the density matrix $\rho(t_{\text{tot}})$ of the system at the time instant $t_{\text{tot}} = t_1 + t_{\text{int}} + t_3$, supposing that at $t = 0$ the initial condition was $|\psi(0)\rangle = |000\rangle$. Moreover, we have assumed that all the three baths are characterized by the same spectral density given in particular by the ohmic one

$$\gamma(\omega) = \begin{cases} \gamma_0 & \omega = 0 \\ \alpha\omega & \omega \neq 0 \end{cases} \tag{3.39}$$

where γ_0 is introduced in order to take into account a non zero decay rate for $\omega = 0$. In my master thesis work I studied the same problem with the hypothesis of a flat spectrum. Now we are improving the calculation, since transitions with higher Bohr frequencies are here more damped. The ohmic spectrum implies that the ratio between the decay rates is equal to the ratio between the correspondent Bohr frequencies.

To quantify the effects of the bosonic baths we can consider the fidelity F

$$F = \text{Tr}\{\rho_{\text{exp}}\rho(t_{\text{tot}})\} \tag{3.40}$$

that gives an idea of the difference existing between the density matrix ρ_{exp} , obtained when the interaction with the three baths is neglected, and the density matrix $\rho(t_{\text{tot}})$. The results we have

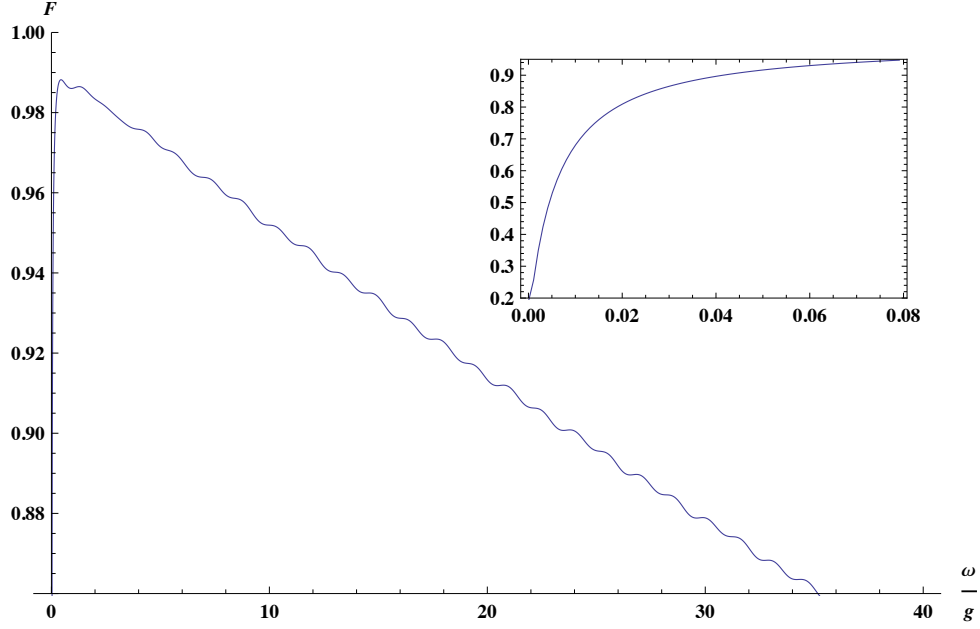


Figure 3.7: Fidelity F as a function of ω/g when we assume that all the three baths are characterized by the same ohmic spectral density given in (3.39) with $\gamma_0/g = \alpha = 10^{-3}$ and the parameters assume the values $\tilde{g}/g = 0.1$. The inset shows the Fidelity for values $0 < \omega/g < 0.08$.

obtained are given in figure 3.7 where we plot F as a function of the ratio ω/g assigning to the parameters γ_0 and α physically reasonable values. In particular we have chosen $\gamma_0/g = \alpha = 10^{-3}$ [7, 23, 66, 95].

The fidelity shown in figure 3.7 slowly decreases for increasing values of ω/g , as it is expected from the form of the dissipation constants given in (3.39). As we can see, at least for $\omega \lesssim 20g$ the presence of bosonic baths at zero temperature does not affect in a significant way the dynamics of the system during the different steps of the procedure, the fidelity not being less than 0.9. One should expect that the fidelity F is a monotonically decreasing function of ω/g . The model we have used for the decay rate (see eq.(3.39), however, is discontinuous for zero frequency because we want to consider also possible dephasing channels. Due to this discontinuity one is not allowed to perform the limit ω/g tending to zero in the fidelity. Anyway this is not a problem as for $\omega = 0$ our scheme is meaningless since in this limit no rotations are performed. Moreover, as the inset in figure 1 shows, the increase of F is rapid with respect to ω/g . Let us now observe that increasing the bath decay rates by an order of magnitude, the fidelity F remains experimentally significant as shown in figure 3.8.

Both figures make evident that the presence of the three independent bosonic baths do not affect in a dramatic way the results reached under the hypothesis of perfect isolation.

We are interested in the generation of GHZ states as given in equation (3.9), which, as we have previously seen, can be obtained only if the condition (3.23) is satisfied. Thus it is of

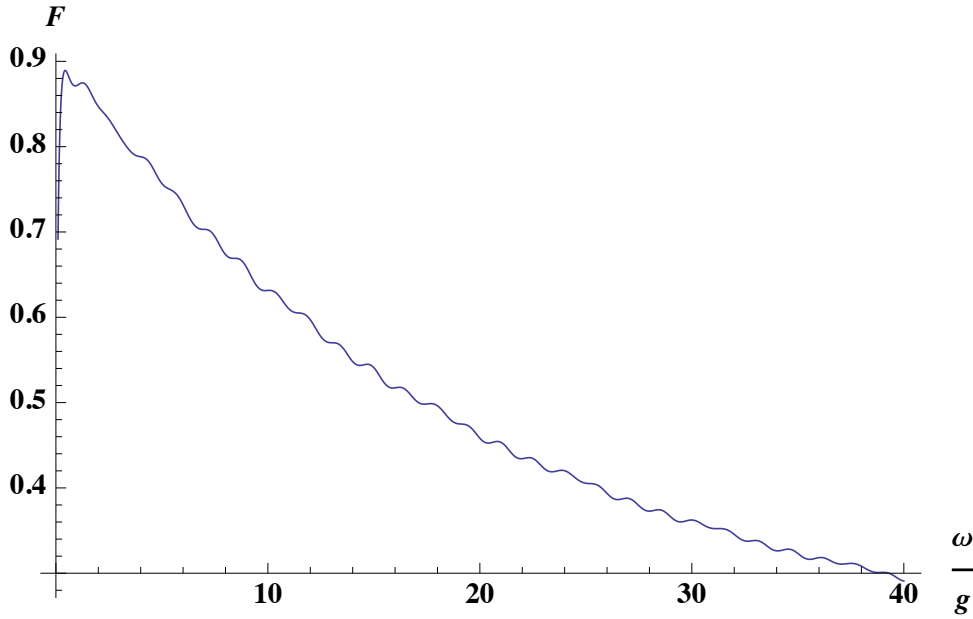


Figure 3.8: Fidelity F as a function of ω/g when we assume that all the three baths are characterized by the same ohmic spectral density given in (3.39) with $\gamma_0/g = \alpha = 10^{-2}$ and the parameters assume the values $\tilde{g}/g = 0.1$.

interest for us to analyze the fidelity F_{GHZ} defined as

$$F_{GHZ} = \text{Tr}\{|GHZ\rangle\langle GHZ|\rho(t_{\text{tot}})\} \quad (3.41)$$

and reported in figures 3.9 and 3.10 as a function of the ratio ω/g .

Figure 3.9 is obtained for realistic bath decay rates generally reported in literature [7, 23, 66, 95]. The results shown in figure 3.10 are obtained supposing worse conditions. As expected, the fidelity F_{GHZ} shows maxima at values of ω/g which satisfy condition (3.23). The value of such maxima moreover decreases increasing the ratio ω/g . This circumstance is in turn related to the fact that the decay rates appearing in the master equations (3.30), (3.34) and (3.38), are increasing functions of ω . However, also considering the worst case we may conclude that it is possible to choose an interval of values of the ratio ω/g for which F_{GHZ} is greater than 0.7. On the other hand for experimentally reasonable values of the decay rates γ_0 and α we can obtain values of F_{GHZ} greater than 0.9 also fixing ω/g in different intervals, see figure 3.9.

We thus may conclude that the scheme to generate GHZ states discussed here, (3.9) is robust enough with respect to the presence of noise sources describable as independent ohmic bosonic baths [92].

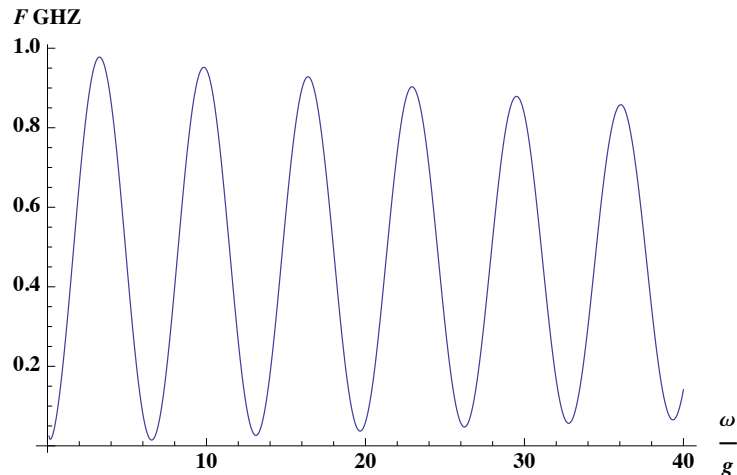


Figure 3.9: Fidelity F_{GHZ} as a function of ω/g when we assume that all the three baths are characterized by the same ohmic spectral density given in (3.39) with $\gamma_0/g = \alpha = 10^{-3}$ and the parameters assume the values $\tilde{g}/g = 0.1$. To evaluate F_{GHZ} we put $\varphi = \frac{3\pi}{2}(\sqrt{3} + \frac{(3+\sqrt{3})}{4} \frac{\omega}{g-\tilde{g}})$ for the GHZ state in equation (3.41).

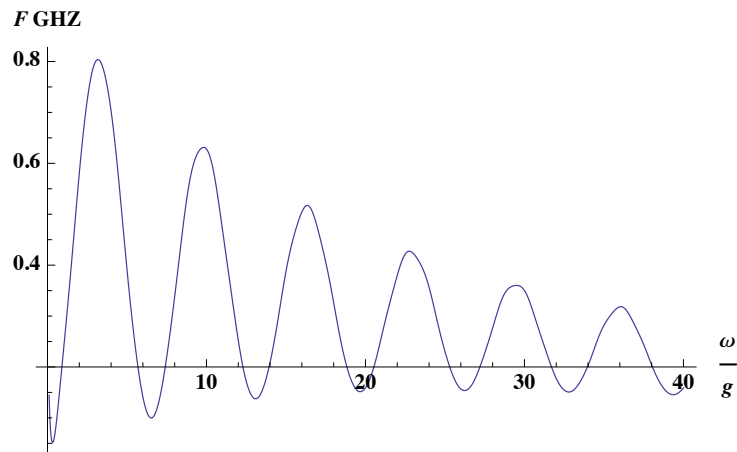


Figure 3.10: Fidelity F_{GHZ} as a function of ω/g when we assume that all the three baths are characterized by the same ohmic spectral density given in (3.39) with $\gamma_0/g = \alpha = 10^{-2}$ and the parameters assume the values $\tilde{g}/g = 0.1$. To evaluate F_{GHZ} we put $\varphi = \frac{3\pi}{2}(\sqrt{3} + \frac{(3+\sqrt{3})}{4} \frac{\omega}{g-\tilde{g}})$ for the GHZ state in equation (3.41).

3.2.3 Conclusive remarks

Summarizing, we have proposed a new generation scheme for a *GHZ* entangled quantum state in a tripartite system. To do this we use a symmetric control of all the qubits in the system and, in particular, we make use of a triangular coupling interaction scheme and of single qubit local rotations. We demonstrated the possibility of generating the desired state appropriately setting the interaction time between the qubits. Moreover, using the mathematical tools of a markovian master equation, which help us to determine the evolution of the system coupled to three independent bosonic baths, we found that this generation scheme is robust enough with respect to the presence of noise sources describable as independent ohmic bosonic baths.

Chapter 4

Thermal current in superconducting flux qubits

In chapter 1 we saw that the charge current through a superconducting weak link is sensitive to the phase difference of the superconducting order parameters on either side of the link. In the absence of a bias voltage, a dissipationless Josephson current flows through the link which is proportional to the sine of the phase difference. In section 1.2.1 we saw that also the heat current flowing through a Josephson junction depends on the phase difference of the two superconductors separated by the junction. This effect has been predicted over 50 years ago by Maki and Griffin [36], and only very recently has been measured experimentally [37–41]. Heat transport through weak links in superconductors was theoretically studied in [53, 108, 109]; see also [110] for a review on interference in heat transport and thermoelectric effects in superconducting weak links. It has been found that the heat current can be modulated by the applied phase gradient [111]. Recent experiments have shown that weak links in superconductors can be used to refrigerate small islands [112] and trap hot quasiparticles [113].

As it was introduced in chapter 2, an altogether different application of the phase sensitivity of the supercurrent in superconducting rings is the realization of flux qubits where the phase sensitivity of the device is used to implement qubit operations. In what follows, we will combine these two intriguing studies on the phase-sensitivity in superconducting rings. We are in particular interested in the dependence of the heat current on the state of the Delft qubit and of the Fluxonium qubit. Beyond this, we find that the state-sensitive heat current has an impact on the qubit state. With the help of a master equation approach, we investigate how the temperature *gradient* influences the dynamics of the qubit system.

4.1 Measurement and dephasing of a Delft qubit due to heat currents

The Delft design of the flux qubit consists in a superconducting loop interrupted by three Josephson junctions. It is furthermore characterized by the fact that the Josephson coupling of one of the junctions is smaller by a factor $\alpha \simeq 0.75$ with respect to the others [60] (fig. 4.1), which in actual implementations is made tuneable by replacing this third junction by a DC SQUID [23]. Another important tuning parameter is the external flux Φ threading the loop. If the flux is close to half a superconducting flux quantum, $\Phi = h/4e$, the superconducting system emulates a particle in a (shallow) double-well potential, where the state in either well corresponds to a circulating persistent current, either flowing clockwise or counterclockwise around the loop. These two states represent the qubit states of the device.

In what follows we investigate a superconducting ring with three Josephson junctions subject to a temperature gradient. We use the microscopic description of the Josephson junctions described in chapter 1 in order to investigate the phase-dependent heat current through them. We will show that indeed the heat current in a temperature-biased Delft qubit is sensitive to the qubit state, with typical sensitivities of 4%. We determine the rate of coherence suppression, which is shown to be given by the rate with which the difference in heat currents at the two qubit states accumulates an energy difference approximately equal to the gap energy. The difference in heat currents due to a thermal gradient depending on the qubit state is hence demonstrated to be a qubit-state measurement. Depending on the temperature gradient, the associated typical dephasing times range from nano- to microseconds with the condition that the qubit is detuned from the “sweet spot” of half a flux quantum, $\Phi = \Phi_0/2$, threading the superconducting loop, to a typical “operation point” of $\Phi = 0.495\Phi_0$. This adds an additional contribution to the dephasing, which in general is attributed to non-equilibrium quasiparticles [114–116].

4.1.1 Qubit-state sensitive heat currents

The system we will investigate in this paragraph is a Delft qubit. In particular, we want to investigate the sensitivity of the heat current to the state of the Delft qubit realised by the three-junction SQUID, which was introduced in paragraph 2.3.3. If between the electrodes of the qubit there is a thermal gradient we expect to have some thermal currents in the system. Since both the thermal currents and the states of the qubit are dependent on the phase values across the junctions as it has been pointed out in paragraphs 1.2.1 and 2.3.3, we want to investigate how the thermal current change according to the state of the qubit and, in the next section, how much they influence the qubit dynamics.

In order to understand the change in the thermal current depending on the qubit state, we propose to study the difference between the heat currents compared to the sum of the two currents for the qubit being in the state $|\psi_L\rangle$ or $|\psi_R\rangle$, characterising the sensitivity [32],

$$s_l = \frac{\dot{Q}_R^l - \dot{Q}_L^l}{\dot{Q}_R^l + \dot{Q}_L^l} \quad \text{with} \quad \dot{Q}_{L/R}^l = \langle \psi_{L/R} | \dot{Q}^l | \psi_{L/R} \rangle \quad (4.1)$$

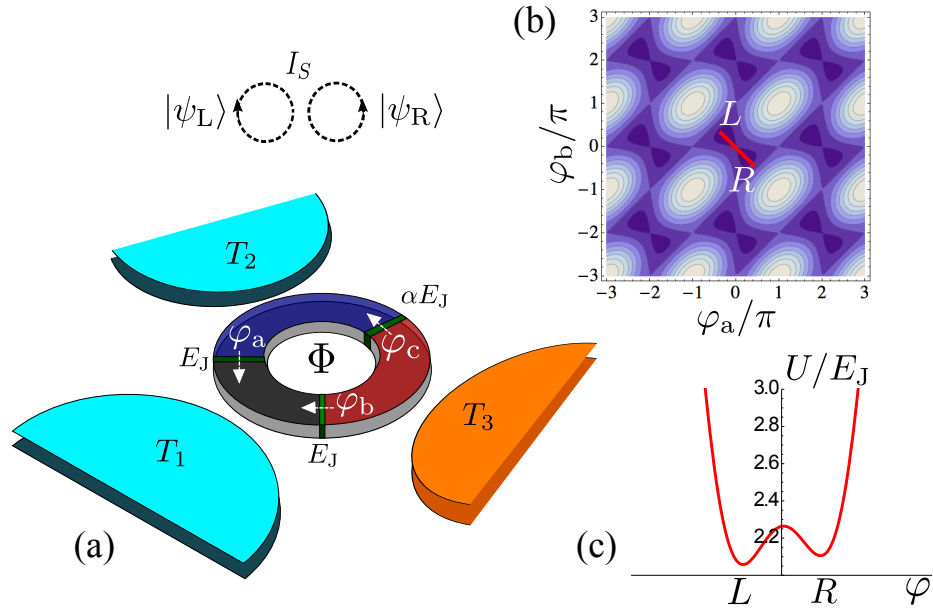


Figure 4.1: **(a)** Sketch of a persistent current qubit realised by a SQUID with three superconducting links, characterised in general by different phase differences, $\varphi_a, \varphi_b, \varphi_c$. The SQUID is penetrated by a magnetic flux Φ . The direction of the supercurrent circulating in the SQUID characterises the state of the persistent current qubit. The different sections of the SQUID are coupled to thermal baths with temperatures T_1, T_2 and T_3 . **(b)** Potential landscape of the SQUID as a function of the phase differences for $\alpha = 0.75$ and $\Phi/\Phi_0 = 0.495$. The potential is 2π -periodic in φ_a and φ_b and it can be divided into equal square cells of side 2π . **(c)** Cut through the potential in the central cell of figure (b) along the line $\varphi = \varphi_a = -\varphi_b$ visualising the two minima corresponding to the qubit states of oppositely circulating currents.

The expectation values are obtained from the usual integral over φ of the product of the heat currents given in (1.28) with the wave functions of (2.29). We evaluate the heat currents in each electrode due to a temperature gradient induced by $T_1 = T_2 < T_3$ sketched in figure 4.1. This yields heat currents in electrodes 1 and 2 given by the heat flow through the junction with electrode 3 only, while the heat current in electrode 3 has two contributions. To simplify the notation, we now take as a reference the heat current into electrode 1, with $\dot{Q}_{\text{int}} \equiv \dot{Q}_{\text{int}}^1(T_1, T_3)$ and $\dot{Q}_{\text{qp}} \equiv \dot{Q}_{\text{qp}}^1(T_1, T_3)$. Starting from equation (4.1) the sensitivities then take the simple form [32]

$$\begin{aligned}
 s_1 &= \frac{\dot{Q}_{\text{int}}(C_L - C_R)}{2\dot{Q}_{\text{qp}} - \dot{Q}_{\text{int}}(C_L + C_R)} \\
 s_2 &= \frac{\dot{Q}_{\text{int}}(D_L - D_R)}{2\dot{Q}_{\text{qp}} - \dot{Q}_{\text{int}}(D_L + D_R)} \\
 s_3 &= \frac{\dot{Q}_{\text{int}}(\alpha(D_L - D_R) + (C_L - C_R))}{2\dot{Q}_{\text{qp}}(1 + \alpha) - \dot{Q}_{\text{int}}(\alpha(D_L + D_R) + (C_L + C_R))} .
 \end{aligned} \tag{4.2}$$

where, for a short notation and assuming the two qubit states to be well localized, we here define

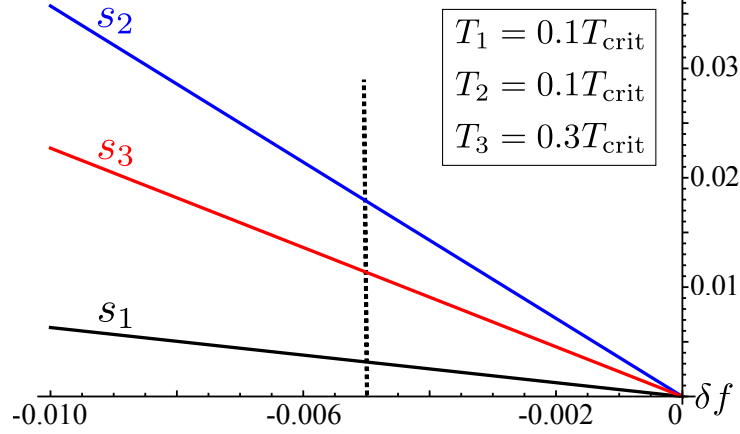


Figure 4.2: Plot of the sensitivities, s_l , for the three electrodes $l = 1, 2, 3$ as a function of the flux enclosed in the loop, for $\alpha = 0.75$ and $E_J/E_C \approx 80$ [32]. The vertical dotted line indicates the flux value of the Delft qubit “operation point” [60].

the phase-dependent factors

$$\begin{aligned} C_{L/R} &= \langle \psi_{L/R} | \cos(\varphi_a) | \psi_{L/R} \rangle = \cos(\varphi_{L/R}) e^{-1/(4\lambda_{L/R})}, \\ D_{L/R} &= \langle \psi_{L/R} | \cos(\varphi_c) | \psi_{L/R} \rangle = \cos(2\varphi_{L/R} + 2\pi f) e^{-1/\lambda_{L/R}}. \end{aligned} \quad (4.3)$$

We used the generalized Ambegaokar-Baratoff relations [117, 118] in order to relate the heat currents $\dot{Q}^{(i)}$ through the junctions $i = b, c$ to each other, when $T_1 = T_2$. The heat currents through the *different junctions* are furthermore related to the heat currents \dot{Q}^l *into the different reservoirs*, $l = 1, 2, 3$, by $\dot{Q}^{i=b} \equiv \dot{Q}^1$, $\dot{Q}^{i=c} \equiv \dot{Q}^2$ and hence $\dot{Q}^3 = -\dot{Q}^{i=b} - \dot{Q}^{i=c}$. By comparing the separate quasi-particle and interference components of these heat currents, see (1.29) and (1.30), we then find

$$\frac{\dot{Q}_{\text{int}}^c}{\dot{Q}_{\text{int}}^b} = \frac{\dot{Q}_{\text{qp}}^c}{\dot{Q}_{\text{qp}}^b} = \frac{I_{\text{crit}}^b}{I_{\text{crit}}^c} = \frac{R_c}{R_b} = \frac{R_{23}}{R_{13}} = \alpha. \quad (4.4)$$

This finally leads to the compact expressions in (4.2). The results for these three sensitivities as a function of the flux, in the vicinity of the sweet spot and the operation point of the Delft qubit, are shown in figure 4.2. The sensitivity of the heat currents to the qubit state hence yields a possible measure of the latter. The heat currents in electrodes 2 and 3 are most sensitive to the qubit state with a sensitivity of about 2% at the “operation point”, $f = 0.495$ [60]. The plot in figure 4.2 shows a dependence of the sensitivities as a function of the magnetic flux penetrating the SQUID which is very close to a linear function. The slopes of the latter depend on the specific realisation of the qubit, namely on the ratio α , of the electrode temperatures T_l and the applied thermal gradient, as well as on the ratio of Josephson and charging energy. This is shown in the approximate result for the heat currents for small deviations δf from the “sweet spot” $f = \frac{1}{2}$, $s_l \approx m_l(\alpha)\delta f$ with the respective slope m_l . The rather complex explicit analytic form of the slopes of the three sensitivities are given in appendix D and they are shown in figure 4.3 as a function of the ratio α , which is tuneable in the experiment. We find that the slopes of the

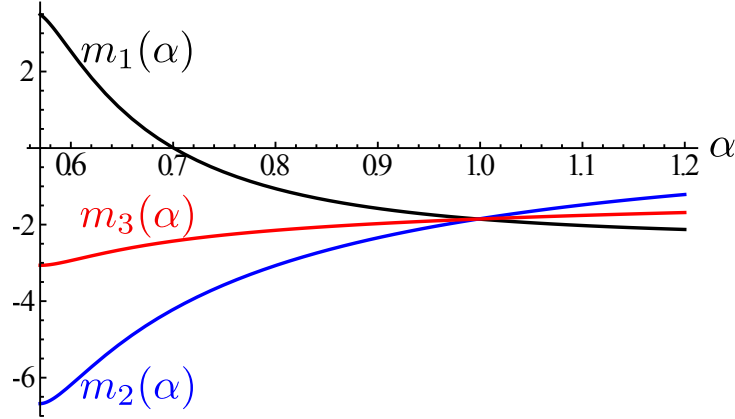


Figure 4.3: Coefficient of the linear expansion of the heat currents of the electrodes as a function of α for $T_1 = T_2 = 0.1T_{\text{crit}}$, $T_3 = 0.3T_{\text{crit}}$, and $E_J/E_C \approx 80$ [32].

sensitivities do in general not need to have the same sign. The slope with the largest absolute value is the one obtained from the heat currents into reservoir 2. This is related to the fact that the heat currents into this reservoir flow uniquely through the junction with the weakest Josephson coupling, namely junction c, which has consequently the largest phase difference and is most sensitive to the qubit state. While for the working point of the Delft qubit, that is at $\alpha \approx 0.75$, the slope of s_2 has already a rather large value, this value can be improved by lowering α . Note however that with α approaching 0.5 the two valleys of the potential get closer and the qubit states are not well defined any more. Equivalently for $\alpha > 1$ the SQUID can not be used as a qubit any longer.

4.1.2 Impact of temperature gradients on the qubit dephasing

After having demonstrated the sensitivity of the heat currents to the state of the qubit, the aim of this section is to study the impact of a temperature gradient - and the resulting heat current - on the coherence properties of the qubit. Our interest in this point is twofold: on one hand we want to find out the behavior of the qubit state under measurement, on the other hand we are interested in the impact of accidental temperature gradients on the dephasing of the qubit. We therefore consider the two-level system, defined by the states $|\psi_L\rangle$ and $|\psi_R\rangle$, namely the qubit states obtained from the low-energy physics of the SQUID, in contact with two heat baths, resulting in the model Hamiltonian [32]

$$\begin{aligned}
 H_{\text{toy}} = & -\frac{\varepsilon}{2}\tau^3 - \frac{w}{2}\tau^1 + \sum_{l=1,3} \sum_{k,\sigma} (\varepsilon_{l,k} - \mu_l) a_{l,k\sigma}^\dagger a_{l,k\sigma} \\
 & + \sum_{k,q,\sigma} \left[a_{1,k\sigma}^\dagger a_{3,q\sigma} (V_0\tau^0 + V_3\tau^3) + \text{H.c.} \right].
 \end{aligned} \tag{4.5}$$

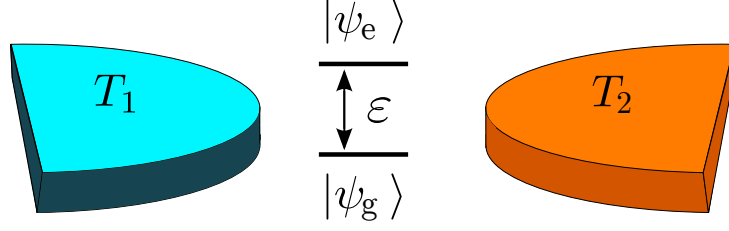


Figure 4.4: Model of the two-level system with level-spacing ϵ , tunnel-coupled to two quasi-particle baths at different temperatures T_1 and T_3 .

The model is depicted in figure 4.4. Here, the matrices $\tau^j, j = 0, 1, 3$ are Pauli matrices in the qubit space. The level splitting between the qubit states is given by ϵ and weak coupling between them is denoted by w . The creation (annihilation) operators of particles with momentum k and spin σ in lead l are given by $a_{l,k\sigma}^\dagger (a_{l,k\sigma})$.

In the simplified model of equation (4.5), we do not explicitly take into account the three superconducting leads with the heat currents, which depend on all three phase differences, but rather discuss a simplified microscopic model, which involves only two leads. The idea is to set the density of states and tunnelling matrix elements such as to reproduce the correct macroscopic thermal current between the reservoirs at temperature $T_1 = T_2$ and T_3 in the three lead setup. We expect that such a procedure, while being inaccurate for certain microscopic details, will correctly incorporate the effects of the phase-dependent thermal currents on the qubit. In linear response, the Hamiltonian (4.5) leads to a heat current,

$$\dot{Q}_{L/R}^{\text{toy}} = \frac{\pi}{\hbar} \int_{-\infty}^{\infty} d\omega \omega (|V_0|^2 \pm |V_3|^2) N_1(\omega) N_3(\omega) [f_1(\omega) - f_3(\omega)] \quad (4.6)$$

with $N_l(\omega)$ the density of states of the electrons in lead l (including spin). If we set the parameters

$$\begin{aligned} |V_0|^2 &= \frac{1}{2} |V^{13}|^2 [2\alpha + 2 - C_R - C_L - \alpha (D_R + D_L)] \\ |V_3|^2 &= \frac{1}{2} |V^{13}|^2 [C_R - C_L + \alpha (D_R - D_L)] \\ N_l(\omega) &= N_l^0 \frac{|\Delta_l|}{\sqrt{\omega^2 - |\Delta_l|^2}} \theta(\omega^2 - |\Delta_l|^2), \end{aligned} \quad (4.7)$$

with $\theta(x)$ the unit-step function, we achieve the goal of reproducing the correct qubit-state dependent heat current with $\dot{Q}^{\text{toy}} = \dot{Q}^3 = -\dot{Q}^1 - \dot{Q}^2$; here and below, we assume the magnitude of the quasiparticle and interference parts of the heat current to be equal.

We are now interested in the dynamics of the qubit state depending on the qubit-state sensitive heat current induced by the temperature gradient. Starting from the full system's density matrix, we therefore trace out the lead degrees of freedom and write down a master equation for the reduced density matrix of the qubit, $\rho(t)$. If we write the density matrix of the qubit as $\rho(t) = \frac{1}{2} [\mathbb{1} + \boldsymbol{\tau} \cdot \mathbf{S}(t)]$ with $\mathbf{S}(t) = \text{Tr}[\rho(t)\boldsymbol{\tau}] = (\rho_{LR}(t) + \rho_{RL}(t), i(\rho_{LR}(t) -$

$\rho_{\text{RL}}(t), \rho_{\text{LL}}(t) - \rho_{\text{RR}}(t))^{\text{T}}$, we obtain the Pauli rate equation

$$\dot{\mathbf{S}}(t) = \mathbf{S}(t) \times \mathbf{h} - \gamma(S_1(t), S_2(t), 0)^{\text{T}}. \quad (4.8)$$

This equation contains a precession around a pseudo-magnetic field, $\mathbf{h} = (w, 0, \varepsilon)^{\text{T}}$, determined by the qubit properties, and a relaxation of the coherences of the reduced density matrix with the rate γ , while the diagonal elements, namely the occupations of the qubit states, do not decay. This is also appreciable from the solution of the master equation, which for large detuning $\varepsilon \gg w$ with respect to the weak tunneling between the qubit states, is given by

$$\begin{aligned} \rho_{\text{LL}}(t) &\approx \rho_{\text{LL}}(0), & \rho_{\text{RR}}(t) &\approx \rho_{\text{RR}}(0), \\ \rho_{\text{LR}}(t) &\approx \rho_{\text{LR}}(0)e^{-(\gamma+i\varepsilon)t}, & \rho_{\text{RL}}(t) &\approx \rho_{\text{RL}}(0)e^{-(\gamma-i\varepsilon)t}. \end{aligned} \quad (4.9)$$

The value of the dephasing rate γ reads [32],

$$\gamma = \frac{4\pi|V_3|^2 N_1^0 N_3^0}{\hbar} \int_{|\Delta_{\text{max}}|}^{\infty} d\omega \omega^2 \frac{[1-f_1(\omega)]f_3(\omega) + [1-f_3(\omega)]f_1(\omega)}{\sqrt{\omega^2 - |\Delta_1|^2} \sqrt{\omega^2 - |\Delta_3|^2}}. \quad (4.10)$$

Importantly, this rate equals zero, if the sensitivity of the heat current to the qubit state vanishes and hence $|V_3|^2 \propto C_{\text{R}} - C_{\text{L}} + \alpha(D_{\text{R}} - D_{\text{L}}) = 0$. Note that this means that the temperature gradient leads to dephasing only when the qubit is tuned away from the sweet spot. Indeed, it is possible to conclude that the qubit-state sensitivity of the heat current represents a measurement process which reflects in the time-dependent solution of the master equation given in (4.9).

The dephasing rate is connected to fluctuations in the electronic subsystem which drive the qubit. In equilibrium, we would expect a fluctuation-dissipation relation to hold which relates the fluctuations to the response coefficient of the system. Naturally, this is not true in the non-equilibrium situation studied here. It is however interesting to compare the response of the system to the temperature gradient, namely the heat current depending on the qubit states, to the related dephasing rate. We therefore introduce the dimensionless ratio $r = |\Delta_{\text{max}}|\gamma/|\dot{Q}_{\text{L}}^3 - \dot{Q}_{\text{R}}^3|$. As above, we specialise to the case when $T_1, T_3 \lesssim |\Delta_{\text{max}}|/k_{\text{B}}$. With a similar calculation as the one following 1.30, we obtain the estimate

$$r \simeq \coth\left(\frac{|\Delta_{\text{max}}||T_1 - T_3|}{2k_{\text{B}}T_1T_3}\right). \quad (4.11)$$

This means that r is universal with respect to microscopic details like the normal-state resistance R_{13} or the phase difference φ_j across the junctions, and only depends on thermodynamical quantities like the temperatures T_1, T_3 and the gap Δ_0 . We see that for small temperature differences, $\delta T = T_1 - T_3 \ll T_1, T_3$, this ratio becomes $r \simeq k_{\text{B}}T^2/(|\Delta_{\text{max}}|\delta T)$.

The dephasing time $\mathcal{T}_{\phi} = \gamma^{-1}$ is in this case given by [32]

$$\begin{aligned} \mathcal{T}_{\phi} &\simeq \frac{\Delta_0^2(1 - T/T_{\text{crit}})\delta T}{k_{\text{B}}T^2|\dot{Q}_{\text{L}}^3 - \dot{Q}_{\text{R}}^3|} \\ &\simeq \frac{e^2 R_{13} e^{\Delta_{\text{max}}/k_{\text{B}}T}}{\Delta_{\text{max}} \ln(T_{\text{crit}}/T_{\text{cut}})[C_{\text{L}} - C_{\text{R}} + \alpha(D_{\text{L}} - D_{\text{R}})]}. \end{aligned} \quad (4.12)$$

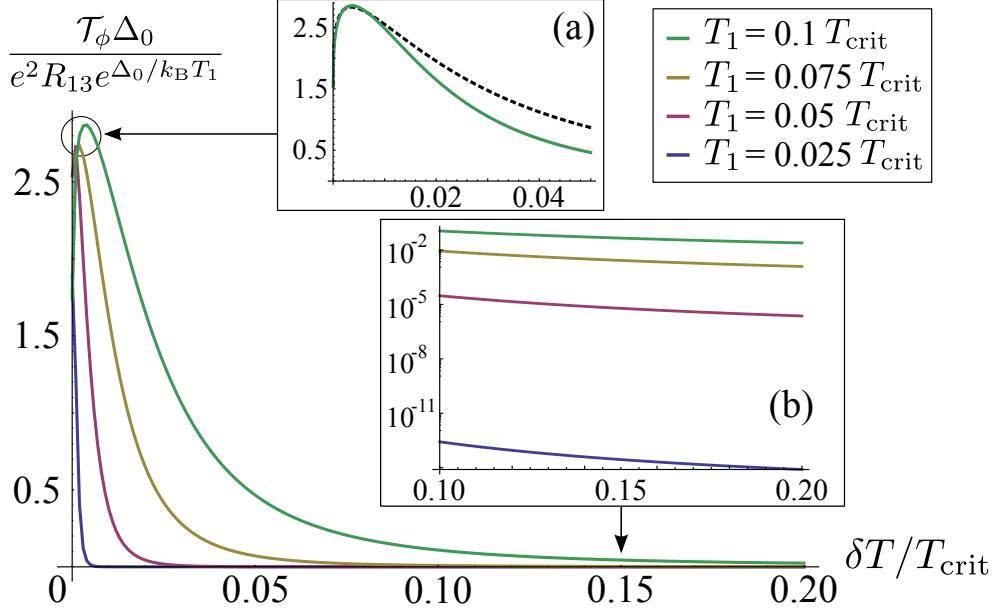


Figure 4.5: Dephasing time as a function of the temperature gradient δT for different values of T_1 with $T_1 \leq T_3$ [32]. The dephasing time was calculated for $\alpha = 0.75$ and $f = 0.495$. In the inset (a) we show an enlargement at $\delta T \ll T$, for the case of $T_1 = 0.1 T_{\text{crit}}$ (full, green line) together with the approximate function of the dephasing time given in 4.12 (dashed, black line) multiplied by a numerical factor of order 1. In the inset (b) we show the enlargement of the plot for $0.1 < \delta T / T_{\text{crit}} < 0.2$ on a logarithmic scale. Note that this plot is valid only for temperature differences larger than the cutoff temperature, $\delta T > T_{\text{cut}}$, which in turn depends on the microscopic details of the Josephson junctions.

The dephasing times in units of $e^2 R_{13} e^{\Delta_{\text{max}} / k_B T_1} / \Delta_0$ are shown in figure 4.5 as a function of the temperature difference δT for different values of the minimum temperature T_1 . The inset (a) of figure 4.5 compares the full result (full green line) with the approximation of equation (4.12).

In the opposite regime of large temperature bias, we have that $r \simeq 1$ and thus the dephasing rate is approximately equal to $\gamma \simeq |\dot{Q}_L^3 - \dot{Q}_R^3| / |\Delta_{\text{max}}|$. In particular, we find in this regime that the dephasing time \mathcal{T}_ϕ of the qubit is given by [32]

$$\mathcal{T}_\phi \simeq \frac{\Delta_0}{|\dot{Q}_L^3 - \dot{Q}_R^3|} \simeq \frac{e^2 R_{13} e^{\Delta_0 / k_B T_{\text{max}}}}{\Delta_0 [C_L - C_R + \alpha(D_L - D_R)]}, \quad (4.13)$$

i.e. the time after which the difference of the energy transported by the heat currents in the two qubit states equals the gap Δ_0 of the superconductor. This is well confirmed by the inset (b) of figure 4.5, which shows the dramatic decrease of the dephasing time with increasing temperature gradient.

Using the values we applied to estimate the heat currents in this system, we can also estimate the dephasing time. Taking $\Delta_0 / e^2 R_{13} \simeq 1 \text{ THz}$ as in [38], we have that $\mathcal{T}_\phi \approx 1 \text{ ns}$ for large temperature gradients, $\delta T / T_{\text{min}} \gg 1$. For small temperature gradients, it can be shown that a temperature T_{min} of less than $0.1 T_{\text{crit}}$ has to be reached in order to avoid a strong

limitation of the dephasing due to the thermal current. Indeed, for $\delta T/T_{\min} \ll 1$, $T_{\min} \simeq T_{\max} \lesssim 0.1T_{\text{crit}}$, and taking the logarithm to be of order one, we have $\mathcal{T}_\phi \approx 1\mu\text{s}$. The actual dephasing times of the Delft qubit range from a few tens of nanoseconds [119] up to a microsecond [75] (as it is possible to see also from table 2.2) and thus are of the same order of magnitude. As the nominal temperatures reached for today’s superconducting persistent current qubits is usually smaller than $0.1T_{\text{crit}}$ [120, 121], it is unlikely that the thermal currents do constitute the *dominant* source of dephasing for those qubits. However, it is well known that quasiparticles in small superconducting structures badly thermalise, leading to problems in reaching the base temperature in the dilution refrigerator [113, 122] and thus effects of the phase dependence of the thermal current on the coherence properties of the Delft qubit cannot be excluded.

Looking at figure 4.5 one can notice that for small values of the temperature gradient the dephasing time presents a maximum for a specific value of δT . In other words, there seems to be an *optimum* value of the temperature gradient, different from zero, for which the dephasing time would be bigger with respect to its neighboring values. We use the conditional because this aspect can be an interesting starting point for a more accurate investigation on the problem. In fact, the investigation done in this section is valid for the tunneling approximation, which, as was mentioned in section 1.2.1, in the case of small temperature gradient has an expression for the thermal current that needs a cutoff temperature $T_{\text{cut}} = \delta T$. However, the tunneling approximation does not take properly into account a resonance in the density of states due to a weakly bound Andreev state. In the linear response derivation of the thermal currents for $\delta T \ll T_c$ this resonance introduces a new cutoff $T_{\text{cut}} = D\Delta_0 \sin^2(\varphi_{lm}/2)/k_B$, and in our case it is important to understand if, depending on the value of the transparency D characterizing the junction, our derivation is consistent with the properties of the system under study.

4.1.3 Conclusive remarks

In this section we have shown that due to the phase sensitivity of the heat current which flows in weak links of a superconducting loop, the heat current due to a temperature gradient applied to a flux qubit depends on the state of the qubit which is formed when the loop is threaded with a magnetic flux that is close to half a superconducting flux quantum. We have found that the sensitivity of the heat current to the qubit state can be up to 4%, when the qubit is tuned away from the “sweet spot” of exactly half a flux quantum threading the loop. This should allow to identify the state of the flux qubit in experiments of the type performed in [37, 38].

Moreover, we have found that due to this difference of heat currents for different qubit states, a thermal gradient leads to a dephasing of the qubit. In particular, we have found that the ratio of the dephasing rate to the difference of the heat currents is universal with respect to microscopic details and only depends on the temperature of the reservoirs measured in units of the superconducting gap at zero temperature. For example, in the case of large temperature gradients the dephasing time of the qubit corresponds to the time when the difference of heat currents have transported an energy of the order of the superconducting gap. We have shown that the dephasing time of the flux qubit in the Delft design due to the phase-sensitive heat current can range from microseconds for small temperature differences to nanoseconds for large

temperature differences thus constituting a potential source of dephasing given the fact that the qubits are driven by microwave pulses which may lead to an imbalance of heating between the different sections of the superconducting loop.

4.2 Dephasing of the fluxonium qubit due to thermal currents

In the previous section it has been shown that the dephasing time is closely linked to the fact that the heat current due to quasiparticles flows through Josephson junctions. In this section, we will concentrate our study on the thermal currents in a fluxonium qubit, which is a more performant flux qubit system with respect to the Delft design. We will show that even though the fluxonium qubit is insensitive to *charge* noise due to quasiparticles it still remains sensitive to quasiparticles tunneling through the Josephson junction due to the *thermal* transport that is connected with the transport of the quasiparticles. We do this by analyzing the thermal currents in a fluxonium system due to small temperature gradients ($\delta T \ll T_c$) in the linear response regime derivation, studying in particular their dependence on the parameters characterizing the system as well as their sensitivity to the quantum state of the fluxonium qubit. The reason for this choice is that it is very interesting to study the properties of parasitic thermal currents originated from small temperature gradient in the loop, which can have detrimental effects on the coherence of the qubit system. In fact, we show that thermal current can be at the origin of not negligible dephasing effects of the qubit. We want to stress that even though we assume that the reservoirs are in thermal equilibrium our results indicate that a nonequilibrium population of quasiparticles (which can be roughly modeled by an effective temperature which is larger than the nominal one) that typically are present in superconducting qubit experiments, leads to dephasing of the fluxonium qubit.

In what follows we wish to investigate the sensitivity of the heat current to the state of the fluxonium qubit, supposing in particular that there is a thermal gradient $\delta T = T_1 - T_2$ through the black sheep, see figure 4.6. As mentioned before, being interested to small values of δT , that is $\delta T/T_c \sim 10^{-2} \dots 10^{-1}$, we will evaluate the heat current in the linear response regime.

4.2.1 Thermal current in a fluxonium qubit

We would like to investigate how the phase sensitivity of the thermal current through a Josephson junction manifests itself in the fluxonium. We are interested in a situation where there is a temperature gradient applied at the two reservoirs surrounding the black sheep, see figure 4.6. As the M Josephson junctions of the array are equivalent, the temperature difference δT_L across each of them is also the same. As the temperature difference of the M junctions will add up to the total temperature difference δT , we have that the temperature difference across each of the array junctions is $\delta T/M$. Thus in the limit of many junctions the temperature gradient across each of them becomes very small, $\delta T_L \ll \delta T \ll T$.

The task is to evaluate the thermal current \dot{Q} flowing in the cold reservoir which is held at

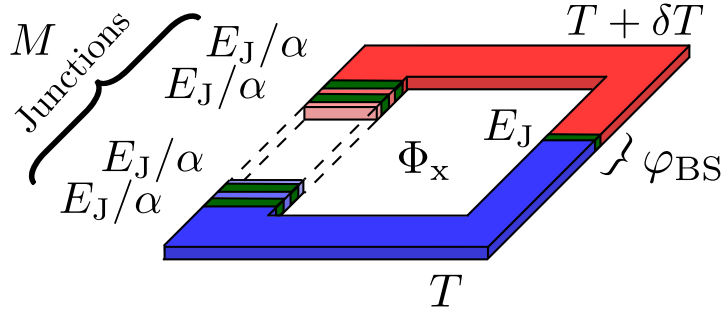


Figure 4.6: The fluxonium qubit consists of a superconducting loop interrupted by $M + 1$ Josephson junctions which is threaded by a magnetic flux Φ_x . In an effective description only the junction with the Josephson energy E_J and the phase difference φ_{BS} acts as a Josephson junction whereas the remaining M junctions with a larger Josephson energy E_J/α ($\alpha < 1$) act as a superinductance. In this paragraph we will suppose that there is a thermal gradient δT between the two electrodes separated by the black sheep.

temperature T (or equivalently the thermal current flowing out of the hot reservoir at temperature $T + \delta T$). The thermal current is given by the sum of two terms

$$\dot{Q} = \dot{Q}(\varphi_{BS}, T, \delta T) + \dot{Q}(\varphi_M, T_M, \delta T/M), \quad (4.14)$$

where the first term is the contribution of the black sheep and the second term is due to the last JJ of the array.

In the following, we are interested in the effect this heat current has on the coherence properties of the fluxonium qubit. To this aim, analogously to the previous section, we will study the difference between the heat current when the qubit is in the state $|\psi_g\rangle$ and that when the qubit is in the state $|\psi_e\rangle$. This is again best characterized by the sensitivity

$$s_{\text{fl}} = \frac{\dot{Q}_e - \dot{Q}_g}{\dot{Q}_e + \dot{Q}_g} \quad \text{with} \quad \dot{Q}_{g/e} = \langle \psi_{g/e} | \dot{Q} | \psi_{g/e} \rangle. \quad (4.15)$$

A large sensitivity corresponds to a large difference of thermal currents and as we will see later to a fast dephasing of the qubit. We are interested on the dependence of the sensitivity on the qubit parameter. As a first step, we will show that the sensitivity only depends on the effective parameters E_L , E_C , and E_J and not on the number of junctions M with which the superinductance is emulated.

4.2.2 Independence of the sensitivity on the number of array junctions

Before proceeding in the evaluation of the sensitivity s_{fl} , we want to convince ourselves that the sensitivity only depends on the effective parameters E_L , E_C , and E_J of the qubit and not on the specific number of junctions M (or the asymmetry factor α) with which the superinductance L_{eff} is emulated. In order to realise a fluxonium qubit modelled by the Hamiltonian given in equation (2.28), a large amount M of array junctions is needed, which all have a Josephson

energy larger than the one of the *black sheep* by a factor $1/\alpha$. To obtain a given value of E_L , the number of array junctions and their coupling strength hence need to scale like $\alpha \propto M^{-1}$. As the generalized Ambegaokar-Baratoff model [40, 123] relate the Josephson energy to the normal state resistance, we find that the ratio of the normal state resistance of a junction in the array to the one of the black sheep should be given by $R_L/R_{BS} = \alpha$. Using this relation, all coefficients κ_i can be expressed in terms of the parameters of the *black sheep*, only.

The eventual dependence of the sensitivity on M could arise only from the contribution to the thermal current due to the last junction, $\dot{Q}(\varphi_M, T_M, \delta T/M)$, in correspondence of which $T_M = T - \delta T/2M$ and $\varphi_M = -(\varphi_{BS} - 2\pi f)/M$. But for M large enough, $\varphi_M \rightarrow 0$ and, exploiting equation (1.35), we may state that $\kappa_0(T_M \simeq T)$ is the only relevant term for $\dot{Q}(\varphi_M \approx 0, T_M, \delta T/M)$. As a consequence, except for the term $\kappa_0(T_M \simeq T)$, the thermal current \dot{Q} will depend only on the thermal current through the *black sheep* which is M independent.

It is interesting at this point to investigate which are the physical parameters that contribute to determine such a behavior. In order to do this, instead of using the sensitivity as numerically calculated starting from equation (4.15), we consider the value of s_{fl} obtained for the black sheep phase points correspondent to the minima of the potential relative to the excited and ground state. From the equation of the potential (2.26) we calculate the minima φ_e and φ_g with respect to φ , correspondent to the excited and ground state respectively. From equation (2.25) we find that the phase difference across the black sheep is given by $\varphi_{BS} = -\varphi + 2\pi f$, so we define the value of the phase φ_{BS} in correspondence of the the excited and ground state as

$$\varphi_{BS}^{e/g} = -\varphi_{e/g} + 2\pi f. \quad (4.16)$$

Exploiting the values of $\varphi_{BS}^{e/g}$, the sensitivity s_{fl} is given by

$$s_{\text{fl}} = \frac{\kappa_2 F_-(\varphi_{BS}^e, \varphi_{BS}^g) - \kappa_1 G_-(\varphi_{BS}^e, \varphi_{BS}^g)}{\kappa_2 F_+(\varphi_{BS}^e, \varphi_{BS}^g) - \kappa_1 G_+(\varphi_{BS}^e, \varphi_{BS}^g) + 2(1 + \frac{E_L}{E_J})\kappa_0} \quad (4.17)$$

where

$$\begin{aligned} F_{\pm} &= \sin^2 \frac{\varphi_{BS}^e}{2} \pm \sin^2 \frac{\varphi_{BS}^g}{2}, \\ G_{\pm} &= \sin^2 \frac{\varphi_{BS}^e}{2} \ln \left(\sin^2 \frac{\varphi_{BS}^e}{2} \right) \pm \sin^2 \frac{\varphi_{BS}^g}{2} \ln \left(\sin^2 \frac{\varphi_{BS}^g}{2} \right). \end{aligned} \quad (4.18)$$

As mentioned before, the contribution from the junction of the array enters only via κ_0 . Furthermore, since the values φ_{BS}^e and φ_{BS}^g depend only on the values of the energies E_J , E_C and E_L , we see from equation (4.17) that, when keeping the ratios of these energies fixed, the sensitivity is independent of the number M of junctions in the array.

4.2.3 Sensitivity near $f = 0.5$

In the following we want to show the importance of the superinductance for the heat current sensitivity. We therefore confine our attention on values of f for the case where the ground and

first excited state are almost degenerate, namely $0 < \delta f \ll 1$. Starting from equation (2.28) it is easy to convince oneself that for $f = 0.5$ the potential is symmetric with respect to $\varphi = 0$. In this case let's indicate by $\pm\varphi^*$ the position of the two minima φ_e and φ_g . The value of φ^* cannot be found analytically and when necessary we will evaluate it by a numerical calculation. Slightly varying f we expect that the two minima are shifted in such a way that $\varphi_{e/g} = \pm\varphi^* + \delta\varphi$ where $\delta\varphi$, at first order in δf , is given by

$$\delta\varphi = \frac{E_J \cos \varphi^*}{E_J \cos \varphi^* - E_L} 2\pi \delta f \quad (4.19)$$

To calculate the sensitivity in equation (4.17) we must calculate $F_{\pm}(\varphi_{\text{BS}}^e, \varphi_{\text{BS}}^g)$ and $G_{\pm}(\varphi_{\text{BS}}^e, \varphi_{\text{BS}}^g)$ using the relation given in equation (4.16). At first order in δf , we can write

$$\begin{aligned} F_+(\varphi_{\text{BS}}^e, \varphi_{\text{BS}}^g) &\approx 2 \cos^2 \frac{\varphi^*}{2}, \\ F_-(\varphi_{\text{BS}}^e, \varphi_{\text{BS}}^g) &\approx -\tan \varphi^* \frac{E_L}{E_J} \delta\varphi, \\ G_+(\varphi_{\text{BS}}^e, \varphi_{\text{BS}}^g) &\approx 2 \cos^2 \frac{\varphi^*}{2} \ln \left(\cos^2 \frac{\varphi^*}{2} \right) \\ G_-(\varphi_{\text{BS}}^e, \varphi_{\text{BS}}^g) &\approx -\left[1 + \ln \left(\cos^2 \frac{\varphi^*}{2} \right) \right] \tan \varphi^* \frac{E_L}{E_J} \delta\varphi \end{aligned} \quad (4.20)$$

Inserting equation (4.20) into equation (4.17), we finally have

$$\begin{aligned} s_{\text{fl}} &\approx \frac{\left[\kappa_1 \left[1 + \ln \left(\cos^2 \frac{\varphi^*}{2} \right) \right] - \kappa_2 \right] \frac{\tan \varphi^* E_L}{E_J} \delta\varphi}{\kappa_2 \cos^2 \frac{\varphi^*}{2} - \kappa_1 \left[\cos^2 \frac{\varphi^*}{2} \ln \left(\cos^2 \frac{\varphi^*}{2} \right) \right] + \left(1 + \frac{E_L}{E_J} \right) \kappa_0} \\ &\approx \frac{\left[\kappa_1 \left[1 + \ln \left(\cos^2 \frac{\varphi^*}{2} \right) \right] - \kappa_2 \right] \left(\frac{E_L \sin \varphi^*}{E_J \cos \varphi^* - E_L} \right) \pi \delta f}{\kappa_2 \cos^2 \frac{\varphi^*}{2} - \kappa_1 \left[\cos^2 \frac{\varphi^*}{2} \ln \left(\cos^2 \frac{\varphi^*}{2} \right) \right] + \left(1 + \frac{E_L}{E_J} \right) \kappa_0} \end{aligned} \quad (4.21)$$

Figure 4.7 shows the sensitivity s_{fl} against T as given by equation (4.17) (in blue) and its approximation as given in equation (4.21) (in red) in the case for $\delta f = 0.1$. Equation (4.21) gives an analytical expression of s_{fl} starting from which we can easily deduce the physical variables that concur in determining how fast s_{fl} decreases increasing the parameter f . It is interesting in particular to analyze the case $E_L \ll E_J$ in correspondence of which the two states, the ground and the excited states respectively, become more stable. To this scope let us initially observe that, putting $E_L = 0$ and $f = \frac{1}{2}$ we have $\varphi^* = \pi$. If now we consider the case for $E_L \ll E_J$, we expect that the value of the minimum of the two wells will be slightly different from π so that we can write $\varphi^* = \pi + \delta\varphi^*$ where at first order in E_L/E_J we have

$$\delta\varphi^* = -\frac{E_L}{E_J} \pi. \quad (4.22)$$

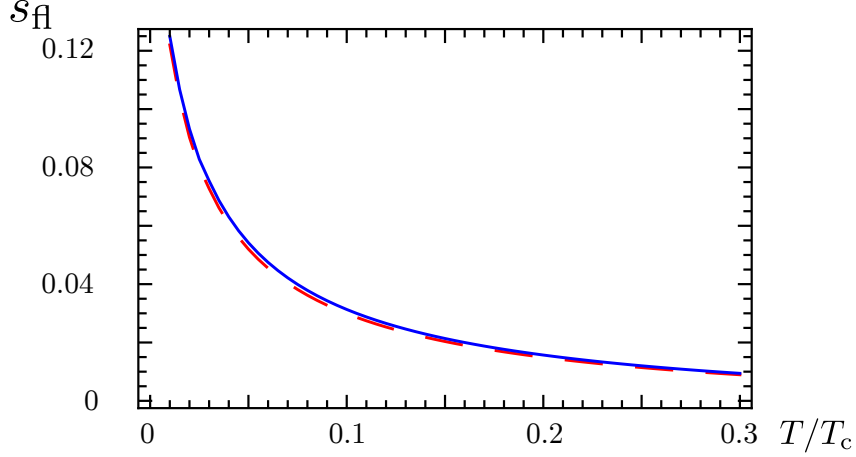


Figure 4.7: Comparison between the sensitivity defined in equation (4.17) (blue) and its approximation for $\delta f \rightarrow 0$ of equation(4.21) (red) in the case for $\delta f = 0.1$, $D = 10^{-2}$, $E_L/E_J = 5.8 \cdot 10^{-2}$, $E_C/E_J = 2.8 \cdot 10^{-1}$ as the ones used in Ref. [63].

Inserting equation (4.22) into equation (4.21) we finally obtain

$$s_{\text{fl}} \approx -\frac{\kappa_1}{\kappa_0} \left(\pi \frac{E_L}{E_J} \right)^2 \ln \left(\frac{\pi E_L}{2 E_J} \right)^2 \delta f \quad (4.23)$$

This result shows that the variation of the energy related to the superinductance, E_L , allows to change the sensitivity of the heat currents to the qubit state. In particular, in order to decrease the sensitivity, a suppression of the inductive energy E_L is required. The approximation of the sensitivity as a function of the energy is indeed very reasonable for small E_L , as can be seen from figure 4.8. It shows the comparison between the sensitivity defined in equation (4.17) (blue) and its approximation for $\delta f \rightarrow 0$ and $E_L/E_J \rightarrow 0$ obtained from equation (4.23) (red).

4.2.4 Dephasing time

Generally speaking there are many possible sources of dephasing for superconducting qubits arising, for example, from fluctuations of the offset charge, of the critical current, of the flux and so on. In other words any microscopic and/or macroscopic process that causes a drift or a fluctuation of the qubit frequency, becomes a sources of dephasing. In the work discussed in the previous part of this chapter [32] it has been demonstrated that when a Delft-qubit design is considered, even small accidental temperature gradients can lead to dephasing times of the order of microseconds. It appears thus reasonable to wonder if also in correspondence of a fluxonium qubit the presence of thermal gradients can be at the origin of a dephasing and if such a dephasing is negligible or not with respect to others. In order to investigate on the impact of possible thermal gradients on the fluxonium qubit dephasing let's start by writing an Hamiltonian describing a two level system defined by the states $|\psi_g\rangle$ and $|\psi_e\rangle$, correspondent to the two low-energy levels of the fluxonium, in contact with two heat baths. The Hamiltonian

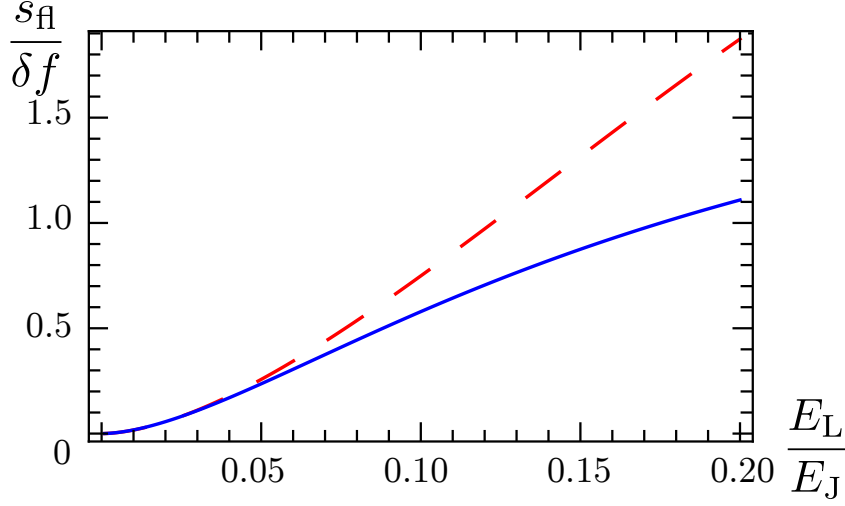


Figure 4.8: Comparison between the sensitivity defined in equation (4.17) (blue) and its approximation for $\delta f, E_L/E_J \rightarrow 0$ of equation (4.23) (red) in the case for $D = 10^{-2}$ and $T = 0.1T_c$.

model is the following

$$H_{\text{toy}} = H_S + H_I \quad (4.24)$$

with

$$H_S = -\frac{\varepsilon}{2}\tau^3 - \frac{w}{2}\tau^1 + \sum_{l=1,2} \sum_{k,\sigma} (\varepsilon_{l,k} - \mu_l) c_{l,k\sigma}^\dagger c_{l,k\sigma}, \quad (4.25)$$

$$H_I = \sum_{k,q,\sigma} (V_0\tau^0 + V_3\tau^3) (c_{1,k\sigma}^\dagger c_{2,q\sigma} + \text{H.c.}).$$

where $V_{0/3} = (V_e \pm V_g)/2$, ε represents the level splitting between the qubit states while w is a weak coupling between them.

Starting from Hamiltonian model (4.25) we will set the density of states and tunneling matrix elements in such a way to reproduce the correct macroscopic thermal current between the reservoirs at temperatures T_1 and T_2 in the two leads setup so that we will incorporate the effects of the phase-dependent thermal currents on the qubit. The heat current obtained exploiting the Hamiltonian (4.25) is the following

$$\dot{Q}_{e/g}^{\text{toy}} = \frac{\pi}{\hbar} \int_{\Delta}^{\infty} d\omega \omega V_{e/g}^2 N_1^{e/g} N_2^{e/g} [f_1(\omega) - f_2(\omega)] \quad (4.26)$$

with the Fermion functions $f_i = [\exp(\omega/k_B T_i) + 1]^{-1}$ and where we used the local density of

states as given in Ref. [53]

$$\begin{aligned}
N_l^{e/g}(\omega) &= N_l^0 \langle \psi_{g/e} | \frac{|\omega|(\omega^2 - \Delta^2)^{1/2}}{\omega^2 - \omega_b^2} | \psi_{g/e} \rangle \\
&\approx N_l^0 \frac{|\omega|(\omega^2 - \Delta^2)^{1/2}}{\omega^2 - \Delta^2(1 - D/2)} \left(1 + \frac{D\Delta^2 e^{-\frac{1}{4\lambda_{e/g}}} \cos \varphi_{\text{BS}}^{e/g}}{2\omega^2 - 2\Delta^2(1 - D/2)} \right).
\end{aligned} \tag{4.27}$$

To obtain equation (4.26) we made the approximation

$$\langle \psi_{e/g} | V^2 N_1 N_2 | \psi_{e/g} \rangle = \langle \psi_{e/g} | V^2 | \psi_{e/g} \rangle N_1^{e/g} N_2^{e/g}$$

which is justified as the exchange terms are small with respect to the direct terms, i.e.,

$$\frac{\langle \psi_e | V^2 | \psi_g \rangle}{\langle \psi_{e/g} | V^2 | \psi_{e/g} \rangle}, \frac{\langle \psi_e | N_l | \psi_g \rangle}{\langle \psi_{e/g} | N_l | \psi_{e/g} \rangle} \ll 1. \tag{4.28}$$

Using this form for the density of states, in the tunneling regime, namely for small values of D , we have the following expression for the tunneling matrix elements

$$V_{e/g}^2(\omega) = 2V_{12}^2 \left(1 - \frac{\Delta^2}{\omega^2} e^{-\frac{1}{4\lambda_{e/g}}} \cos \varphi_{\text{BS}}^{e/g} \right) \tag{4.29}$$

with V_{12} being the tunnelling amplitude of the black sheep, linked to the normal state resistance by $R = \hbar(\pi e^2 N_1^0 N_2^0 |V_{12}|^2)^{-1}$, and $\lambda_{e/g}$ given in equation (2.30). We are now in condition to study the dynamics of the qubit state and its dependence on the temperature gradient. Starting from the full system's density matrix, we therefore trace out the lead degrees of freedom and write down a master equation for the reduced density matrix of the qubit, $\rho(t)$. If we write the interaction Hamiltonian H_I as

$$H_I = P_e B_e + P_g B_g \tag{4.30}$$

with

$$\begin{aligned}
P_e &= |\psi_e\rangle\langle\psi_e|, & B_e &= V_e \sum_{k,q,\sigma} (c_{1,k\sigma}^\dagger c_{2,q\sigma} + \text{H.c.}), \\
P_g &= |\psi_g\rangle\langle\psi_g|, & B_g &= V_g \sum_{k,q,\sigma} (c_{1,k\sigma}^\dagger c_{2,q\sigma} + \text{H.c.}).
\end{aligned} \tag{4.31}$$

we can write the master equation for the system as follows [107]

$$\dot{\rho}(t) = -i[H_S, \rho(t)] + \sum_{\alpha,\beta=e,g} \gamma_{\alpha\beta} \left(P_\beta \rho(t) P_\alpha - \frac{1}{2} \{P_\alpha P_\beta, \rho(t)\} \right)$$

where

$$\gamma_{\alpha\beta} = \frac{1}{2} \int \langle \{B_\alpha(t), B_\beta(0)\} \rangle dt \tag{4.32}$$

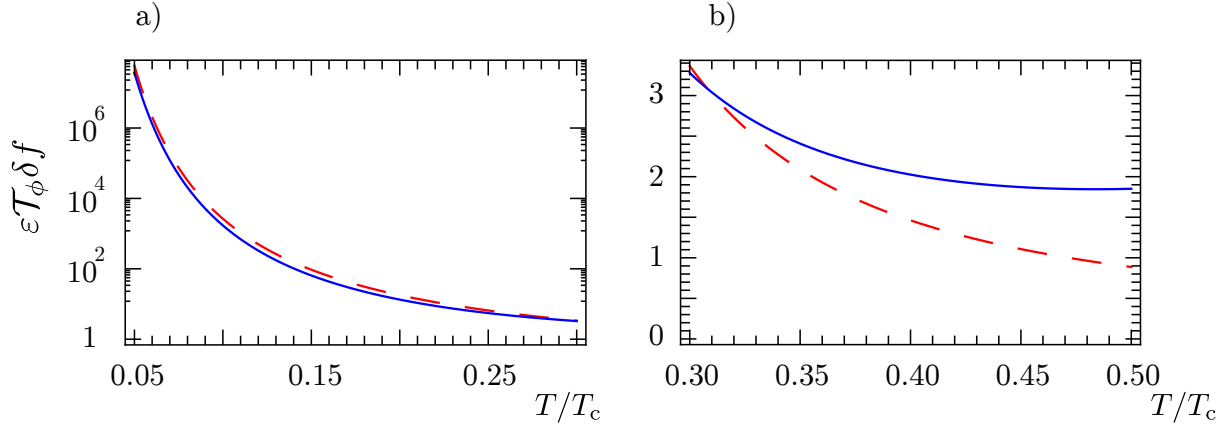


Figure 4.9: The figure shows the dephasing time multiplied by the level splitting of the fluxonium and by δf (blue) as a function of temperature in units of T_c . It is a measure of the possible number of operations performed within the dephasing time. The transmission of the junction is assumed to be $D = 10^{-2}$, $E_L/E_J = 5.8 \times 10^{-2}$ and $e^2 R/\Delta \approx 8 \times 10^{-13}$ s. The red dashed line shows a fit $d \times \exp(T_c/T)$ with $d = 1.2 \times 10^{-1}$.

If we write the density matrix of the qubit as $\rho(t) = \frac{1}{2}[\mathbb{1} + \boldsymbol{\tau} \cdot \mathbf{S}(t)]$ with $\mathbf{S}(t) = \text{Tr}[\rho(t)\boldsymbol{\tau}] = [\rho_{\text{LR}}(t) + \rho_{\text{RL}}(t), i\rho_{\text{LR}}(t) - i\rho_{\text{RL}}(t), \rho_{\text{LL}}(t) - \rho_{\text{RR}}(t)]^T$, we obtain from equation (4.32) the Pauli rate equation

$$\dot{\mathbf{S}}(t) = \mathbf{S}(t) \times \mathbf{h} - \gamma(S_1(t), S_2(t), 0)^T \quad (4.33)$$

with

$$\gamma = \frac{1}{2}(\gamma_{ee} - 2\gamma_{eg} + \gamma_{gg}) \quad (4.34)$$

This equation contains a precession around a pseudo-magnetic field, $\mathbf{h} = (w, 0, \varepsilon)^T$, determined by the qubit properties, and a relaxation of the coherences of the reduced density matrix with the rate γ , while the diagonal elements, namely the occupations of the qubit states, do not decay.

The value of the dephasing rate γ reads,

$$\gamma = \frac{\pi}{\hbar} \int_{\Delta}^{\infty} d\omega \left[V_e(N_1^e N_2^e)^{1/2} - V_g(N_1^g N_2^g)^{1/2} \right]^2 [f_1(-\omega)f_2(\omega) + f_1(\omega)f_2(-\omega)]. \quad (4.35)$$

Importantly, this rate equals zero if the wave functions of the states are even functions of the phase, so that we have $V_e = V_g$ and $N_l^e(\omega) = N_l^g(\omega)$. This is the case only when $f = 1/2$. We will now investigate in more detail the dephasing time \mathcal{T}_ϕ , which is the inverse of the dephasing rate, $\mathcal{T}_\phi = 1/\gamma$.

The dephasing time can be directly brought into contact with the heat current flowing through the qubit due to a finite temperature gradient and its sensitivity to the qubit state. In order to estimate this link, we consider the low temperature regime, $T, \delta T \ll T_c$, and write down the product between dephasing time and the difference in heat currents in the two qubit

states, $\delta\dot{Q}$,

$$\mathcal{T}_\phi \delta\dot{Q} = - \frac{\delta T \int_{\Delta}^{\infty} d\omega \omega^2 [V_e^2 N_1^e N_2^e - V_g^2 N_1^g N_2^g] / \cosh^2 \frac{\omega}{2k_B T}}{2k_B T^2 \int_{\Delta}^{\infty} d\omega [V_e \sqrt{N_1^e N_2^e} - V_g \sqrt{N_1^g N_2^g}]^2 / \cosh^2 \frac{\omega}{2k_B T}}. \quad (4.36)$$

This function gives us an idea about the energy which is transferred by the *difference* of heat currents in the two qubit states in the time, which the qubit needs to dephase. It is thus of importance to get a clearer understanding of the quantity given in equation (4.36). Since both integrand functions in equation (4.36) are negligible for $\omega > \Delta$, we obtain a rough estimate by calculating the integrals for $\Delta < \omega < \Delta + \delta$ with $\delta \ll 1$. We obtain

$$\mathcal{T}_\phi \delta\dot{Q} \approx \Delta \frac{T_c \delta T}{4T^2} \frac{|\cos \varphi_{\text{BS}}^e - \cos \varphi_{\text{BS}}^g|}{(|\sin \frac{\varphi_{\text{BS}}^e}{2}| - |\sin \frac{\varphi_{\text{BS}}^g}{2}|)^2}, \quad (4.37)$$

where we also used the approximation, $\frac{\Delta}{k_B T_c} \approx 1$, valid in BCS theory. From equation (4.37) it becomes clear that the dephasing time \mathcal{T}_ϕ is proportional to the gap Δ divided by the difference of heat currents in the two qubit states $\delta\dot{Q}$. This in turn is proportional to the heat current sensitivity to the qubit states, which was investigated in detail in the previous section. In order to understand the proportionality factor we make use of the results obtained in section 4.2.3. For small δf we can use equation (4.19) to rewrite the phases at the minima of the fluxonium potential such that the proportionality factor becomes

$$\frac{|\cos \varphi_{\text{BS}}^e - \cos \varphi_{\text{BS}}^g|}{(|\sin \frac{\varphi_{\text{BS}}^e}{2}| - |\sin \frac{\varphi_{\text{BS}}^g}{2}|)^2} \approx \frac{\sin \varphi^* (E_L - E_J \cos \varphi^*)}{E_L \pi \delta f}. \quad (4.38)$$

If in addition to $\delta f \ll 1$, we consider the inductive energy of the superinductance to be very small, $E_L/E_J \ll 1$, the factor can be expressed in terms of qubit energies and δf , only,

$$\frac{|\cos \varphi_{\text{BS}}^e - \cos \varphi_{\text{BS}}^g|}{(|\sin \frac{\varphi_{\text{BS}}^e}{2}| - |\sin \frac{\varphi_{\text{BS}}^g}{2}|)^2} \approx \frac{(E_L + E_J)}{E_J \delta f}. \quad (4.39)$$

With the results obtained in equations (4.39) and (4.37), we can estimate \mathcal{T}_ϕ for $\delta f \ll 1$ and $E_L/E_J \ll 1$ as

$$\mathcal{T}_\phi \approx \frac{\Delta T_c}{8\kappa_1(T) T^2 \left(\frac{E_L}{E_J}\right)^2 \left|\ln\left(\frac{E_L}{E_J}\right)\right|^2 \pi^2 \delta f^2} \approx \frac{e^2 R}{\Delta} \frac{e^{\frac{T_c}{T}}}{\left(\frac{E_L}{E_J}\right)^2 \left|\ln\left(\frac{E_L}{E_J}\right)\right|^2 \pi^2 \delta f^2}. \quad (4.40)$$

Exploiting equation (4.23), in the same limit for $\delta f \ll 1$ and $E_L/E_J \ll 1$ we can find a relation between the sensitivity of the fluxonium and the dephasing time

$$\mathcal{T}_\phi \approx \frac{\Delta T_c}{8\kappa_0(T) T^2 \delta f} s_{\text{fl}}^{-1}. \quad (4.41)$$

It is of major interest to find out if this dephasing time can limit the number of operations of the fluxonium qubit substantially.

The time scale on which the qubit is operated is typically given by the inverse of the level splitting of the qubit, $1/\varepsilon$ (where we set $\hbar = 1$). The latter is found from the difference of the energies of the ground and excited state from the Hamiltonian given in equation (2.28). It is this time scale which needs to be compared to \mathcal{T}_ϕ in order to find out about the typical number of operations which can be performed before the qubit dephases.

In figure 4.9, we show a plot of the function $\varepsilon\mathcal{T}_\phi \times \delta f$. Since with small changes in f , the level splitting increases linearly with δf , while \mathcal{T}_ϕ is proportional to $1/\delta f^2$, we choose to multiply the function of interest with δf in order to get a function which is independent of the magnetic flux at which the operation is performed. Figure 4.9 a) shows a logarithmic plot of $\varepsilon\mathcal{T}_\phi \times \delta f$ for small values of the temperature, $T \ll T_c$. The ratio between the two time-scales occurs to be approximately exponentially suppressed with increasing temperature. Figure 4.9 a) however shows that for small values of the temperature it is possible to perform a great number of operations on the qubit state before they become unreliable due to dephasing of the two level system. In particular, the required number of $\varepsilon\mathcal{T}_\phi$ for the fluxonium qubit to work properly is 10^4 , which for $\delta f = 10^{-2}$ is obtained as soon as the temperature is smaller than $0.15T_c$.

However, when the temperature gets larger, see figure 4.9, the dephasing can prevent the system from doing more than a small number of operations.

4.2.5 Conclusive remarks

In this section we have studied the thermal current flowing through an electrode of the fluxonium architecture in presence of small temperature gradients between the two arms. As expected, the circumstance that the heat current depends on the phase difference between the two electrodes, is at the origin of the sensitivity of the thermal current to the quantum state of the system. One of the most important results we have found is the independence of such a sensitivity on the number M of junctions realizing the superinductance, provided that the ratio E_C/E_J between the charging energy and the Josephson energy, as well as the ratio E_L/E_J between the inductive energy and the Josephson energy, are kept fixed. As stressed in the text, this M -independence can be, at least qualitatively, traced back to the fact that considering small values of thermal gradients determines that the thermal current in the electrode is practically due to the heat current in the black sheep that obviously does not depend on M . Another relevant aspect consists in the fact that when the loop is threaded with a magnetic flux that is close to half a superconducting flux quantum and in correspondence to small values of the ratio between the inductive energy and the Josephson energy, the sensitivity is proportional to $(E_L/E_J)^2 \ln(E_L/E_J)^2$ as clearly shown by equation (4.23), which gives an approximate analytical expression of the sensitivity s_{fl} .

Concerning the dephasing induced by the presence of thermal currents in the system we have found that, also in presence of small temperature gradients, there is a dephasing effect that could be not negligible. The dephasing time we have obtained depends both on the temperature and on the flux threading the loop. Moreover, the interesting property we have brought to light is its independence on the number M of junctions in the array realizing the superin-

ductance. It is important to underline that the results presented in this paragraph allow us to conclude that if the temperature is not sufficiently small ($T > 0.15 T_c$) the thermal current can constitute an important source of dephasing. As the nominal temperatures reached for today's superconducting devices are very small, it is unlikely that the thermal currents do constitute the dominant source of dephasing for those qubits. However, it is well known that quasiparticles in small superconducting structures badly thermalize, leading to problems in reaching the base temperature in the dilution refrigerator and thus effects of the phase dependence of the thermal current on the coherence properties of the fluxonium cannot be excluded.

Chapter 5

Conclusions

Superconducting flux qubits are particular superconducting devices based on Josephson junction properties. In this thesis various phenomena related to quantum coherences in superconducting flux qubits are investigated.

The first two chapters are in particular devoted to briefly summarize some properties of the Josephson junctions of interest in the context of this thesis and to discuss the different kinds of superconducting qubits recently realized and exploited in different applicative areas of physics. The original results are instead contained in the chapters 3 and 4.

In the third chapter, quantum coherences in superconducting flux qubit systems have been exploited in two cases. In the first case, starting from some experimental observations obtained by Chiarello et al. at the IFN-CNR laboratory in Rome, a theoretical analysis of the system's behavior has been done. In particular, the experiment investigated the effect of the modification speed of the potential shape in a double SQUID flux qubit, resulting in an interesting quantum effect due to the interplay of Landau-Zener transitions and resonant tunneling. Both of them give rise to the activation of quantum resonance phenomena manifesting themselves as peaks in the probability of measuring a right flux state of the SQUID at the end of the nonadiabatic transition. If the appearance of such peaks is traceable back to the Landau-Zener transitions and resonant tunneling, the way in which they manifest was not so clear. The theoretical analysis we have performed on this system furnish an explanation of the experimental data, relating the behavior of the probability of finding the system in the right flux state to the presence of quantum coherences in the initial condition of the system. In the second part of the chapter, we have proposed a new generation scheme for a GHZ state, namely a maximally entangled state, in a tripartite system of three superconducting qubits. This kind of study is important because entangled quantum states have indeed proved to be essential resources both for quantum information processing and computational tasks. We have also investigated the effects of the environment on the generation of GHZ states, concentrating our attention on all of the external degrees of freedom that can be effectively modeled as independent bosonic baths. Our analysis proves that the scheme for generating GHZ states is stable enough against the noise sources we consider.

In the last chapter of the thesis we concentrated our attention to a cause of dephasing in superconducting flux qubit which have not been investigated in detail before: dephasing due to thermal currents. Since these qubit systems are driven by microwave pulses this may lead to an unbalance of heating between the different sections of the superconducting loop. Moreover, quasiparticles in small superconducting structures badly thermalize, leading to problems in reaching the base temperature in the dilution refrigerator. These reasons can even lead to accidental temperature gradients between different electrodes of the system and consequently thermal currents can appear. Thermal currents through Josephson junctions was introduced in the first chapter of this thesis and in appendix A a detailed derivation of this current in the tunneling approximation was given. The interesting property of thermal current through superconducting Josephson qubits is that they are periodic function of the superconducting phase which characterizes the junction. In general, the flux qubit states are characterized by different values of the phase difference through their Josephson junctions. Since the thermal current through a device subject to a temperature gradient is also phase-dependent, we have shown that it is related to the phase-dependent qubit states. In particular we have studied the effect of a thermal gradient in a persistent current qubit and have calculated the sensitivity of the thermal current on the qubit states, showing that it is a linear function of the flux bias threading the loop of the qubit. Moreover, we have investigated the impact of a temperature gradient on the dynamics of the system. We have shown that the thermal currents have a measurement character on the state of the qubit. In other words, the thermal currents contribute to limiting the dephasing time of the qubit, according to the thermal gradient and the temperature of the system. The dephasing due to temperature gradients in a persistent current qubit can range from nano- to micro-seconds. A comparison with dephasing times imputable to other noise sources shows that their detrimental effects could be not negligible. In section 4.2 we have investigated the effects of temperature gradients in the most performant flux qubit: fluxonium. The reason for this is that this system is particularly well protected against flux noise thanks to its array of Josephson junctions which acts as a superinductance. We have studied the effects of very small thermal gradients and to do that we have used the thermal current in the linear response regime. What we have found is that the sensitivity of the thermal current to the qubit states is independent on the number of junctions in the array of the superinductance. The sensitivity only depends on the flux bias threading the loop and on the ratios E_C/E_J between the charging energy and the Josephson energy, as well as the ratio E_L/E_J between the inductive energy relative to the superinductance and the Josephson energy. We have found analytic expressions for the sensitivity as well as the dephasing time. Moreover, we have shown that when the loop is threaded with a magnetic flux that is close to half a superconducting flux quantum and in correspondence to small values of the ratio between the inductive energy and the Josephson energy, the sensitivity is proportional to $(E_L/E_J)^2 \ln(E_L/E_J)^2$ and the dephasing time is inversely proportional to the sensitivity. This means that the superinductance, which results in a small inductive energy, gives a good protection also to thermal dephasing. However, we have shown that if the temperature of the system is not sufficiently small ($T > 0.15T_c$), the thermal current can constitute an important source of dephasing in a fluxonium qubit.

The results discussed in this thesis are the content of reference [32, 77, 92] and of the paper “Dephasing of the fluxonium qubit due to heat currents” in preparation.

Appendix A

Derivation of the Maki-Griffin formula for the heat current

In this appendix, will be derived in detail the analytic formulae for the heat current, which it is used in (1.29) and (1.30) and which were previously found in [36]. Starting from equation (1.26) the first thing to do is to evaluate the full commutator $[H_{\text{tot}}, H_1]$. In this commutator only the contribution $[H_{\text{tot}}, H_1] = [H_T, H_1]$ is non-zero. Dealing with fermionic annihilation and creation operators, they must obey the anticommutation rule $\{c_{l,k\sigma}^\dagger, c_{mk'\sigma'}\} = \delta_{lm}\delta_{kk'}\delta_{\sigma\sigma'}$ from which it is possible to derive

$$[c_{l,k\sigma}^\dagger c_{l,k\sigma}, c_{l,k'\sigma'}^\dagger] = \delta_{kk'}\delta_{\sigma\sigma'}c_{l,k\sigma}^\dagger, \quad [c_{l,k\sigma}^\dagger c_{l,k\sigma}, c_{l,k'\sigma'}] = -\delta_{kk'}\delta_{\sigma\sigma'}c_{l,k\sigma}. \quad (\text{A.1})$$

Using these commutation relations, the evaluation of $[H_T, H_1]$ yields

$$\begin{aligned} [H_T, H_1] &= \sum_{k,q,\sigma} \sum_{k',\sigma'} \left\{ V_{kq}^{12} \xi_{1,k'} [c_{1,k\sigma}^\dagger, c_{1,k'\sigma'}^\dagger c_{1,k'\sigma'}] c_{2,q\sigma} + V_{kq}^{12*} \xi_{1,k'} c_{2,q\sigma}^\dagger [c_{1,k\sigma}, c_{1,k'\sigma'}^\dagger c_{1,k'\sigma'}] \right. \\ &\quad \left. - V_{kq}^{12} \Delta_{1,k'}^* [c_{1,k\sigma}^\dagger, c_{1,-k'\downarrow} c_{1,k'\uparrow}] c_{2,q\sigma} - V_{kq}^{12*} \Delta_{1,k'} c_{2,q\sigma}^\dagger [c_{1,k\sigma}, c_{1,k'\uparrow}^\dagger c_{1,-k'\downarrow}] \right\} \\ &= -2i \text{Im} \left\{ \sum_{k,q,\sigma} V_{kq}^{12} \xi_{1,k} c_{1,k\sigma}^\dagger c_{2,q\sigma} + V_{kq}^{12} (\Delta_{1,-k}^* c_{1,-k\uparrow} c_{2,q\downarrow} - \Delta_{1,k}^* c_{1,-k\downarrow} c_{2,q\uparrow}) \right\}. \end{aligned} \quad (\text{A.2})$$

Substituting this expression in (1.26), the expression in equation (1.27) is found

$$\frac{dQ^{(1)}}{dt} = \frac{2}{\hbar} \text{Im} \left\{ \sum_{k,q,\sigma} \left\langle V_{kq}^{12} \xi_{1,k} c_{1,k\sigma}^\dagger c_{2,q\sigma} + V_{kq}^{12} (\Delta_{1,-k}^* c_{1,-k\uparrow} c_{2,q\downarrow} - \Delta_{1,k}^* c_{1,-k\downarrow} c_{2,q\uparrow}) \right\rangle \right\}. \quad (\text{A.3})$$

The next step is to calculate the expectation values in the general expression for the heat current (A.3), yielding a Kubo formula, when expanding in the small tunnelling matrix elements. In general, to first order in perturbation theory, the expectation value of an operator $O(t)$ is

$$\langle O(t) \rangle = -i \int_{-\infty}^t dt' \langle [O(t), H_T(t')] \rangle_0 e^{\eta(t'-t)} \quad (\text{A.4})$$

where the brackets $\langle \cdot \rangle_0$ denote the equilibrium average with respect to the Hamiltonian $H_0 = H_1 + H_2$ without the perturbation H_T , and η is a small parameter which is eventually taken to zero. Using (A.4), the heat current can be written as

$$\begin{aligned} \frac{dQ^{(1)}}{dt} &= -\frac{2}{\hbar} \text{Re} \left\{ \int_{-\infty}^t dt' e^{\eta(t'-t)} \sum_{k,q,\sigma} \left\langle \left[\left(V_{kq}^{12} \xi_{1,k} c_{1,k\sigma}^\dagger(t) c_{2,q\sigma}(t) + \right. \right. \right. \\ &\quad \left. \left. \left. + V_{kq}^{12} (\Delta_{1,-k}^* c_{1,-k\uparrow}(t) c_{2,q\downarrow}(t) - \Delta_{1,k}^* c_{1,-k\downarrow}(t) c_{2,q\uparrow}(t)) \right), H_T(t') \right] \right\rangle_0 \right\}. \quad (\text{A.5}) \end{aligned}$$

As a first step, an evaluation of the commutator expression in the integrand is needed, which assumes the form

$$\begin{aligned} \sum_{k,q,\sigma} \sum_{k',q',\sigma'} &\left\{ V_{kq}^{12} V_{k'q'}^{12} \left[\xi_{1,k} \left(c_{1,k\sigma}^\dagger(t) c_{2,q\sigma}(t) c_{1,k'\sigma'}^\dagger(t') c_{2,q'\sigma'}(t') - c_{1,k'\sigma'}^\dagger(t') c_{2,q'\sigma'}(t') c_{1,k\sigma}^\dagger(t) c_{2,q\sigma}(t) \right) \right. \right. \\ &\quad - \Delta_{1,k}^* \left(c_{1,-k\downarrow}(t) c_{2,q\uparrow}(t) c_{1,k'\sigma'}^\dagger(t') c_{2,q'\sigma'}(t') - c_{1,k'\sigma'}^\dagger(t') c_{2,q'\sigma'}(t') c_{1,-k\downarrow}(t) c_{2,q\uparrow}(t) \right) \\ &\quad \left. + \Delta_{1,-k}^* \left(c_{1,-k\uparrow}(t) c_{2,q\downarrow}(t) c_{1,k'\sigma'}^\dagger(t') c_{2,q'\sigma'}(t') - c_{1,k'\sigma'}^\dagger(t') c_{2,q'\sigma'}(t') c_{1,-k\uparrow}(t) c_{2,q\downarrow}(t) \right) \right] \\ &+ V_{kq}^{12} V_{k'q'}^{12*} \left[\xi_{1,k} \left(c_{1,k\sigma}^\dagger(t) c_{2,q\sigma}(t) c_{2,q'\sigma'}^\dagger(t') c_{1,k'\sigma'}(t') - c_{2,q'\sigma'}^\dagger(t') c_{1,k'\sigma'}(t') c_{1,k\sigma}^\dagger(t) c_{2,q\sigma}(t) \right) \right. \\ &\quad - \Delta_{1,k}^* \left(c_{1,-k\downarrow}(t) c_{2,q\uparrow}(t) c_{2,q'\sigma'}^\dagger(t') c_{1,k'\sigma'}(t') - c_{2,q'\sigma'}^\dagger(t') c_{1,k'\sigma'}(t') c_{1,-k\downarrow}(t) c_{2,q\uparrow}(t) \right) \\ &\quad \left. + \Delta_{1,-k}^* \left(c_{1,-k\uparrow}(t) c_{2,q\downarrow}(t) c_{2,q'\sigma'}^\dagger(t') c_{1,k'\sigma'}(t') - c_{2,q'\sigma'}^\dagger(t') c_{1,k'\sigma'}(t') c_{1,-k\uparrow}(t) c_{2,q\downarrow}(t) \right) \right] \left. \right\}. \quad (\text{A.6}) \end{aligned}$$

In order to take the equilibrium expectation value of this expression, it is useful to employ the Green's functions defined in the following way

$$\begin{aligned} G_{l,k}^>(t, t') &= -i \langle c_{l,k}(t) c_{l,k}^\dagger(t') \rangle_0, & G_{l,k}^<(t, t') &= i \langle c_{l,k}^\dagger(t') c_{l,k}(t) \rangle_0, \\ F_{l,k}^>(t, t') &= -i \langle c_{l,k\uparrow}(t) c_{l,-k\downarrow}(t') \rangle_0, & F_{l,k}^<(t, t') &= i \langle c_{l,-k\downarrow}(t') c_{l,k\uparrow}(t) \rangle_0, \\ F_{l,k}^{\uparrow}>(t, t') &= i \langle c_{l,-k\downarrow}^\dagger(t') c_{l,k\uparrow}^\dagger(t) \rangle_0, & F_{l,k}^{\uparrow}<(t, t') &= -i \langle c_{l,k\uparrow}^\dagger(t) c_{l,-k\downarrow}^\dagger(t') \rangle_0. \end{aligned}$$

The linear-response formula for the heat current, equation (A.5) is then given by

$$\begin{aligned} \frac{dQ^{(1)}}{dt} &= \frac{2}{\hbar} \text{Re} \sum_{k,q} \int_{-\infty}^t dt' e^{\eta(t'-t)} \left\{ V_{kq}^{12} V_{-k-q}^{12} \left[\xi_{1,k} \left(F_{1,k}^{\uparrow}>(t, t') F_{2,q}^<(t, t') + F_{1,-k}^{\uparrow}<(t', t) F_{2,-q}^>(t', t) \right. \right. \right. \\ &\quad \left. \left. - F_{1,k}^{\uparrow}<(t, t') F_{2,q}^>(t, t') - F_{1,-k}^{\uparrow}>(t', t) F_{2,-q}^<(t', t) \right) + \Delta_{1,k}^* \left(G_{1,-k}^>(t, t') F_{2,q}^>(t, t') \right. \right. \\ &\quad \left. \left. - G_{1,-k}^<(t, t') F_{2,q}^<(t, t') \right) + \Delta_{1,-k}^* \left(G_{1,-k}^>(t, t') F_{2,-q}^<(t', t) - G_{1,-k}^<(t, t') F_{2,-q}^>(t', t) \right) \right] \\ &- |V_{kq}^{12}|^2 \left[2 \xi_{1,k} \left(G_{1,k}^<(t', t) G_{2,q}^>(t, t') - G_{1,k}^>(t', t) G_{2,q}^<(t, t') \right) + \Delta_{1,k}^* \left(F_{1,k}^<(t', t) G_{2,q}^>(t, t') \right. \right. \\ &\quad \left. \left. - F_{1,k}^>(t', t) G_{2,q}^<(t, t') \right) + \Delta_{1,-k}^* \left(F_{1,-k}^>(t, t') G_{2,q}^>(t, t') - F_{1,-k}^<(t, t') G_{2,q}^<(t, t') \right) \right] \left. \right\}. \quad (\text{A.7}) \end{aligned}$$

The next step is to express the Green's functions by their spectral densities

$$\begin{aligned}
G_{l,k}^>(t, t') &= -i \int_{-\infty}^{\infty} \frac{d\omega}{2\pi} e^{-i\omega(t-t')} (1 - f_l(\omega)) A_{l,k}(\omega), \\
G_{l,k}^<(t, t') &= i \int_{-\infty}^{\infty} \frac{d\omega}{2\pi} e^{-i\omega(t-t')} f_l(\omega) A_{l,k}(\omega), \\
F_{l,k}^>(t, t') &= i \int_{-\infty}^{\infty} \frac{d\omega}{2\pi} e^{-i\omega(t-t')} (1 - f_l(\omega)) B_{l,k}(\omega), \\
F_{l,k}^<(t, t') &= -i \int_{-\infty}^{\infty} \frac{d\omega}{2\pi} e^{-i\omega(t-t')} f_l(\omega) B_{l,k}(\omega).
\end{aligned} \tag{A.8}$$

where $f_l(\omega)$ is the Fermi function of the l -th electrode. Substituting these expressions, (A.8), into the equation for the heat current, (A.7), the latter simplifies significantly

$$\begin{aligned}
\frac{dQ^{(1)}}{dt} &= \frac{2}{\hbar} \text{Im} \sum_{k,q} \int_{-\infty}^{\infty} \frac{d\omega}{2\pi} \int_{-\infty}^{\infty} \frac{d\omega'}{2\pi} |V_{kq}^{12}|^2 (f_1(\omega) - f_2(\omega')) \\
&\times \left(-\Delta_{1,-k}^* \frac{A_{1,-k}(\omega) B_{2,-q}(\omega')}{\omega' - \omega - i\eta} + \Delta_{1,k}^* \frac{A_{1,k}(\omega) B_{2,q}(-\omega')}{\omega' - \omega + i\eta} + 2\Delta_{1,k}^* \frac{B_{1,k}(\omega) A_{2,q}(\omega')}{\omega' - \omega + i\eta} \right. \\
&+ \left. \xi_{1,k} \frac{B_{1,k}^*(\omega) B_{2,q}(\omega') - B_{1,k}(\omega) B_{2,q}^*(\omega')}{\omega' - \omega - i\eta} + 2\xi_{1,k} \frac{A_{1,k}(\omega) A_{2,q}(\omega')}{\omega' - \omega - i\eta} \right).
\end{aligned} \tag{A.9}$$

Here, since the tunneling matrix element is invariant under time reversal, the relation $V_{kq}^{12} V_{-k-q}^{12} = |V_{kq}^{12}|^2$ is used. According to microscopic BCS theory the spectral densities are $A_{l,k}(\omega) = 2\pi[|u_{l,k}|^2 \delta(\omega - E_{l,k}) + |v_{l,k}|^2 \delta(\omega + E_{l,k})]$ and $B_{l,k}(\omega) = 2\pi u_{l,k} v_{l,k} [\delta(\omega - E_{l,k}) - \delta(\omega + E_{l,k})]$, with $|u_{l,k}|^2 = 1/2(1 + \xi_{l,k}/E_{l,k})$, $|v_{l,k}|^2 = 1/2(1 - \xi_{l,k}/E_{l,k})$, and the quasi-particle energy-momentum relation $E_{l,k} = \sqrt{\xi_{l,k}^2 + |\Delta_{l,k}|^2}$. To continue the calculation, it is important to notice that the parameters $u_{l,k}$, $v_{l,k}$ and $\Delta_{l,k}$ are not independent, but that their phases are related by $\Delta_{l,k}^* v_{l,k}/u_{l,k} = E_{l,k} - \xi_{l,k}$, such that $\Delta_{l,k}^* v_{l,k}/u_{l,k}$ must be a real number. That is, the phase of $v_{l,k}$ relative to $u_{l,k}$ must be equal to the phase of $\Delta_{l,k}$. Without loss of generality it is possible to choose $u_{l,k}$ to be real and positive, so that $v_{l,k}$ and $\Delta_{l,k}$ must have the same phase [43]. Finally, the phase difference φ between the electrodes is introduced with the relation $\Delta_{1,k}^* v_{2,q} = |\Delta_{1,k}^* v_{2,q}| \exp(i\varphi)$.

The next stage of the calculation is to substitute the spectral densities, $A_{l,k}(\omega)$ and $B_{l,k}(\omega)$, into the heat current expression, (A.9), and to perform the sum over the momenta k and q . To do that, the sum over the momenta is transformed into an integral over the electronic energies $\xi_{l,k}$ with $l = 1, 2$, such that [124],

$$\begin{aligned}
\sum_k A_{l,k} &= \frac{\pi N_l^0}{2} \int_{-\infty}^{\infty} d\xi_{l,k} \left(\delta(\omega - E_{l,k}) + \delta(\omega + E_{l,k}) \right) \\
&= \pi N_l^0 \int_{|\Delta_{l,k}|}^{\infty} dE_{l,k} \frac{E_{l,k}}{\sqrt{E_{l,k}^2 - |\Delta_{l,k}|^2}} \left(\delta(\omega - E_{l,k}) + \delta(\omega + E_{l,k}) \right) \\
&= \frac{\pi N_l^0 |\omega|}{\sqrt{\omega^2 - |\Delta_l|^2}} \theta(\omega^2 - |\Delta_l|^2).
\end{aligned} \tag{A.10}$$

The normal-state density of states (including spin) of the l -th electrode is denoted by N_l^0 and finally is assumed an isotropic superconductor with an energy-independent gap. Similarly, for the other terms it is found

$$\begin{aligned}\sum_k B_{l,k} &= \text{sgn}(\omega) \frac{\pi N_l^0 |\Delta_l|}{\sqrt{\omega^2 - |\Delta_l|^2}} \theta(\omega^2 - |\Delta_l|^2), \\ \sum_k \xi_{l,k} A_{l,k} &= \text{sgn}(\omega) \frac{\pi N_l^0 (\omega^2 - |\Delta_l|^2)}{\sqrt{\omega^2 - |\Delta_l|^2}} \theta(\omega^2 - |\Delta_l|^2), \\ \sum_k \xi_{l,k} B_{l,k} &= 0.\end{aligned}\tag{A.11}$$

In (A.9) the term depending only on $B_{1,k} B_{2,q}$, which is related to the sole Cooper pairs contribution, vanishes, as it easy to notice using the last expression in (A.11). Using the relation $\lim_{\epsilon \rightarrow 0} \text{Im} \{1/(x - i\epsilon)\} = \pi \delta(x)$ and substituting the integrals over the spectral functions, (A.10) and (A.11), into the heat current, (A.9), it is possible to obtain

$$\begin{aligned}\frac{dQ^{(1)}}{dt} &= \frac{\pi}{\hbar} |V^{12}|^2 N_1^0 N_2^0 \int_{-\infty}^{\infty} d\omega \omega \frac{(f_1(\omega) - f_2(\omega)) \theta(\omega^2 - |\Delta_1|^2) \theta(\omega^2 - |\Delta_2|^2)}{\sqrt{\omega^2 - |\Delta_1|^2} \sqrt{\omega^2 - |\Delta_2|^2}} \\ &\times \left[\omega^2 - |\Delta_1| |\Delta_2| \cos \varphi \right].\end{aligned}\tag{A.12}$$

In the above derivation the normal densities of states and the tunnelling matrix elements are assumed energy-independent. Evaluating the theta-functions it is finally obtained

$$\begin{aligned}\frac{dQ^{(1)}(T_1, T_2)}{dt} &= \frac{dQ_{\text{qp}}^{(1)}(T_1, T_2)}{dt} - \frac{dQ_{\text{int}}^{(1)}(T_1, T_2)}{dt} \cos \varphi \\ &= \frac{2}{e^2 R_{12}} \int_{|\Delta_{\text{max}}|}^{\infty} d\omega \omega \frac{(f_1(\omega) - f_2(\omega))}{\sqrt{\omega^2 - |\Delta_1|^2} \sqrt{\omega^2 - |\Delta_2|^2}} \left[\omega^2 - |\Delta_1| |\Delta_2| \cos \varphi \right]\end{aligned}\tag{A.13}$$

where $|\Delta_{\text{max}}| = \max\{|\Delta_1(T_1)|, |\Delta_2(T_2)|\}$ and the normal-state conductance of the Josephson junction, defined via the inverse of the normal-state resistance, is $R_{12}^{-1} = \pi e^2 N_1^0 N_2^0 |V^{12}|^2 / \hbar$. In (A.13), the total heat current through the junction carried by quasiparticles is $dQ_{\text{qp}}^{(1)}(T_1, T_2)/dt$, while $dQ_{\text{int}}^{(1)}(T_1, T_2)/dt$ is the interference contribution to the heat current due to an interplay between quasiparticles and Cooper pair condensate. It is easy to see that $dQ_{\text{int}}^{(1)}(T_1, T_2)/dt$, which originates from the Josephson effect and is characteristic to weakly coupled superconductors, vanishes when at least one of the superconductors is in the normal state ($|\Delta_l(T_l)| = 0$).

Appendix B

Dynamics of an open quantum system

The aim of this appendix is to give the mathematical tools to study the dynamics of an open quantum system, when it is coupled to an environment modeled as a reservoir, whose degrees of freedom, by definition, are much more of that of the system under study.

Let us consider a quantum system S weakly coupled to a reservoir B. The total Hamiltonian will be

$$H = H_S + H_B + H_I \quad (\text{B.1})$$

where H_S and H_B are respectively the free Hamiltonian of the system and of the bath (reservoir) and H_I describes the interaction between the system and the reservoir. The operator which will give us the information on the state of the system will be the density operator $\rho(t)$, whose dynamics will be controlled by the Liouville-von Neumann equation ($\hbar = 1$)

$$\dot{\rho}(t) = -i[H, \rho(t)]. \quad (\text{B.2})$$

It is usually very difficult to solve equation (B.2) to study the evolution of the system. A possible solution to this problem is to write a master equation for the density operator of the system. This approach however requires to perform some approximations.

In order to obtain the master equation let us write the interaction Hamiltonian as [107]

$$H_I = \sum_{\alpha} A_{\alpha} \otimes B_{\alpha}. \quad (\text{B.3})$$

where A_{α} are operators which act only on the system, while B_{α} are operators of the bath. If the spectrum of H_S is discrete, and being ϵ the eigenvalues of H_S and $\Pi(\epsilon)$ the projection operator in the relative eigenspaces, we may define

$$A_{\alpha}(\omega) \equiv \sum_{\epsilon' - \epsilon = \omega} \Pi(\epsilon) A_{\alpha} \Pi(\epsilon'), \quad (\text{B.4})$$

which are called the eigenoperators of H_S . Let us also define the Fourier transform of the bath correlation function $\langle B_\alpha^\dagger(t)B_\beta(t-s) \rangle$

$$\Gamma_{\alpha\beta}(\omega) \equiv \int_0^{+\infty} ds e^{i\omega s} \langle B_\alpha^\dagger(t)B_\beta(t-s) \rangle = \frac{1}{2}\gamma_{\alpha\beta}(\omega) + iS_{\alpha\beta}(\omega) \quad (\text{B.5})$$

with $B_\alpha(t) = e^{iH_B t} B_\alpha e^{-iH_B t}$ being the bath operators in the interaction picture. The terms $\gamma_{\alpha\beta}(\omega)$ which will enter in the master equation as dissipative terms can also be written as

$$\gamma_{\alpha\beta}(\omega) = \Gamma_{\alpha\beta}(\omega) + \Gamma_{\beta\alpha}^*(\omega) = \int_{-\infty}^{+\infty} \langle B_\alpha^\dagger(s)B_\beta(0) \rangle. \quad (\text{B.6})$$

Following the derivation given in Ref. [107], we will perform the *Born-Markov* approximation, which require that the coupling between the system and the reservoir is sufficiently weak that the system does not influences the dynamics of the reservoir and even that the time-scale in which the system varies appreciably is much bigger that the time scale in which the correlation function of the bath decay. Moreover, we will also perform the *rotating wave approximation*, which can be applied when the system evolution time scales are much bigger than the relaxation time scales of the open system. Under these circumstances we may write a markovian master equation for the density operator of the system in the Schrödinger picture as [107]

$$\begin{aligned} \dot{\rho}_S(t) = & -i[H_S + H_{LS}, \rho_S(t)] + \\ & + \sum_{\omega} \sum_{\alpha, \beta} \gamma_{\alpha\beta}(\omega) \left(A_\beta(\omega) \rho_S(t) A_\alpha^\dagger(\omega) - \frac{1}{2} \{ A_\alpha^\dagger(\omega) A_\beta(\omega), \rho_S(t) \} \right) \end{aligned} \quad (\text{B.7})$$

where

$$H_{LS} = \sum_{\omega} \sum_{\alpha, \beta} S_{\alpha\beta}(\omega) A_\alpha^\dagger(\omega) A_\beta(\omega) \quad (\text{B.8})$$

it is usually called *Lamb shift* Hamiltonian, because simply renormalizes the energy levels of the free Hamiltonian, as a consequence of the coupling with the reservoir. It is possible to demonstrate that the Lamb shift Hamiltonian commutes with the free Hamiltonian of the system.

Appendix C

Appendix to the GHZ state generation scheme

C.1 Eigensolutions of the Hamiltonian given in (3.12)

The eigenstates of the Hamiltonian given in (3.12) can be written as common eigenstates $|s_{12}, s, m\rangle$ of the operators $S_{12}^2 = [\frac{1}{2}(\boldsymbol{\tau}^1 + \boldsymbol{\tau}^2)]^2$, S^2 and S_z and can be cast in the form

$$\begin{aligned} \left|1, \frac{3}{2}, -\frac{3}{2}\right\rangle &= |000\rangle \\ \left|1, \frac{3}{2}, \frac{3}{2}\right\rangle &= |111\rangle \\ \left|1, \frac{3}{2}, -\frac{1}{2}\right\rangle &= \frac{1}{\sqrt{3}}(|100\rangle + |010\rangle + |001\rangle) \equiv |W\rangle \\ \left|1, \frac{3}{2}, \frac{1}{2}\right\rangle &= \frac{1}{\sqrt{3}}(|011\rangle + |101\rangle + |110\rangle) \equiv |W'\rangle \\ \left|0, \frac{1}{2}, -\frac{1}{2}\right\rangle &= \frac{1}{\sqrt{2}}(|100\rangle - |010\rangle) \equiv |\psi_1\rangle \\ \left|0, \frac{1}{2}, \frac{1}{2}\right\rangle &= \frac{1}{\sqrt{2}}(|011\rangle - |101\rangle) \equiv |\psi'_1\rangle \\ \left|1, \frac{1}{2}, -\frac{1}{2}\right\rangle &= \frac{1}{\sqrt{6}}(|100\rangle + |010\rangle - 2|001\rangle) \equiv |\psi_2\rangle \\ \left|1, \frac{1}{2}, \frac{1}{2}\right\rangle &= \frac{1}{\sqrt{6}}(|011\rangle + |101\rangle - 2|110\rangle) \equiv |\psi'_2\rangle. \end{aligned} \tag{C.1}$$

The correspondent eigenvalues are given by

$$\begin{aligned}
E_{|000\rangle} &= -\frac{3}{2}(\omega - \tilde{g}) \\
E_{|111\rangle} &= \frac{3}{2}(\omega + \tilde{g}) \\
E_{|W\rangle} &= -\frac{1}{2}(\sqrt{3}\omega - 4g + \tilde{g}) \\
E_{|W'\rangle} &= \frac{1}{2}(\sqrt{3}\omega + 4g - \tilde{g}) \\
E_{|\psi_r\rangle} &= -(g + \frac{\tilde{g}}{2}) \quad \text{for } r = 1, 1', 2, 2'
\end{aligned} \tag{C.2}$$

C.2 Jump operators between the eigenstates of the Hamiltonian (3.12)

The Bohr frequencies of the system in the second step are given in (3.35) and the correspondent jump operators are respectively

$$\begin{aligned}
A_j(\omega_1) &= \frac{1}{\sqrt{3}}|000\rangle\langle W| \quad j = 1, 2, 3 \\
A_j(\omega_2) &= (-1)^{j+1} \frac{1}{\sqrt{2}}|000\rangle\langle\psi_1| + \frac{1}{\sqrt{6}}|000\rangle\langle\psi_2| \quad j = 1, 2 \\
A_3(\omega_2) &= -\sqrt{\frac{2}{3}}|000\rangle\langle\psi_2| \\
A_j(\omega_3) &= \frac{1}{\sqrt{3}}|W'\rangle\langle 111| \quad j = 1, 2, 3 \\
A_j(\omega_4) &= (-1)^{j+1} \frac{1}{\sqrt{2}}|\psi'_1\rangle\langle 111| + \frac{1}{\sqrt{6}}|\psi'_2\rangle\langle 111| \quad j = 1, 2 \\
A_3(\omega_4) &= -\sqrt{\frac{2}{3}}|\psi'_2\rangle\langle 111| \\
A_j(\omega_5) &= \frac{2}{3}|W\rangle\langle W'| \quad j = 1, 2, 3 \\
A_j(\omega_6) &= (-1)^j \frac{1}{\sqrt{6}}|W\rangle\langle\psi'_1| - \frac{1}{3\sqrt{2}}|W\rangle\langle\psi'_2| \quad j = 1, 2 \\
A_3(\omega_6) &= \frac{\sqrt{2}}{3}|W\rangle\langle\psi'_2| \\
A_j(\omega_7) &= -\frac{1}{\sqrt{6}}|\psi_1\rangle\langle W'| - \frac{1}{3\sqrt{2}}|\psi_2\rangle\langle W'| \quad j = 1, 2 \\
A_3(\omega_7) &= \frac{\sqrt{2}}{3}|\psi_2\rangle\langle W'| \\
A_j(\omega_8) &= (-1)^{j+1} \frac{1}{\sqrt{3}}(|\psi_1\rangle\langle\psi'_2| + |\psi'_1\rangle\langle\psi_2| + |\psi_2\rangle\langle\psi'_1| + \\
&\quad + |\psi'_2\rangle\langle\psi_1|) - \frac{2}{3}(|\psi_2\rangle\langle\psi'_2| + |\psi'_2\rangle\langle\psi_2|) \quad j = 1, 2 \\
A_3(\omega_8) &= -(|\psi_1\rangle\langle\psi'_1| + |\psi'_1\rangle\langle\psi_1|) + \frac{1}{3}(|\psi_2\rangle\langle\psi'_2| + \\
&\quad |\psi'_2\rangle\langle\psi_2|).
\end{aligned} \tag{C.3}$$

C.3 Jump operators of the Hamiltonian H_{rot}^{III}

As far as the third step it is useful to rewrite the jump operators of the first step in the basis $|\widetilde{000}\rangle, |\widetilde{111}\rangle, |\widetilde{W}\rangle, |\widetilde{W}'\rangle, |\widetilde{\psi}_1\rangle, |\widetilde{\psi}'_1\rangle, |\widetilde{\psi}_2\rangle$ and $|\widetilde{\psi}'_2\rangle$

$$\begin{aligned}
A_j(\omega_1) &= -\frac{1}{2\sqrt{3}} \left[(\cos\beta + i\sqrt{2}\sin\beta) (\sqrt{2}|\widetilde{W}\rangle\langle\widetilde{000}| + \right. \\
&\quad \left. + \sqrt{3}|\widetilde{\psi}_1\rangle\langle\widetilde{000}| + |\widetilde{\psi}_2\rangle\langle\widetilde{000}|) + (\cos\beta - i\sqrt{2}\sin\beta) \times \right. \\
&\quad \left. \times (\sqrt{2}|\widetilde{W}'\rangle\langle\widetilde{111}| + \sqrt{3}|\widetilde{\psi}'_1\rangle\langle\widetilde{111}| + |\widetilde{\psi}'_2\rangle\langle\widetilde{111}|) \right] \quad j = 1, 2 \\
A_3(\omega_1) &= -\frac{1}{\sqrt{6}} \left[(\cos\beta + i\sqrt{2}\sin\beta) (|\widetilde{W}\rangle\langle\widetilde{000}| + \right. \\
&\quad \left. - \sqrt{2}|\widetilde{\psi}_2\rangle\langle\widetilde{000}|) + (\cos\beta - i\sqrt{2}\sin\beta) (|\widetilde{W}'\rangle\langle\widetilde{111}| + \right. \\
&\quad \left. - \sqrt{2}|\widetilde{\psi}'_2\rangle\langle\widetilde{111}|) \right] \tag{C.4} \\
A_j(\omega_2) &= -\frac{\cos\beta}{3\sqrt{2}} \left[3|\widetilde{000}\rangle\langle\widetilde{000}| - 3|\widetilde{111}\rangle\langle\widetilde{111}| + |\widetilde{W}\rangle\langle\widetilde{W}| + \right. \\
&\quad \left. - |\widetilde{W}'\rangle\langle\widetilde{W}'| + 2|\widetilde{\psi}_2\rangle\langle\widetilde{\psi}_2| - 2|\widetilde{\psi}'_2\rangle\langle\widetilde{\psi}'_2| \right] \quad j = 1, 2 \\
A_3(\omega_2) &= -\frac{\cos\beta}{3\sqrt{2}} \left[3|\widetilde{000}\rangle\langle\widetilde{000}| - 3|\widetilde{111}\rangle\langle\widetilde{111}| + \right. \\
&\quad \left. + |\widetilde{W}\rangle\langle\widetilde{W}| - |\widetilde{W}'\rangle\langle\widetilde{W}'| + 3|\widetilde{\psi}_1\rangle\langle\widetilde{\psi}_1| + \right. \\
&\quad \left. - 3|\widetilde{\psi}'_1\rangle\langle\widetilde{\psi}'_1| + 2|\widetilde{\psi}_2\rangle\langle\widetilde{\psi}_2| - 2|\widetilde{\psi}'_2\rangle\langle\widetilde{\psi}'_2| \right].
\end{aligned}$$

Appendix D

Slopes of the sensitivities

In this appendix we provide the analytic formulas for the slopes of the sensitivities s_l for small $\delta f \ll 1$, found in paragraph 4.1. We find

$$\begin{aligned} m_1 &= \frac{2\pi \left[(4\alpha^2 - 1)^2 (2\alpha^2 - 1) + \alpha \frac{E_C}{E_J} (1 + 2\alpha^2) \right]}{(4\alpha^2 - 1)^{5/2} \left[1 - 2\alpha \frac{\dot{Q}_{\text{qp}}}{\dot{Q}_{\text{int}}} e^{-\frac{E_C}{E_J} \frac{\alpha}{(4\alpha^2 - 1)}} \right]} \\ m_2 &= \frac{2\pi\alpha \left[(4\alpha^2 - 1) + 4\alpha \frac{E_C}{E_J} \right]}{(4\alpha^2 - 1)^{3/2} \left[(2\alpha^2 - 1) - 2\alpha^2 \frac{\dot{Q}_{\text{qp}}}{\dot{Q}_{\text{int}}} e^{-\frac{E_C}{E_J} \frac{4\alpha}{(4\alpha^2 - 1)}} \right]} \\ m_3 &= \frac{2\pi\alpha \left[(4\alpha^2 - 1)^2 \left(2\alpha^2 - 1 + e^{-\frac{E_C}{E_J} \frac{3\alpha}{(4\alpha^2 - 1)}} \right) + \alpha \frac{E_C}{E_J} \left(2\alpha^2 + 1 + e^{-\frac{E_C}{E_J} \frac{4\alpha}{(4\alpha^2 - 1)}} (4\alpha^4 - 1) \right) \right]}{(4\alpha^2 - 1)^{5/2} \left[\left(e^{-\frac{E_C}{E_J} \frac{3\alpha}{(4\alpha^2 - 1)}} (2\alpha^2 - 1) + 1 \right) - 2\alpha(\alpha + 1) \frac{\dot{Q}_{\text{qp}}}{\dot{Q}_{\text{int}}} e^{-\frac{E_C}{E_J} \frac{\alpha}{(4\alpha^2 - 1)}} \right]}. \end{aligned}$$

The results are plotted in figure 4.3.

Bibliography

- [1] J. M. Martinis, S. Nam, J. Aumentado and C. Urbina, Phys. Rev. Lett. **89**, 117901 (2002)
- [2] A. Wallraff, D. I. Schuster et al, Nature **431**, 162 (2004)
- [3] A. B. Zorin and F. Chiarello, Phys. Rev. B **80**, 214535 (2009)
- [4] M. G. Castellano, F. Chiarello et al, Phys. Rev. Lett. **98**, 177002 (2007)
- [5] V. I. Shnyrkov, A. A. Soroka, and S. I. Melnyk, Low. Temp. Phys. **34**, 610 (2008)
- [6] A. Barone and G. Paternò, *Physics and Applications of the Josephson Effect*, John Wiley & Sons, Inc. (1981)
- [7] J. Q. You and F. Nori, Phys. Today **58**, 42 (2005)
- [8] A. Galianudinov and J. Martinis, Phys. Rev. A **78**, 010305(R) (2008)
- [9] R. Migliore, K. Yuasa, H. Nakazato and A. Messina, Phys. Rev. B **74**, 104503 (2006)
- [10] R. Migliore and A. Messina, Eur. Phys. J. B **34**, 269 (2003); A.V. Dodonov, et al., J. Phys. B **44**, 225502 (2011)
- [11] L. F. Wei, Y. X. Liu and F. Nori, Phys. Rev. Lett. **96**, 246803 (2006)
- [12] S. Matsuo, S. Ashhab, T. Fujii, F. Nori, K. Nagai and N. Hatakenaka, J. Phys. Soc. Japan **76**, 054802 (2007)
- [13] R. Migliore, K. Yuasa, M. Guccione, H. Nakazato and A. Messina, Phys. Rev. B **76**, 052501 (2007)
- [14] F. Altomare, J. I. Park, K. Cicak, M. A. Sillanpää, M. S. Allman, D. Li, A. Sirois, J. A. Strong, J. D. Whittaker and R. W. Simmonds, Nature Phys. **6** 777 (2010)
- [15] M. Neeley, R. C. Bialczak, M. Lenander, E. Lucero, M. Mariani, A. D. O'Connell, D. Sank, H. Wang, M. Weides, J. Wenner, Y. Yin, T. Yamamoto, A. N. Cleland and J. M. Martinis, Nature **467**, 570 (2010)
- [16] L. DiCarlo, M. D. Reed, L. Sun, B. R. Johnson, J. M. Chow, J. M. Gambetta, L. Frunzio, S. M. Girvin, M. H. Devoret and R. Schoelkopf, Nature **467**, 574 (2010)

-
- [17] R. Migliore, M. Scala, A. Napoli, K. Yuasa, H. Nakazato and A. Messina, *J. Phys. B: At. Mol. Opt. Phys.* **44**, 075503 (2011)
- [18] M. Wallquist, K. Hammerer, P. Zoller, C. Genes, M. Ludwig, F. Marquardt, P. Treutlein, J. Ye and H. J. Kimble, *Phys. Rev. A* **81**, 023816 (2010)
- [19] L. M. Duan and H. J. Kimble, *Phys. Rev. Lett.* **92**, 127902, (2004)
- [20] H. Kampermann, D. Bruß, X. Peng and D. Suter, *Phys. Rev. A* **81**, 040304(R) (2010)
- [21] J. Cho, S. Bose and M. S. Kim, *Phys. Rev. Lett.* **106**, 020504 (2011)
- [22] C. Ospelkaus, U. Warring, Y. Colombe, K. R. Brown, J. M. Amini, D. Leibfried and D. J. Wineland, [arXiv.org:quant-ph/1104.3573](https://arxiv.org/abs/1104.3573) (2011)
- [23] Yu. Makhlin, G. Schön and A. Shnirman, *Rev. Mod. Phys* **73**, 357 (2001)
- [24] J. M. Martinis, K. B. Cooper, R. McDermott, M. Steffen, M. Ansmann, K.D. Osborn, K. Cicak, Seongshik Oh, D. P. Pappas, R. W. Simmonds and C. C. Yu, *Phys. Rev. Lett.* **95**, 210503 (2005)
- [25] E. Paladino, A. D'Arrigo, A. Mastellone and G. Falci, *Physica E* **42**, 439 (2010)
- [26] A.J. Skinner and B.-L. Hu, *Phys. Rev. B* **78**, 014302 (2008)
- [27] D. A. Herrera-Martí, A. Nazir and S. D. Barret, *Phys. Rev. B* **88**, 094512 (2013)
- [28] J. Clarke and F. K. Wilhelm, *Nature* **453**, 1031 (2008)
- [29] Y. Nakamura, Yu. A. Pashkin and J. S. Tsai, *Nature* **398**, 786 (1999)
- [30] J. Bylander, S. Gustavsson, F. Yan, F. Yoshihara, K. Harrabi, G. Fitch, D. G. Cory, Y. Nakamura and J. S. Tsai and W. Oliver, *Nature Physics* **7**, 565-570 (2011)
- [31] G. Catelani, S. E. Nigg, S. M. Girvin, R. J. Schoelkopf, and L. I. Glazman, *Phys. Rev. B* **86**, 184514 (2012)
- [32] S. Spilla, F. Hassler, and J. Splettstoesser, *New J. Phys.* **16**, 045020 (2014)
- [33] S. Zanker and M. Marthaler, [arXiv:1410.8715](https://arxiv.org/abs/1410.8715) (2014)
- [34] J. E. Marchese, M. Cirillo, and N. Grønbech-Jensen, *Eur. Phys. J. Spec. Top.* **147**, 333 (2007)
- [35] N. Grønbech-Jensen and M. Cirillo, *Phys. Rev. Lett.* **95**, 067001 (2005)
- [36] K. Maki and A. Griffin, *Phys. Rev. Lett.* **15**, 921, (1965)
- [37] F. Giazotto and M. J. Martínez-Pérez, *Applied Physics Letters* **101**, 102601 (2012)
- [38] F. Giazotto and M. J. Martínez-Pérez, *Nature* **492**, 401 (2012)

-
- [39] M. J. Martínez-Perez and F. Giazotto, *Applied Physics Letters* **102**, 092602 (2013)
- [40] M. J. Martínez-Perez and F. Giazotto, *Applied Physics Letters* **102**, 182602 (2013)
- [41] F. Giazotto, M. J. Martínez-Perez and P. Solinas, *Phys. Rev. B* **88**, 094506 (2013)
- [42] R. P. Feynman, R. B. Leighton and M. Sands, *The Feynman Lectures on Physics* Vol. 3, Addison-Wesley (1965)
- [43] M. Tinkham *Introduction to Superconductivity* 2nd ed (New York: McGraw-Hill) (1996)
- [44] B. D. Josephson, *Phys. Lett.* **1**, 251, (1962)
- [45] P. W. Anderson and J. M. Rowell, *Phys. Rev. Lett.* **10**, 230 (1963)
- [46] W. C. Stewart, *Apple. Phys. Lett.* **12**, 277-280 (1968)
- [47] D. E. McCumber, *J. Appl. Phys.* **39**, 3113-3119 (1968)
- [48] A. Barone, *The Josephson effect: What it is-What it allows*, Proceedings of the International School of Physics “Enrico Fermi”: Models and Phenomenology for Conventional and High-temperature Superconductivity, IOS Press, Ohmsha (1998)
- [49] K. K. Likharev, *Dynamics of Josephson Junctions and Circuits*, Gordon and Breach, New York (1986)
- [50] L. Solymar, *Superconductive Tunneling and Applications*, Chapman and Hall LTD, London (1972)
- [51] M. Cyrot, D. Pavuna, *Introduction to Superconductivity and High-TC Materials*, World Scientific Publishing Co. Pte. Ltd (1992)
- [52] M. H. Devoret, A. Wallraff and J. M. Martinis, *ArXiv.org:cond-mat/0411174* (2004)
- [53] E. Zhao, T. Löfwander and J. A. Sauls, *Phys. Rev. B* **69**, 134503 (2004)
- [54] P. Joyez, P. Lafarge, A. Filipe, D. Esteve, M. H. Devoret, *Phys. Rev. Lett.* **72**, 2458-2461 (1994)
- [55] D. Flees, S. Han, J. Lukens, *Phys. Rev. Lett.* **78**, 4817-4820 (1997)
- [56] Y. Nakamura, C.D. Chen, J. S. Tsai, *Phys. Rev. Lett.* **79**, 2328-2331 (1997)
- [57] V. Bouchiat, D. Vion, P. Joyez, D. Esteve, M. H. Devoret, *Physica Scripta T* **76**, 165-170 (1998)
- [58] D. Vion, A. Aassime, A. Cottet, P. Joyez, H. Pothier, C. Urbina, D. Esteve, and M. H. Devoret, *Science* **296**, 886-889 (2002)
- [59] J. R. Friedman, V. Patel, W. Chen, S. K. Tolpygo, J. E. Lukens, *Nature* **406**, 43-46 (2000)

- [60] J. E. Mooij, T. P. Orlando, L. Levitov, L. Tian, C. H. van der Wal and S. Lloyd, *Science* **285** 1036 (1999)
- [61] T. P. Orlando, J. E. Mooij, L. Tian, C. H. van der Wal, L. S. Levitov, S. Lloyd, and J. J. Mazo, *Phys. Rev. B* **60**, 15398-15413 (1999)
- [62] J. Koch, T. M. Yu, J. Gambetta, A. A. Houck, D. I. Schuster, J. Majer, A. Blais, M. H. Devoret, S. M. Girvin, R. J. Schoelkopf, *Phys. Rev. A* **76**, 042319 (2007)
- [63] Manucharyan *et al.* *Science* **326**, 113 (2009)
- [64] C. Cohen-Tannoudji, B. Diu, F. Laloë, *Quantum Mechanics*, Wiley Interscience, Paris, (1977)
- [65] J. A. Schreier, A. A. Houck, J. Koch, D. I. Schuster, B. R. Johnson, J. M. Chow, J. M. Gambetta, J. Majer, L. Frunzio, M. H. Devoret, S. M. Girvin, and R. J. Schoelkopf, *Phys. Rev. B* **77**, 180502 (2008)
- [66] M. H. Devoret, J. M. Martinis, *Quantum Inf. Proc.* **3**, 163-203 (2004)
- [67] F. Chiarello, *The European Physical Journal B - Condensed Matter and Complex Systems* **55**, 7 (2007)
- [68] M. D. Reed, B. R. Johnson, A. A. Houck, L. DiCarlo, J. M. Chow, D. I. Schuster, L. Frunzio, and R. J. Schoelkopf, *Appl. Phys. Lett.* **96**, 203110-3, (2010)
- [69] A. P. Sears, A. Petrenko, G. Catelani, L. Sun, H. Paik, G. Kirchmair, L. Frunzio, L. I. Glazman, S. M. Girvin, and R. J. Schoelkopf, *Phys. Rev. B*, **86**, 180504 (2012)
- [70] A. B. Zorin, F.-J. Ahlers, J. Niemeyer, T. Weimann, H. Wolf, V. A. Krupenin, and S. V. Lotkhov, *Phys. Rev. B* **53**, 13682-13687, (1996)
- [71] F. C. Wellstood, C. Urbina, and J. Clarke, *Appl. Phys. Lett.* **50**, 772-774, (1987)
- [72] D. J. Van Harlingen, T. L. Robertson, B. L. T. Plourde, P. A. Reichardt, T. A. Crane, and J. Clarke, *Phys. Rev. B* **70**, 064517, (2004)
- [73] Hanhee Paik, D. I. Schuster, Lev S. Bishop, G. Kirchmair, G. Catelani, A. P. Sears, B. R. Johnson, M. J. Reagor, L. Frunzio, L. I. Glazman, S. M. Girvin, M. H. Devoret, and R. J. Schoelkopf, *Phys. Rev. Lett.* **107**, 240501 (2011)
- [74] D. A. Bennett, L. Longobardi, V. Patel, W. Chen, D. V. Averin, J. E. Lukens *Quantum Inf. Proc.* **8**, 217-243 (2009)
- [75] P. Bertet, I. Chiorescu, G. Burkard, K. Semba, C. J. P. M. Harmans, D. P. DiVincenzo and J. E. Mooij, *Phys. Rev. Lett.* **95**, 257002 (2005)
- [76] N. A. Masluk, Ph.D. thesis, YALE UNIVERSITY, 186 pages; 3572040 (2013)

- [77] F. Chiarello, S. Spilla, M. G. Castellano, C. Cosmelli, A. Messina, R. Migliore, A. Napoli, and G. Torrioli, *Phys. Rev. B* **89**, 134506 (2014)
- [78] L. D. Landau, *Physikalische Zeitschrift der Sowjetunion* **2**, pp. 46-51, (1932)
- [79] C. Zener, *Proc. R. Soc. Lond. A* **137**, (1932)
- [80] M. G. Castellano, F. Chiarello and G. Torrioli, *Journal of Superconductivity and Novel Magnetism* **24**, 1053 (2011)
- [81] M. G. Castellano, F. Chiarello et al, *New J. Phys.* **12**, 043047 (2010)
- [82] S. Poletto, F. Chiarello, M. G. Castellano, J. Lisenfeld, A. Lukashenko, C. Cosmelli, G. Torrioli, P. Carelli and A. V. Ustinov, *New J. of Phys.* **11**, 013009 (2009)
- [83] C. Cosmelli, P. Carelli, M. G. Castellano, F. Chiarello, R. Leoni and G. Torrioli, *IEEE Trans. App. Supercond.* **11**, 990 - 993 (2001)
- [84] F. Chiarello, E. Paladino, M. G. Castellano, C. Cosmelli, A. D'Arrigo, G. Torrioli and G. Falci, *New J. Phys.* **14**, 023031 (2012)
- [85] F. Yoshihara, K. Harrabi, A. O. Niskanen, Y. Nakamura and J. S. Tsai, *Phys. Rev. Lett.* **97**, 167001 (2006)
- [86] R. C. Bialczak, R. McDermott, M. Ansmann, M. Hofheinz, N. Katz, E. Lucero, M. Neeley, A. D. O'Connell, H. Wang, A. N. Cleland and J. M. Martinis, *Phys. Rev. Lett.* **99**, 187006 (2007)
- [87] O. Astafiev, Yu. A. Pashkin, Y. Nakamura, T. Yamamoto and J. S. Tsai, *Phys. Rev. Lett.* **96**, 137001 (2006)
- [88] L. S. Levitov, T. P. Orlando, J. B. Majer, J. E. Mooij [arXiv.org:cond-mat/0108266](https://arxiv.org/abs/cond-mat/0108266) (2001)
- [89] S. H. W. van der Ploeg, A. Izmailkov, A. Maassen van den Brink, U. Hübner, M. Grajcar, E. Il'ichev, H. -G. Meyer and A. M. Zagoskin, *Phys. Rev. Lett.* **98**, 057004 (2007)
- [90] C. Cosmelli, M. G. Castellano, F. Chiarello, R. Leoni, D. Simeone, G. Torrioli and P. Carelli, [arXiv.org:cond-mat/0403690](https://arxiv.org/abs/cond-mat/0403690) (2004)
- [91] W. Dür, G. Vidal, and J. I. Cirac, *Phys. Rev. A* **62**, 062314 (2000)
- [92] S. Spilla, R. Migliore, M. Scala, A. Napoli, *J. Phys. B: At. Mol. Opt. Phys.* **45**, 065501 (2012)
- [93] L. Chirulli and G. Burkard, *Phys. Rev. B* **74**, 174510 (2006)
- [94] M. R. Geller, E. J. Pritchett, A. Galiautdinov and J. M. Martinis, *Phys. Rev. A* **81**, 012320 (2010)
- [95] M. Scala, R. Migliore, A. Napoli and L. L. Sánchez-Soto, *Eur. Phys. J. D.* **61**, 199 (2011)

-
- [96] N. P. Oxtoby, Á. Rivas, S. F. Huelga and R. Fazio, *New J. Phys.* **11**, 063028 (2009)
- [97] A. Shnirman, G. Schön, I. Martin and Y. Makhlin, *Phys. Rev. Lett.* **94**, 127002 (2005)
- [98] E. Paladino, L. Faoro, G. Falci and R. Fazio, *Phys. Rev. Lett.* **88**, 228304 (2002)
- [99] Y. M. Galperin, B. L. Altshuler, J. Bergli and D. V. Shantsev, *Phys. Rev. Lett.* **96**, 097009 (2006)
- [100] L. Faoro, J. Bergli, B. L. Altshuler and Y. M. Galperin, *Phys. Rev. Lett.* **95**, 046805 (2005)
- [101] A. Grishin, I. V. Yurkevich and I. V. Lerner, *Phys. Rev. B* **72**, 060509 (2005)
- [102] J. Schrieffer, Y. Makhlin, A. Shnirman and G. Schön, *New J. Phys.* **8**, 1 (2006)
- [103] B. Abel and F. Marquardt, *Phys. Rev. B* **78**, 201302 (2008)
- [104] L. Faoro and L. B. Ioffe, *Phys. Rev. Lett.* **100**, 227005 (2008)
- [105] R. Migliore, M. Scala, A. Napoli, K. Yuasa, H. Nakazato and A. Messina, *J. Phys. B: At. Mol. Opt. Phys.* **44**, 075503 (2011)
- [106] M. Scala, R. Migliore and A. Messina, *J. Phys. A: Math. Theor.* **41**, 435304 (2008)
- [107] H. -P. Breuer and F. Petruccione, *The Theory of Open Quantum Systems*, Oxford University Press, Oxford (2002)
- [108] F. Giazotto, T. T. Heikkilä, A. Luukanen, A. M. Savin and J. P. Pekola, *Rev. Mod. Phys.* **78**, 217 (2006)
- [109] D. Golubev, T. Faivre and J. P. Pekola, *Phys. Rev. B* **87**, 094522 (2013)
- [110] M. J. Martínez-Pérez and F. Giazotto, *Applied Physics Letters* **102**, 182602 (2013)
- [111] E. Zhao, T. Löfwander and J. A. Sauls, *Phys. Rev. Lett.* **91**, 077003 (2003)
- [112] A. V. Timofeev, M. Helle, M. Meschke, M. Möttönen and J. P. Pekola, *Phys. Rev. Lett.* **102**, 200801 (2009)
- [113] H. Q. Nguyen, T. Aref, V. J. Kauppila, M. Meschke, C. B. Winkelmann, H. Courtois and J. P. Pekola, *New Journal of Physics* **15**, 085013 (2013)
- [114] J. M. Martinis, M. Ansmann and J. Aumentado, *Phys. Rev. Lett.* **103**, 097002 (2009)
- [115] G. Catelani, J. Koch, L. Frunzio, R. J. Schoelkopf, M. H. Devoret and L. I. Glazman, *Phys. Rev. Lett.* **106**, 077002 (2011)
- [116] J. Leppäkangas and M. Marthaler, *Phys. Rev. B* **85**, 144503 (2012)
- [117] F. Giazotto and J. P. Pekola, *J. Appl. Phys.* **97**, 023908 (2005)

-
- [118] S. Tirelli, A. M. Savin, C. P. Garcia, J. P. Pekola, F. Beltram and F. Giazotto, *Phys. Rev. Lett.* **101**, 077004 (2008)
- [119] I. Chiorescu, Y. Nakamura, C. J. P. M. Harmans and J. E. Mooij, *Science* **299**, 1869 (2003)
- [120] A. Kemp, S. Saito, W. J. Munro, K. Nemoto and K. Semba, *Phys. Rev. B* **84**, 104505 (2011)
- [121] R. Harris, J. Johansson, A. J. Berkley, M. W. Johnson, T. Lanting, S. Han, P. Bunyk, E. Ladizinsky, T. Oh, I. Perminov, E. Tolkacheva, S. Uchaikin, E. M. Chapple, C. Enderud, C. Rich, M. Thom, J. Wang, B. Wilson and G. Rose, *Phys. Rev. B* **81**, 134510 (2010)
- [122] D. Ristè, C. C. Bultink, M. J. Tiggelman, R. N. Schouten, K. W. Lehnert and L. DiCarlo, *Nature communications* **4**, 1913 (2013)
- [123] V. Ambegaokar and A. Baratoff, *Phys. Rev. Lett.* **10**, 486 (1963); **11**, 104(E) (1963)
- [124] H. Bruus and K. Flensberg, *Many-body quantum theory in condensed matter physics: An introduction*, Oxford University Press (2004)

Acknowledgments

I want to use this opportunity to thank all the people who supported me throughout the course of my Ph.D studies.

I deeply thank my supervisors Anna Napoli and Janine Splettstößer who have both been tremendous mentors for me. Their patient and wise advices encouraged my research and allowed me to grow as a research scientist. Moreover, I developed with both of them a deep human link which has been important to me during these years.

I thank Fabian Hassler, Rosanna Migliore and Antonino Messina for the scientific exchanges and stimulating conversations that contributed significantly to my thesis. I would like to thank Roberto Passante for the careful reading and correction of this thesis.

During my year in Aachen I had the luck to know wonderful colleagues, having lunches or going out for a beer with them. I heartily thank Guillem, Federica, Giovanni, Hernan, Francesca, Roman and Jens for having filled my mind with positive memories of this German year. Notwithstanding my usual “mantra” *vita amara* (life is bitter), they always managed to ease my mind and to make me smile. I am very grateful for this!

È doveroso per me ringraziare le splendide persone che ho avuto modo di avere al mio fianco (non per forza vicine) durante questi anni. Che dire della fantastica tribù che ho trovato nella stanza “dottorandi”? Posso solo dire di sentirmi una persona fortunata! Grazie a Salvo, Bruno, Saro, Matteo, Salvatore, Margherita, Federico e Pasquale (e a Daniele e Lucia, che sono componenti *ad honorem*) per avere reso il mio luogo di lavoro una seconda casa. Grazie ai ragazzi con i quali ho condiviso molti pranzi: Michele, Valeria, Federica, Francesco, Giorgio e Matteo. Grazie Luisa per essere stata una compagna di viaggio durante questo dottorato e grazie Riccardo, perché è raro trovare una guida e un amico nella stessa persona. Le discussioni, lo scambio di opinioni e le risate insieme a tutti voi sono stati motivo di una crescita umana oltre che scientifica, e non è poco.

Ringrazio di cuore la mia famiglia, per avermi sempre dato sostegno e motivazione per qualsiasi scelta abbia dovuto compiere. Grazie Dario, fratello acquisito, per aver condiviso questi anni con me e grazie Antuan per il tuo grande cuore. Lo sapete già che senza di voi e senza la musica del Senhor MuTrìo io posso ben poco. Ringrazio la mia seconda famiglia, la C.F.D., che più di tutti è riuscita nell’impresa di starmi sempre accanto in qualunque luogo mi trovassi.

Infine ringrazio Roberta, che sa la strada, io posso solo festeggiare.

Curriculum Vitae

Name: Samuele Spilla
Date of Birth: 27. May 1986
Place of Birth: Palermo (Italy)

University Studies

2008 – 2011 Master Degree in Theoretical Physics at the Università di Palermo
Degree: *110/110 cum laude*
Title of the Master Degree thesis: *Dissipative effects in the generation of non-classical states in Josephson circuits*
Supervisor: Dr. A. Napoli

2004 – 2008 Bachelor Degree in Physics at the Università di Palermo
Degree: *110/110 cum laude*
Title of the Master Degree thesis: *Quantum Zeno Effect*
Supervisor: Dr. A. Napoli

Funding/Grants

Since 2013 Member of the COST network MP1209
“Thermodynamics in the quantum regime”

2012 - 2014 Scholarship for the Ph.D. research by the Università di Palermo

Languages

Italian (native), English (fluent), German (basic), Portuguese (basic).

Publications

- (1) S. Spilla, A. Napoli, F. Hassler and J. Splettstoesser, *Thermal current in a Fluxonium qubit*, In preparation
- (2) S. Spilla, F. Hassler and J. Splettstoesser, *Measurement and dephasing of a flux qubit due to heat currents*, New J. Phys. **16**, 045020 (2014).
- (3) F. Chiarello, S. Spilla, M. G. Castellano, C. Cosmelli, A. Messina, R. Migliore, A. Napoli, and G. Torrioli, *Resonant effects in a SQUID qubit subjected to nonadiabatic changes*, Phys. Rev. B **89**, 134506 (2014).
- (4) S. Spilla, R. Migliore, M. Scala and A. Napoli, *GHZ state generation of three Josephson qubits in the presence of bosonic baths*, J. Phys. B: At. Mol. Opt. Phys. **45**, 065501 (2012).